Zn_3P_2 and Cu_2O Substrates for Solar Energy Conversion

Thesis by
Gregory Michael Kimball

In Partial Fulfillment of the Requirements
for the Degree of
Doctor of Philosophy

California Institute of Technology
Pasadena, California

2012

(Defended September 27, 2011)

To Chris Kimball

for his fascination with the greatest machines built by man

Acknowledgements

Looking back at my time at Caltech, I can see why in *The Art of Scientific Investigation* W. I. B. Beveridge wrote: "Research has been likened to warfare against the unknown." During my campaign against zinc phosphide, Harry Atwater and Nathan Lewis have provided indispensable mentorship, guidance, and support. Harry always finds a way to break down the barriers to research and recruit enthusiastic new scientists, and Nate has always challenged me to scrutinize my assumptions and design experiments with focus. Their labs at Caltech have provided seemingly endless equipment and materials as well as unmatched colleagues and peers.

I thank my thesis committee for their encouragement, patience, and feedback. Harry Gray has been a constant source of enthusiasm from my first weeks at Caltech, and since then he has presided as the chair of my thesis committee. Mitchio Okumura motivated me to propose new experiments in atmospheric chemistry, and Rick Flagan made sure I knew what I was talking about. Tom Miller's curiosity and breadth of interest will always inspire me.

My time at Caltech was facilitated by the NDSEG fellowship, the National Defense Science and Engineering Graduate fellowship from the Department of Defense. It would have been difficult to start this project without the fellowship's generous support. The Department of Energy, through the Basic Energy Sciences and Solar Energy Technologies programs, played an essential role enabling research in earth-abundant semiconductors at Caltech.

Since the fall 2009, the partnership between Caltech and the Dow Chemical Company has transformed our research in earth-abundant semiconductors. Marty DeGroot, Rebekah Feist, Jim Stevens, Michael Mills, David Kagan, and Steve Rozeveld are all part of the same team with the researchers at Caltech: working through challenges week by week and doing the hard work of basic research. I am grateful for the generous support of Dave Parillo, Kirk Thompson, Narayan Ramesh, Susan Zerull, and Stephanie Potts–working with you has not only been tremendously productive, but also open and enjoyable!

The people I have worked with directly at Caltech have taught me everything I know about designing experiments and solving research problems: Chengxiang Xiang, Ron Grimm, Jeff Bosco, Faisal Tajdar, Astrid Müller, Adele Tamboli, Dan Turner-Evans, Marina Leite, Emily Warmann, Emily Kosten, and Michael Kelzenberg. My colleagues who have worked with me to prepare material for grant proposals, updates, and reviews have been indispensable: James McKone, Vivian Ferry, Krista Langeland, Davis Darvish, Imogen Pryce, Samantha Wilson, Naomi Coronel, Yulia Tolstova, Lise Lahourcade, Prineha Narang, and Nick Strandwitz. The brave undergraduate researchers who worked with me contributed both to this thesis and to my growth as a mentor: Jeanne (Yiwen) Peng, Jared Sacco, Charlie Jaramillo, and Andrew Gong.

The students and postdocs who generously gave me teaching and training defined my experience at Caltech. Michael Filler, Jennifer Dionne, Melissa Archer, Matthew Dicken, Andrew Leenheer, Seokmin Jeon, and Michael Deceglie labored with me to build and maintain (U)HV equipment; Steven Maldonado, Emily Warren, and Liz Santori helped me navigate photoelectrochemistry; Domenico Pacifici, Gerald Miller, Ryan Briggs, Eyal Feigenbaum, Robert Walters, Deirdre O'Carroll, and Jim Fakonas taught me to use optics equipment; David Gleason-Rohrer, David Knapp, Leslie O'Leary, Matthew Traub, Judith Lattimer, Lars Erik Johansson, and Keisuke Nakayama mused with me about surface science. Then there are the LG/A-Team joint students: Brendan Kayes, Shannon Boettcher, and Amanda Shing, who share with me the same convoluted perspective.

Every person in the two research groups has taught me something, built something with me and/or enriched my experience: Matthew Bierman, Michael Walter, Kate Plass, Josh Spurgeon, Anna Folinsky, Craig Wiggenhorn, Heather McCaig, Tony Fitch, Edgardo García-Berríos, Don Walker, Marc Woodka, Jordan Katz, Kimberly Papadantonakis, Kenneth Diest, Stanley Burgos, Dennis Callahan, Luke Sweatlock, Morgan Putnam, Carrie Hofmann, Katsu Tanabe, Joseph Beardslee, Heather Audesirk, Karla Reyes, Shane Ardo, Rob Coridan, Qixi Mi, Mike Rose, Bryce Sadtler, Koray Aydin, Jonathan Grandidier, Carissa Eisler, Jeremy Munday, Cristofer Flowers, Chris Chen, and Hal Emmer. I shared the sacred fraternity of

pwnage with Jacob Good, Adam Pieterick, Zagid Abatchev, Andrew Meng, Sang Hee Park, Adam Nichols-Nielander, and Qiushi (Ben) Yin.

The equipment and instrumentation support I received at Caltech made this thesis possible. Bruce Brunschwig of the Molecular Materials Research Center provided surface science training and equipment; Ali Ghaffari's Micro/Nano lab played a central role for device fabrication; Yunbin Guan, Chi Ma, and George Rossman helped me hijack the facilities of the geology department for semiconductors; Scott Walck and Carol Garland guided me through wafer lapping and polishing; Jay Winkler built and maintained the picosecond laser system; Rick Gerhart fabricated the crystal growth quartzware; Melinda Bakarbessy, Stephanie Fry and Christina Aguilar labored with me to transfer technology; Dana Roth dug up obscure and fascinating data; Mike Roy and Steve Olsen provided numerous custom machined pieces.

I cannot repay the tireless work from the group administrators: Sherry Feick, April Neidholdt, Amy Crown, Lyra Haas, Elyse Garlock, Tiffany Kimoto, Jennifer Blankenship and Barbara Miralles. The assistance from Agnes Tong from my division, Steven Gould in purchasing, Tess Legaspi in the Registrar's office and Natalie Gilmore and Icy Ma in the graduate office has also been indispensable. Without your help I could not have joined the group, been a candidate, defended my propositions, or defended my thesis.

The people who deserve special credit, though, are the friends and family who have been with me through triumphs and defeats of all sizes during my time at Caltech. To my roommates (and honorary roommates) Douglas Tham, Jingqing Huang, Andrej Svorencik, Marjan Praljak, Molei Tao, George Cadena, Paul Nelson, James Raftery, Jeff LeHew, and Darren Michaels: thank you for trusting me as "Head of Security." Together we left noise complaints unheeded and travelled the West in search of excitement. To Paco and Olive: it has been a pleasure to share so many holidays, parties, and rites of passage–I do not know where Pia and I could find better teammates. To my rockstars Dan Brox, Andrea Robbett, Mohamed Mostagir, Hadil Ghoneim, and the precocious Laila: thank you for creating raucous rhythms with me in the basements of Caltech. To my chemists Edward Weintrob, Ian Tonks,

Matt Winston, and Young In Oh: thank you for always being up for adventure and explaining to me how chemistry works.

I could not have made it here without the tenacity, curiosity, and honesty instilled in me by my family. To my grandmother, my mother, my sister Whitney, and my brother Chris: your encouragement from the beginning made this possible. To Pia: thank you for taking this journey with me–humoring me when I am exuberant, placating me when I am crushed and making me grateful for each day.

Gregory M. Kimball

September 2011

Pasadena, CA

Abstract

Zinc phosphide (Zn_3P_2) and cuprous oxide (Cu_2O) are promising and earth-abundant alternatives to traditional thin film photovoltaics materials such as CIGS, CdTe and a-Si. We have prepared high purity substrates of Zn_3P_2 from elemental zinc and phosphorus, and Cu_2O by the thermal oxidation of copper foils, to investigate their fundamental material properties and potential for solar energy conversion. Photoluminescence-based measurements of Zn_3P_2 substrates have revealed a fundamental indirect band gap at 1.38 eV and a direct band gap at 1.50 eV, with time-resolved data indicating minority carrier diffusion lengths of $\geq$7 μm. Solar cells based on Mg/Zn_3P_2 junctions with solar energy conversion efficiency reaching 4.5% were examined by composition profiling to elucidate the passivation reaction between Mg metal and Zn_3P_2 surfaces. Semiconductor/liquid junctions incorporating Cu_2O substrates exhibited open-circuit voltage, V_{oc}, values in excess of 800 mV and internal quantum yields approaching 100% in the 400–500 nm spectral range.

Contents

List of Figures

List of Tables

List of Publications

Portions of this thesis have been drawn from the following publications:

Gregory M. Kimball, Nathan S. Lewis, and Harry A. Atwater, Direct Evidence of Mg–Zn–P formation in Mg/Zn_3P_2 solar cells, *Conference Record of the Thirty-seventh IEEE Photovoltaic Specialists Conference*, 2011.

Chengxiang Xiang, Gregory M. Kimball, Ronald L. Grimm, Harry A. Atwater, and Nathan S. Lewis, 820 mV Open-Circuit Voltages from Cu_2O/CH_3CN Junctions, *Energy, Environ. Sci.*, 2011, 4(4), 1311–1318.

Gregory M. Kimball, Nathan S. Lewis, and Harry A. Atwater, Mg Doping and Alloying in Zn_3P_2 Heterojunction Solar Cells, *Conference Record of the Thirty-fifth IEEE Photovoltaic Specialists Conference*, 2010.

Gregory M. Kimball, Astrid M. Müller, Nathan S. Lewis, Harry A. Atwater, Photoluminescence-based measurements of the energy gap and diffusion length of Zn_3P_2, *Applied Physics Letters* 95, 112103, 2009.

Chapter 1

Introduction

This thesis details the material properties of high purity zinc phosphide (Zn_3P_2) semiconducting substrates and the device performance of Zn_3P_2 solar cells. Chapter 2 outlines the methods for producing high quality Zn_3P_2 substrates from elemental zinc and phosphorus. Chaper 3 compiles the bulk optoelectronic properties of the Zn_3P_2 substrates that are relevant for photovoltaic applications. Chapter 4 investigates the relationship between surface composition and surface defect density for Zn_3P_2 as a function of chemical treatment. Finally, chapter 5 applies the insights from surface science experiments to elucidate the Mg passivation reaction underlying the record performance of 6% efficient Mg/Zn_3P_2 solar cells.

1.1 α-Zn_3P_2 as a Photovoltaic Material

α-Zn_3P_2 has been shown to exhibit many promising qualities for a photovoltaic absorber material, with a direct band gap of 1.5 eV [1] and 6% efficient solar energy conversion achieved in Mg/Zn_3P_2 devices [2]. Zn_3P_2 is part of a class of Group II–V materials including Zn_3N_2, Cd_3As_2, Zn_3As_2, and Cd_3P_2. Although the P sublattice in α-Zn_3P_2 is essentially a zincblende arrangement of atoms, the Zn atoms display a less symmetric structure [3, 4]. As a result the tetragonal α-Zn_3P_2 has a 40 atom unit cell (figure 1.1) in contrast to the 8 atom unit cell of zincblende Group III–V semiconductors such as InP. In the crystal structure of α-Zn_3P_2, the Zn–P bond distances display a significant variation with Zn atoms bonded in distorted tetrahedra and P atoms bonded in distorted octahedra [1].

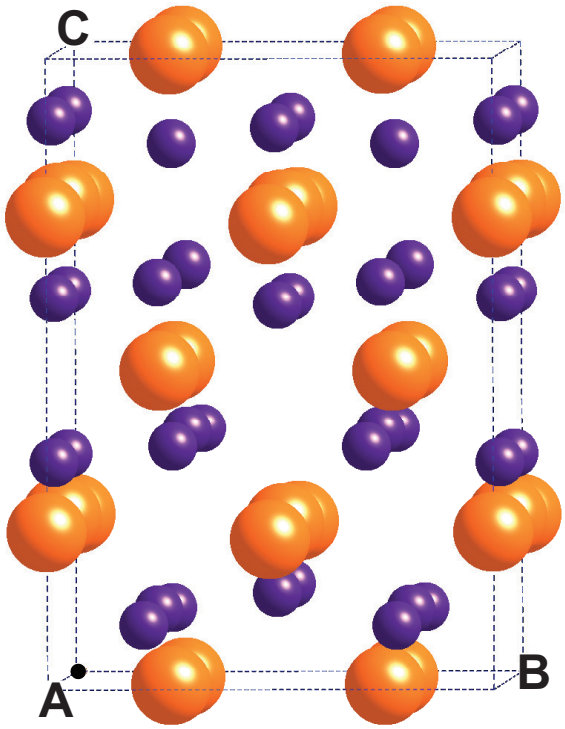

Figure 1.1. Representation of the tetragonal crystal structure of α-Zn_3P_2, where orange spheres correspond to phosphorus atoms and purple spheres correspond to zinc atoms. The crystal structure has nearly zincblende phosphorus sublattice [4].

1.2 Synthetic Methods for α-Zn_3P_2

The advantages of α-Zn_3P_2 as a photovoltaic material include its binary composition, earth-abundant component elements and simple phase diagram for the α-Zn_3P_2 phase (figure 1.2). α-Zn_3P_2 sublimes congruently via P_4 and Zn to produce films of α-Zn_3P_2, highlighting a straightforward process for thin film absorber fabrication [5] and high quality polycrystals. Chapter 2 describes the methods for synthesizing high purity α-Zn_3P_2 substrates.

The Zn–P phase diagram contains four zinc-phosphorus compound materials: α-Zn_3P_2, β-Zn_3P_2, α-ZnP_2, and β-ZnP_2 [6]. Each material has been reported to be semiconducting and exhibits band gap values in the range of interest for photovoltaic applications (1.3 to 2.0 eV) [7, 8]. Although all of the Zn–P semiconductors appear to be promising candidate materials for solar energy conversion, this thesis focuses on the optoelectronic properties and device applications of α-Zn_3P_2. In the following chapters, the low temperature phase α-Zn_3P_2 will simply be referred to as Zn_3P_2.

1.3 Optoelectronic Properties of Zn_3P_2

The bulk optoelectronic properties of the Zn_3P_2 substrates described in chapter 3 confirm the nearly ideal properties of Zn_3P_2 for photovoltaic applications. Zn_3P_2 has a direct band gap at 1.5 eV [1] that is optimally suited for solar energy conversion [9] as well as a fundamental indirect band gap at 1.38 eV [10]. Zn_3P_2 substrates exhibited good minority carrier properties that allowed for the high internal quantum yields needed for efficient solar energy conversion. Minority carrier lifetimes of $\approx$20 ns, corresponding to minority carrier diffusion lengths $\geq$7 μm, were measured for high purity Zn_3P_2 substrates. The majority carrier density, or bulk doping, of Zn_3P_2 was controlled across a wide range of p-type doping concentrations from 10^{13} to 10^{18} holes $\cdot$ cm^{-3} with hole mobility values of 15–20 cm$^2 \cdot$ V$^{-1} \cdot$ s^{-1}. The doping procedures included annealing in P_4 vapor to introduce interstitial phosphorus and

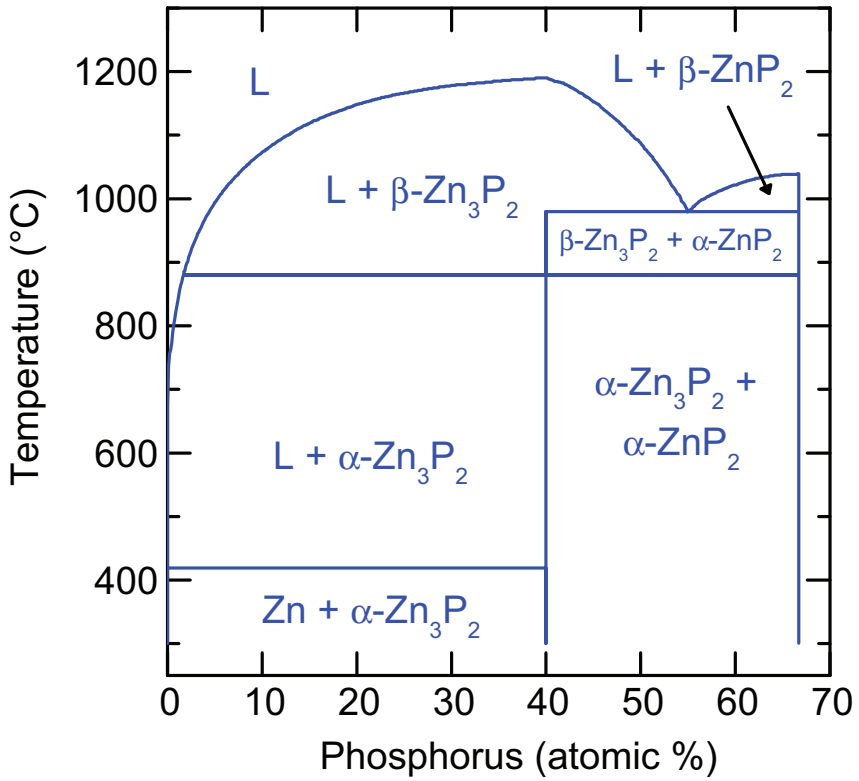

Figure 1.2. Phase diagram for Zn–P compounds as a function of temperature and phosphorus composition showing α-Zn_3P_2 as the stable phase under a range of conditions [6].

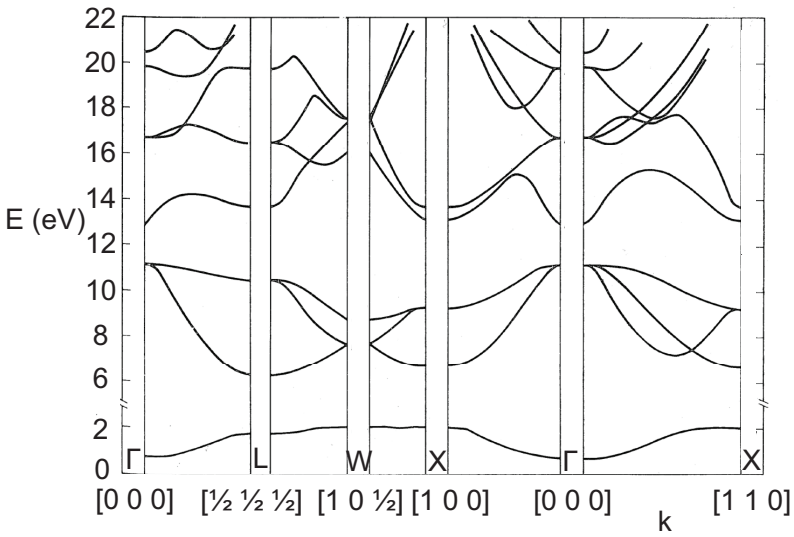

Figure 1.3. Band structure calculations for Zn_3P_2 using a fluorite approximation and averaged vacancy psuedopotential to find a fundamental direct band gap along the Γ direction [11].

solid-source diffusion to introduce Ag impurities.

The computational evaluation of the band structure of Zn_3P_2 is heavily reliant on the approximations used to represent the 40-atom unit cell. The band structure calculations by Lin-Chung, using a fluorite approximation and averaged vacancy psuedopotential, found a fundamental direct gap for Zn_3P_2 (figure 1.3) [11]. Later calculations by Andrzejewski et al. used the nonlocal empirical psuedopotential method and found a fundamental direct gap for the full crystal structure (D_{4h}^{17}) but a fundamental indirect band gap for an idealized tetragonal approximation (D_{4h}^{15}) [12]. The experimental approach by photoluminescence analysis described in chapter 3 settles the controversy over the nature of fundamental band gap of Zn_3P_2.

1.4 Interfaces and Heterojunctions

Chapter 4 describes chemical methods for controlling the defect density of Zn_3P_2 surfaces. Because of the difficulty of doping Zn_3P_2 n-type, heterojunctions [13, 14, 15] and semiconductor/liquid junctions [16, 17] have been investigated for solar energy applications. Unfortunately, these devices have displayed open-circuit voltages

<300 mV, significantly less that the open-circuit voltage of 900–970 mV that is expected for an ideal device incorporating Zn_3P_2. One explanation for the poor performance is that electronically defective Zn_3P_2 interfaces are formed by the chemical treatments used to prepare substrates for device fabrication.

Chemical etching of Zn_3P_2 substrates in 2% Br_2 in methanol was effective for removing surface oxidation and polishing damage, but the resulting surface still contained a high density of defects. Zn_3P_2 substrates etched with Br_2 in methanol exhibited ≈4 ML of residual elemental phosphorus and removing the elemental phosphorus in 10% HF–0.25% H_2O_2 (aq) correlated with improved interface quality. Significantly lower defect densities were measured for Zn_3P_2 substrates that had been exposed to air compared to those measured for freshly etched Zn_3P_2 substrates. Controlled oxidation of Zn_3P_2 also appears to be a promising route to passive interfaces with low defect density.

Inspection of the Zn_3P_2 unit cell suggests several additional approaches to molecular control of the surface. The tetragonal unit cell of Zn_3P_2 contains a cubic phosphorus sublattice, making the anion sublattice remarkably similar to that of zincblende GaAs and InP (figure 1.4). Zinc atoms in Zn_3P_2 have a nearly tetrahedral bonding configuration, with mixed covalent and ionic bonding with the four neighboring phosphorus atoms. Examination of the Zn_3P_2(101)A plane shows terminal zinc atoms with interatomic distances of 3.81 Å, similar to the 3.89 Å spacing of gallium atoms in the GaAs(111)A plane. In contrast, the Zn_3P_2(110)A plane has a tighter structure, with zinc interatomic distances of 3.11 Å. Sulfide passivation treatments that have shown efficacy with GaAs may also improve Zn_3P_2 surface quality [18]. For modifying the InP(111)B surface, functionalizing terminal P–OH sites with organic halides is a versatile synthetic route and may be an approach that is compatible with the Zn_3P_2 surface [19]. The Zn_3P_2(101)B and the InP(111)B surface have similar phosphorus spacings of 4.15 and 4.04 Å, respectively, and could be expected to participate in similar P–OH chemistry.

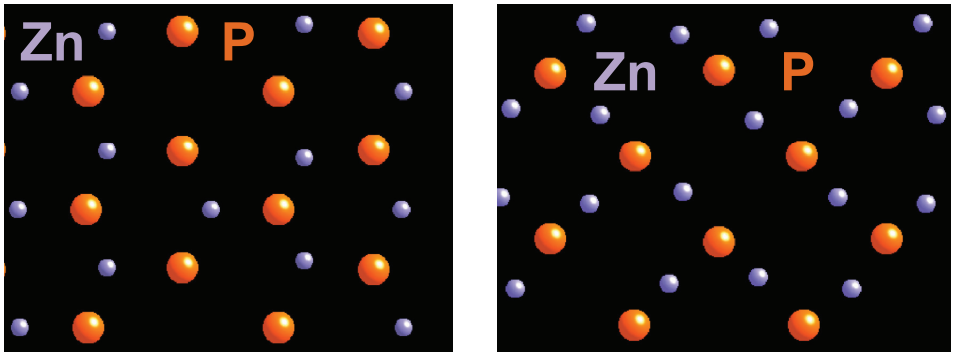

Figure 1.4. Representation of the tetragonal crystal structure of α-Zn_3P_2, (left) showing the (101) crystallographic plane and (right) showing the (110) crystallographic plane. Note the similarity of the phosphorus sublattice to the zincblende (111) plane on the left and the (100) plane on the right.

1.5 Mg/Zn_3P_2 Solar Cells

The record solar energy conversion efficiency for a device with a Zn_3P_2 absorber was set in 1980, reaching 6% for Mg/Zn_3P_2 devices [2]. As-fabricated Mg/Zn_3P_2 solar cells exhibited V_{oc} values of <150 mV, but upon mild annealing at 100 °C in air the cells exhibited V_{oc} values of 500–600 mV. The good performance of Mg/Zn_3P_2 solar cells was unique among reported Zn_3P_2 devices, and chapter 5 explores in detail the effect of annealing on Mg/Zn_3P_2 devices.

To verify the quality of our Zn_3P_2 substrates, Mg/Zn_3P_2 Schottky diodes were fabricated from both undoped and phosphorus-doped (P-doped) Zn_3P_2 samples using procedures similar to those previously reported. A micrograph of a finished device is shown in figure 1.5. Mg films of thickness ≈200 nm were deposited by RF magnetron sputtering on Zn_3P_2 substrates that had been freshly etched in 2% Br_2 in methanol. Back contacts of Ag with ≈200 nm thickness were then deposited by vacuum evaporation. Using optical photolithography a series of devices with 0.25 mm^2 active area and arrays of 2 μm bus bars were patterned by etching through the Mg top contact with 25 mM EDTA*–3% H_2O_2 (aq, pH 10). As part of the photolithography

*ethylenediaminetetraacetic acid

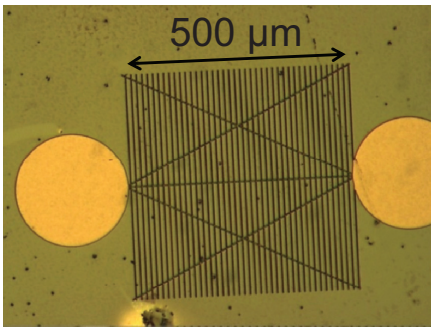

Figure 1.5. Optical micrograph of a microstructured Mg/Zn_3P_2 device showing the 2 µm wide bus bars in the active region of the device and the circular metal pads used to contact the device.

process, the Mg/Zn_3P_2 devices were heated to 120 °C for 5–10 min.

Both undoped and P-doped Zn_3P_2 wafers show significant photovoltaic response in Mg/Schottky diodes as illustrated in Figure 1.6. Cells made from undoped Zn_3P_2 wafers typically exhibited efficiencies of 1.0% to 1.5%, with V_{oc} reaching 550 mV, however a large series resistance prevented good current collection and high fill factors. The large bulk resistivity of the 500–600 µm thick undoped wafer is the primary contributor to the ∼1–10 kΩ series resistance. Cells made from P-doped Zn_3P_2 exhibited efficiencies between 4.0% and 4.5%, with better overall performance due to improved current collection and fill factor, but somewhat reduced V_{oc} values of 400 mV. The solar cell parameters of representative devices are given in table 1.1. The device results from Mg/Zn_3P_2 solar cells confirm the promise of Zn_3P_2 as an efficient solar absorber material.

Table 1.1. Photovoltaic parameters of Mg/Zn_3P_2 solar cells fabricated from undoped and white phosporus annealed (P-doped) Zn_3P_2 substrates

Sample	J_{sc} ($mA \cdot cm^{-2}$)	V_{oc} (V)	FF	η (%)
Undoped	8.5	0.55	0.29	1.38
Undoped	10.3	0.49	0.26	1.31
Undoped	9.1	0.50	0.29	1.30
P-doped	21.8	0.39	0.50	4.20
P-doped	21.4	0.41	0.51	4.48
P-doped	19.7	0.40	0.52	4.08
Record	14.9	0.49	0.71	5.96

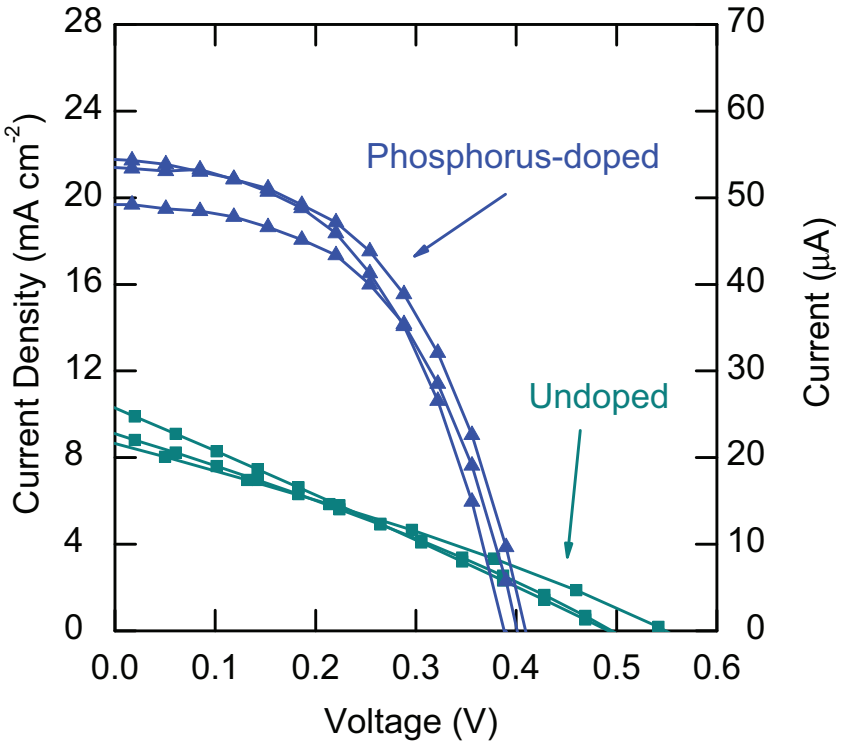

Figure 1.6. J–V performance of microstructured Mg/Zn_3P_2 devices under simulated 1 sun illumination and with 0.25 mm^2 device active area.

Chapter 2

High Purity Zn_3P_2 Substrates

This chapter explores the principles behind the formation of raw Zn_3P_2 from elemental zinc and phosphorus, the growth of large-grain crystals by physical vapor transport (PVT), and the metallographic processing of rough Zn_3P_2 wafers into 1–2 nm root-mean-square (RMS) roughness Zn_3P_2 substrates (figure 2.1). Analysis by x-ray diffraction (XRD) and inductively-coupled mass spectrometry (ICPMS) confirmed the synthesis of single phase α-Zn_3P_2 substrates with high purity (>99.999%).

2.1 Raw Zn_3P_2 Synthesis

Zn_3P_2 in high purity is not available commercially, although ~99.5% Zn_3P_2 can be obtained from Sigma Aldrich, Alfa Aesar, and other suppliers. For semiconductor applications, higher purity material is required to prepare Zn_3P_2 substrates with long minority carrier lifetimes and controlled doping properties. The raw Zn_3P_2 material used in this study was grown by a physical vapor transport (PVT) process [20, 21]. High purity red phosphorus chips and zinc shot (99.9999%) were combined at 850 °C

Figure 2.1. Images of the products in the crystal growth process of (left) raw Zn_3P_2 crystals, (center) large-grain polycrystalline boule of Zn_3P_2, and (right) diced Zn_3P_2 wafer.

to form Zn_3P_2 powders (figure 2.2). Products nominally sold as "red phosphorus" may actually be shipped as different allotropes of red phosphorus. From the diagram in figure 2.4, we suppose that low purity red phosphorus is amorphous and higher purity red phosporus is crystalline. The PVT reaction was conducted under passive vacuum in sealed quartz tubes and detailed procedures can be found in appendix A.

The two critical steps for obtaining quantitative yield of raw Zn_3P_2 crystals were converting the red phosphorus to P_4 and carbon coating the growth ampoules. Figure 2.3 shows the progression of yield of raw Zn_3P_2 crystals from attempted growth trials. Initial attempts yielded 0% to 20% by mass recoverable Zn_3P_2 product which was improved by separating the reactants and adopting a temperature sequence as depicted in figure 2.2. Once the temperature gradient and geometry was optimized to yield 90% to 100% by mass recoverable Zn_3P_2, ampoule bursting and collapse became problematic and resulted in many lost reactions between trials #80 and #100. Carbon coating the quartz ampoules was effective at preventing breached ampoules during the synthesis and enabled a robust synthetic route to Zn_3P_2.

2.1.1 Obtaining the Desired Phase

The reaction products from some of the initial trials showed many Zn–P products other than Zn_3P_2 and illustrated the importance of the temperature gradient and geometry for efficient synthesis. Although the Zn–P phase diagram contains a wide region of stability for Zn_3P_2, the behavior of elemental phosphorus is much more complicated. Phosphorus is known to exhibit a wide range of allotropes with the most distinct being white phosphorus, red phosphorus and black phosphorus. White phosphorus consists of tetrahedral P_4 molecules, has a high vapor pressure and is one of the most reactive forms of phosphorus. Red phosphorus is a polymer of phosphorus atoms that is kinetically stable in air and is most commonly available commercially. Orthorhombic black phosphorus is the most stable allotrope of phosphorus at room temperature and pressure and consists of a layered structure. At least 15 other allotropes of phosphorus have been described (see figure 2.4), and controlling the allotrope of the elemental phosphorus reactant is critical for obtaining quantitative

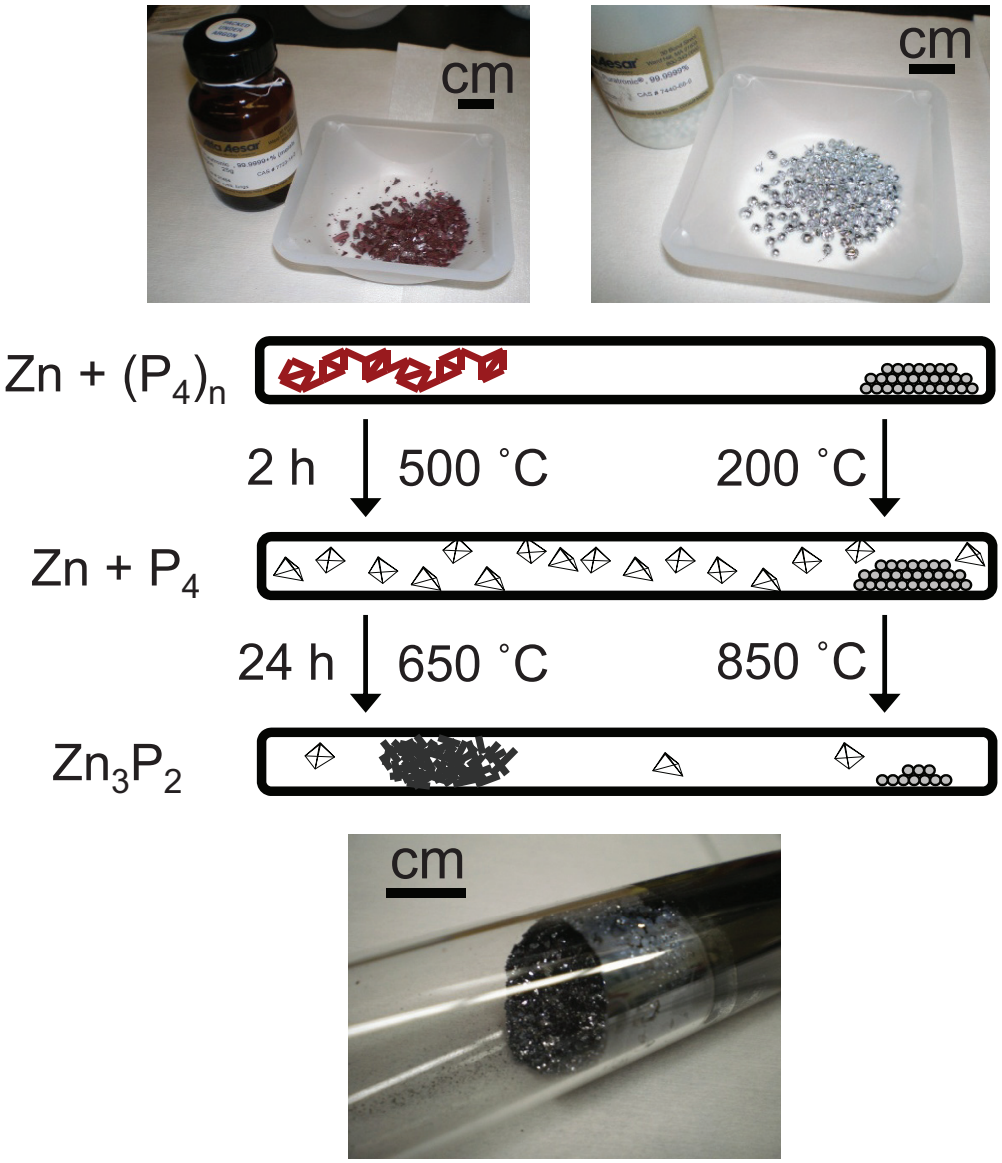

Figure 2.2. Schematic of the synthesis of Zn_3P_2 from elemental Zn and P showing first the conversion of red phosphorus to white phosphorus and then the sublimation of zinc to form Zn_3P_2.

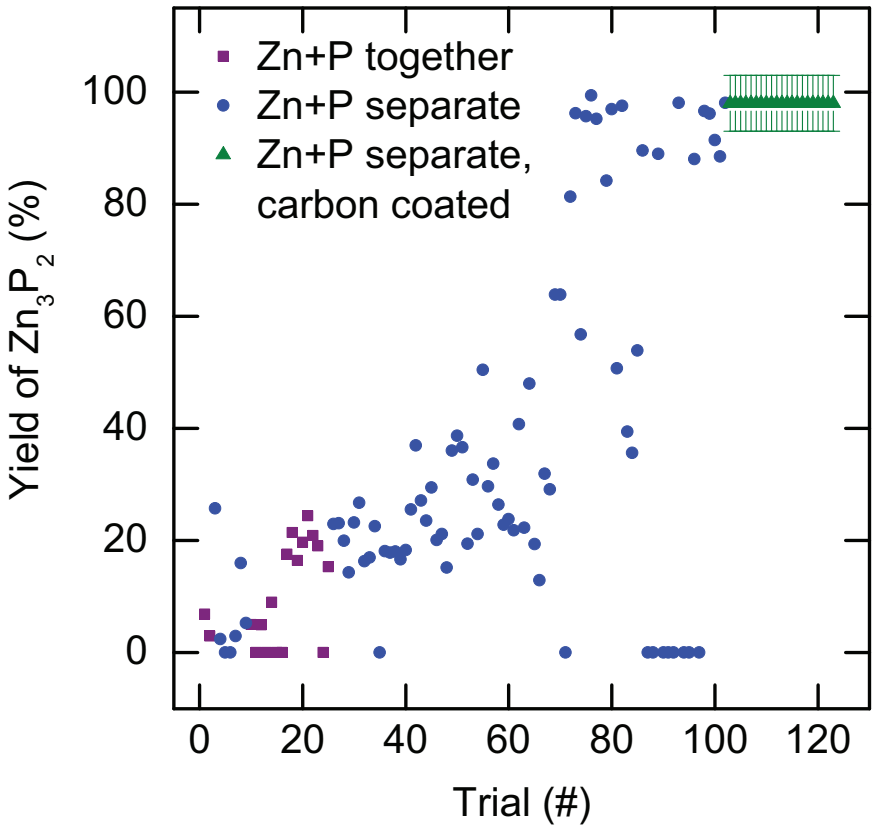

Figure 2.3. Mass yield of Zn_3P_2 by trial number for several types of synthesis improvements, where the conversion of red phosphorus to white phosphorus and carbon coating the growth zone played critical roles in acheiving high yield.

yield for metal phosphide synthesis [22].

Even with nominally the same heating procedure, an elemental zinc–phosphorus mixture did not necessarily result in phase-pure Zn_3P_2. The photographs in Figure 2.5 show the presence of red α-ZnP_2, black phosphorus, and unreacted zinc from growths that did not undergo quantitative yield of Zn_3P_2. Although some literature reports loaded the elemental zinc and phosphorus on the same end of the ampoule during synthesis [23], more control was obtained by keeping the elements at separate sides of the ampoule [20]. Phosphorus allotropes such as orthorhombic black and vitreous grey are known to form at the surface of metals, and the contact between red phosphorus and zinc metal surface may influence the progression of the reaction. By separating the elements, it was possible to gain independent control of the thermal processing of the elements and achieve quantitative yields of Zn_3P_2.

2.1.2 Ampoule Bursting and Collapsing

Improved yields were observed for a reaction sequence where the red phosphorus is heated to 550 °C for conversion to white phosphorus. For this step the temperature of the elemental zinc was not intentionally heated and remained in the range of 300 °C. Once the red phosphorus was fully converted to white phosphorus, a clear liquid was observed refluxing in the quartz ampoule. After this step, the elemental zinc side of the ampoule was heated to 850 °C to begin vaporizing the zinc, where it reacted in the gas phase to form Zn_3P_2. When the ampoule first reaches the higher temperature, it is under a high pressure and bursting of the quartz ampoule was likely to occur if too much phosphorus had been added or if the glass seals on the ampoule were weak. Ampoule bursting subjects the product and reactant mixture to oxygen at high temperatures, which results in the formation of P_2O_5 smoke and rapid oxidation of the Zn_3P_2 product. Ampoule bursting accounted for the data points with zero yield in figure 2.3.

Ampoule collapse upon cooling was more likely for growth trials with high yield than for growth trials with significant unreacted zinc metal and black phosphorus. The product Zn_3P_2 adhered strongly to the walls of the quartz ampoule, and the

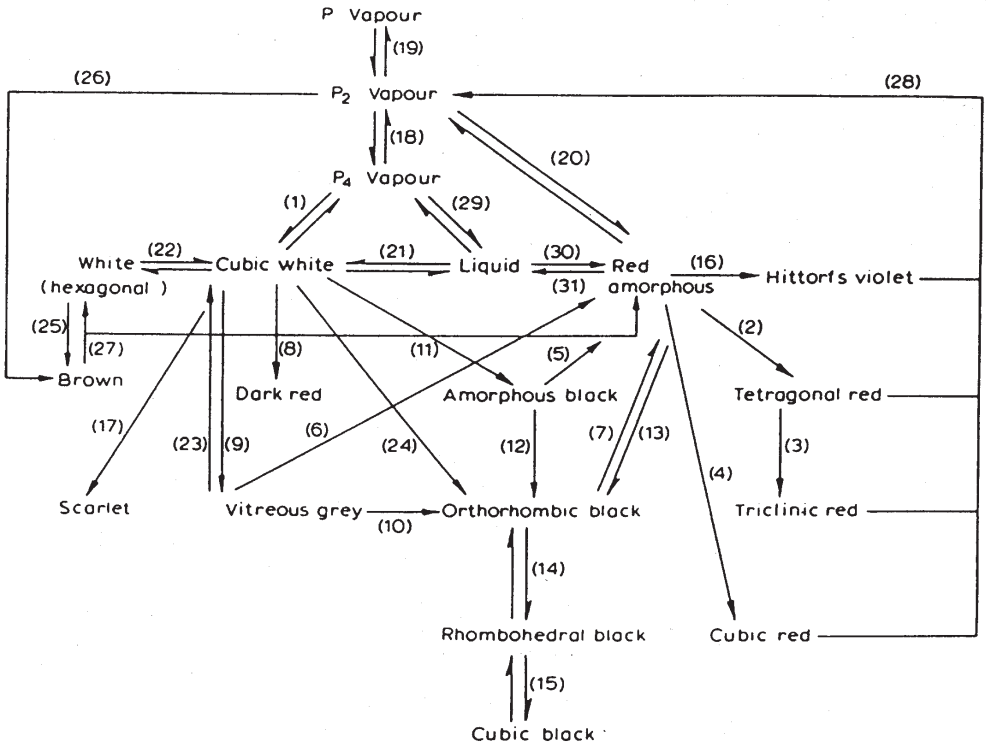

Figure 2.4. A schematic showing the interconversion conditions between allotropes of phosphorus. The depicted transitions occur under the following conditions: (1) room temperature, (2) 540 °C, (3) 550 °C, (4) 600 °C, (5) 125 °C, (6) 400 °C, (7) 500 °C, (8) 400 °C, (9) 380 °C with Hg or 250 °C at 12 kb, (10) 400 °C with Hg, (11) 200 °C at 12 kb, (12) 200 °C at 15 kb, (13) 200 °C at 12 kb, (14) 50–100 kb, (15) 100 kb, (16) recrystallize from Pb, (17) decompose PBr_3, (18) 900 °C, (19) 1700 °C, (20) low pressure, (21) 44.1 °C, (22) –77 °C (23) sublime in vacuo, (24) 220 °C at 12 kb, (25) –190 °C with UV light, (26) condense at –196 °C, (27) –100 °C, (28) heat in vacuo, (29) 280 °C, (30) 300 °C or UV light, (31) 600 °C [22].

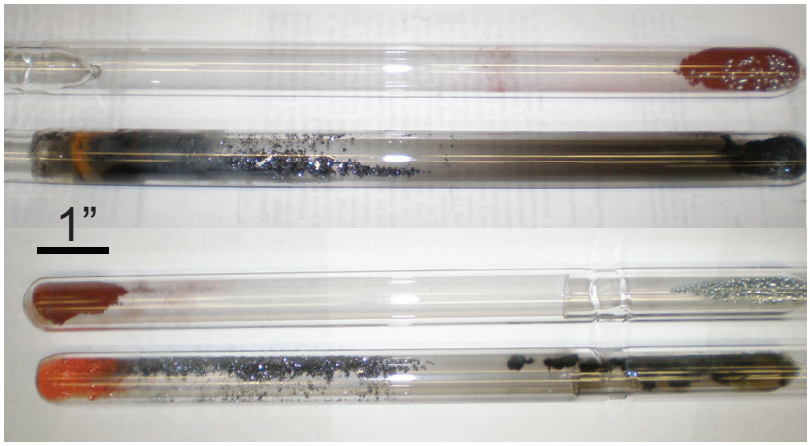

Figure 2.5. Photographs of ampoules containing reacted zinc and phosphorus: the top two pictures show the reaction of a mixture of phosphorus and zinc on the same end of the ampoule; the bottom two pictures show the reaction of phosphorus and zinc on the opposite sides of the ampoule. The silvery α-Zn_3P_2 phase is present in both reactions, along with unwanted red α-ZnP_2 and black phosphorus species.

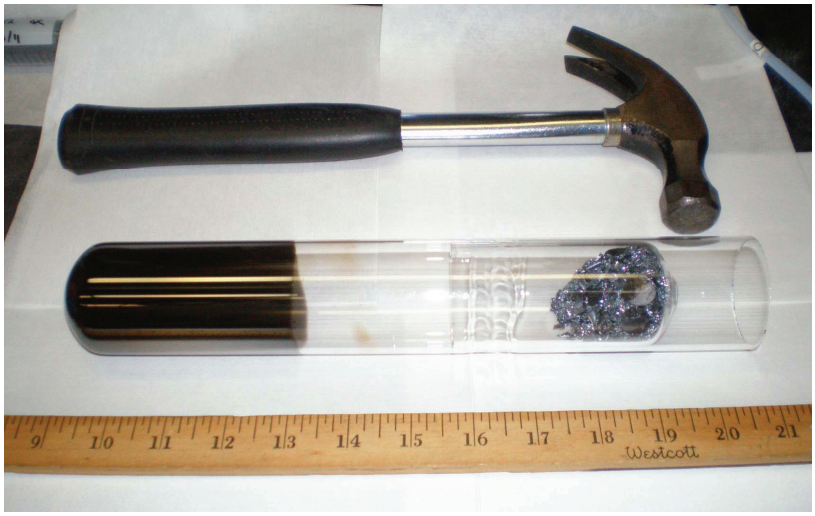

Figure 2.6. Photograph of a carbon coated purification ampoule where the right side contains raw Zn_3P_2 source material and the left side is carbon coated to reduce adhesion of purified Zn_3P_2.

higher coefficient of thermal expansion for Zn_3P_2 as compared to SiO_2 frequently applied enough strain to fracture the ampoule upon cooling. Even when the glass did not shatter, removing the adhered semiconductor material from the quartz was an arduous and hazardous task. In some cases, zinc metal or black phosphorus in the ampoule reduced the adhesion between Zn_3P_2 and SiO_2 by acting as a getter for the water and SiO that is outgassed by the quartz. When phase-pure Zn_3P_2 growth was acheived, adhesion between glass and Zn_3P_2 became a central challenge. Coating the growth ampoules with a layer of densified, amorphous carbon, as depicted in figure 2.6, provided both a chemical getter and a physical barrier to impede the adhesion of Zn_3P_2 and SiO_2.

With the proper geometry, temperature gradients and carbon coating, the synthesis of 20–30 g of high purity Zn_3P_2 material in each ampoule was straightforward. The raw Zn_3P_2 crystals were purified at least once by resubliming the Zn_3P_2 material in a fresh ampoule. The picture shown in figure 2.6 depicts 72 g of Zn_3P_2 loaded and ready for purification–enough material for hundreds of 1 cm^2 Zn_3P_2 substrates.

Inductively-coupled mass spectrometry (ICPMS) was employed to evaluate the purity of the elemental starting materials as well as raw and purified Zn_3P_2 crystals. Solutions were prepared for analysis by dissolving $\sim$10–100 mg of sample material in concentrated nitric acid that contained $<$10 ppt metal impurities. The mixtures were heated at 80 °C until the sample material completely dissolved, and then the solutions were diluted to 2% nitric acid by volume and 1–10 $g \cdot L^{-1}$ dissolved solids. Semiquantitative analysis by ICPMS of the solutions yielded rough impurity concentrations in units of $\mu g \cdot L^{-1}$ or $ng \cdot L^{-1}$ that were converted to units of $atoms \cdot cm^{-3}$ for comparison. Table 2.1 compiles the resulting impurity data for zinc shot, red phosphorus chips, raw Zn_3P_2, and purified Zn_3P_2. Most of the metal impurities in the raw Zn_3P_2 crystals were attributed to the zinc shot and red phosphorus chips starting material; Cu and Li impurities were attributed to the quartz ampoule itself.

Table 2.1. Compiled impurity analysis in units of atoms $\cdot$ cm^{-3} by inductively-coupled mass spectroscopy (ICPMS) of the starting elemental zinc, elemental phosphorus, raw Zn_3P_2, and sublimation-purified Zn_3P_2

Impurity	Zn "6N"	P "6N"	Raw Zn_3P_2	Sublimed Zn_3P_2
Ti	$<1 \times 10^{15}$	1.7×10^{18}	1.0×10^{18}	7.0×10^{17}
Se	2.2×10^{17}	$<1 \times 10^{15}$	1.3×10^{17}	1.2×10^{16}
Mg	9.8×10^{16}	$<1 \times 10^{15}$	5.8×10^{16}	6.2×10^{15}
Ag	2.9×10^{16}	$<1 \times 10^{15}$	1.7×10^{16}	9.5×10^{16}
Ga	1.0×10^{16}	$<1 \times 10^{15}$	7.4×10^{15}	1.8×10^{16}
Al	2.3×10^{17}	6.4×10^{16}	3.0×10^{17}	4.5×10^{16}
Cu	6.9×10^{16}	5.5×10^{16}	1.1×10^{17}	1.8×10^{17}
Li	1.1×10^{15}	3.2×10^{15}	4.6×10^{16}	7.7×10^{17}
Total	6.6×10^{17}	1.8×10^{18}	1.7×10^{18}	1.8×10^{18}
Bulk	6.6×10^{22}	4.5×10^{22}	5.2×10^{22}	5.2×10^{22}
Purity (%)	99.9960	99.9990	99.9968	99.9965

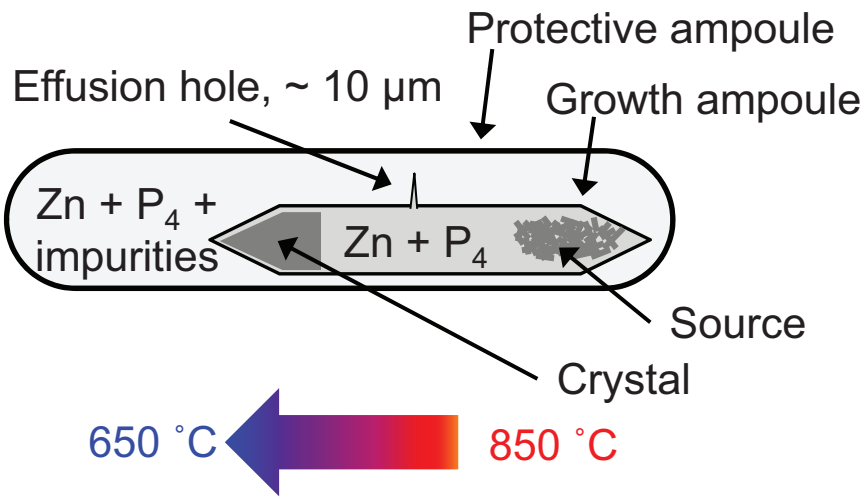

Figure 2.7. Schematic of nested ampoule method for Zn_3P_2 crystal growth (detailed procedures in appendix A).

2.2 Crystal Growth

The purified Zn_3P_2 material was used as source material for growing large-grain polycrystalline boules appropriate for dicing, lapping and polishing into Zn_3P_2 substrates. Polycrystalline boules 1 cm in diameter and 4 cm in length, with grain sizes of ~1–10 mm^2 were prepared by physical vapor transport in horizontal Bridgman-type quartz ampoules (figure 2.7). Carbon coating was also important to prevent crystal adhesion to the ampoule that can crack the Zn_3P_2 crystal upon cooling. Approximately 10 g of Zn_3P_2 were loaded and the ampoule was translated at a rate of 1–2 $mm \cdot h^{-1}$ for several weeks into the cold zone of the furnace held at 850 °C.

2.2.1 Obtaining Bulk α-Zn_3P_2 Crystals

The physical vapor transport process used to produce large Zn_3P_2 was first performed in a single sealed ampoule under passive vacuum. The first growths were conducted with ~10% excess phosphorus in the ampoule with the goal of preventing phosphorus loss due to black phosphorus formation. However, under the conditions of crystal growth, portions of the crystal formed as α- and β-ZnP_2 phases in addition to the desired Zn_3P_2 phase. Scanning electron microscopy (SEM) and energy dispersive

Figure 2.8. Images of diced wafers of (left) mixed-phase α-ZnP_2, β-ZnP_2, and α-Zn_3P_2, (center) α-Zn_3P_2 with a high density of voids, and (right) large-grain polycrystalline α-Zn_3P_2. The displayed wafers have diameters of 1 cm.

x-ray spectroscopy (EDS) confirmed the stoichiometry of the regions. The photograph on the left in Figure 2.8 shows red α-ZnP_2 and black β-ZnP_2 on the outer portion of the substrate and silver α-Zn_3P_2 in the center region. By using only <0.2% excess phosphorus, phase-pure α-Zn_3P_2 was obtained.

2.2.2 Preventing Voids in the Crystal

Crystal growth by PVT in a single ampoule proceeded at slower rates as gas-phase impurities built up during the growth [20]. Water and SiO were outgassed by the quartz at elevated temperature and accumulated as inert impurities in the ampoule. If the ampoule was pulled into the growth zone of the furnace faster than the crystal can grow, voids formed in the crystal. Often only portions of the final polycrystalline boule exhibited voids and the rest of the boule consisted of solid Zn_3P_2. The photograph in the center in figure 2.8 shows a diced wafer containing phase-pure α-Zn_3P_2 with a high density of voids.

One approach to preparing crystals without voids was vacuum annealing the quartz ampoule before loading. Vacuum annealing reduced the amount of water and SiO that was outgassed during the crystal growth and was performed under <10 mTorr vacuum at 1000 °C for 4 h. After vacuum annealing treatment of the quartz ampoule, crystals grew with fewer voids. Slowing down the pulling speed for the ampoule to <1 $mm \cdot h^{-1}$ was also an effective method of preparing solid boules.

With reduced pulling speed the single ampoule process still formed solid boules without any voids, with the disadvantage that growth times took as long as 1–2 months.

Further success was obtained by using the nested ampoule technique described by Catalano [24]. In this technique, an outer protective ampoule surrounds the growth ampoule and the two chambers are connected by a 10–40 μm diffusion hole. The role of the diffusion hole is to reduce the partial pressure of species other than Zn and P_4 in the growth zone. By employing the nested ampoule technique, the growth rate was increased to 1–2 $mm \cdot h^{-1}$ and the formation of voids was significantly reduced. The drawback of using a diffusion hole was that some fraction of the Zn_3P_2 source material was lost to the outer tube and was not incorporated into the final crystal. Thus the crystals grown by the nested ampoule technique yielded ∼30% fewer wafers for a given mass of source material, but with growth times of 1–2 weeks. Figure 2.1 shows photographs of a high quality crystalline boule of Zn_3P_2 as well as a diced wafer.

2.3 Metallographic Processing

This section details how to process diced Zn_3P_2 wafers into Zn_3P_2 substrates with 1–2 nm root-mean-square (RMS) roughness. The rough wafers were lapped with 20 μm alumina abrasive films and polished with a sequence of 6, 3, 1, and 0.25 μm diamond pastes to yield Zn_3P_2 substrates with a specular finish. Lapped substrates had a diameter of 1 cm, thickness of 500–600 μm and root-mean-square (RMS) surface roughness of 2–3 nm by atomic force microscopy (AFM). The substrates were then etched for 30 s in 2% Br_2 in methanol as a final chemical polish that yielded RMS roughness values of 1–2 nm by AFM. Etching with Br_2 in methanol was effective at removing native oxides and was measured to have a bulk etch rate of ∼30 $nm \cdot s^{-1}$. X-ray diffraction (XRD) patterns collected using copper K-α x-rays showed the wafers to be highly crystalline, phase-pure α-Zn_3P_2 (figure 2.9).

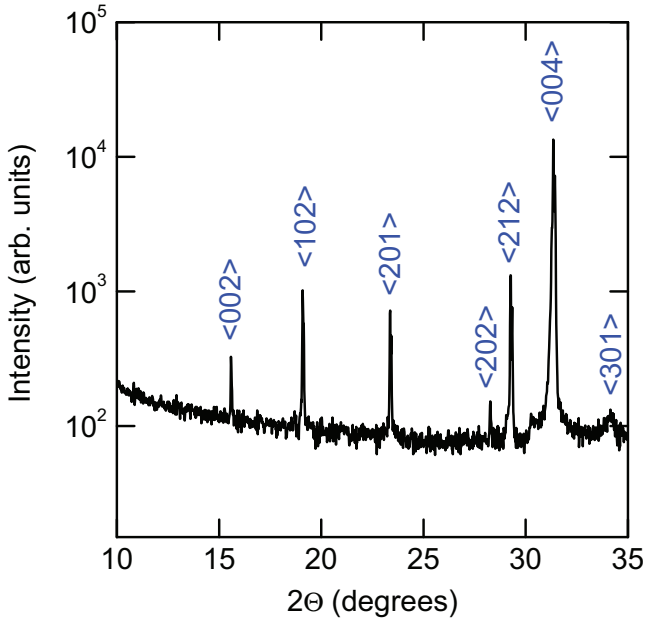

Figure 2.9. X-ray diffraction of polished Zn_3P_2 substrate showing phase-pure α-Zn_3P_2.

2.3.1 Obtaining a Specular Finish

The diced wafers of Zn_3P_2 at first exhibited surface roughness in the 10s of μm, and processing the wafer to a specular finish was made challenging by the orientation-dependent fracturing of Zn_3P_2. Grains of certain orientations exhibited a higher density of macroscopic pitting even when adjacent grains had a specular finish. The pitting damage consisted of ∼2–20 μm voids in the surface of the wafer and persisted as material was removed from the wafer. Figure 2.10 shows micrographs of typical orientation-dependent pitting damage in Zn_3P_2 wafers.

Abrasive suspensions and abrasive films provided two basic approaches for obtaining a specular finish. Among the abrasive suspensions, aqueous and nonaqueous alumina as well as nonaqueous diamond suspensions were attempted but nonaqueous diamond pastes were found to work the best. Unfortunately, the removal of most of the pitting damage required polishing times of 4–6 h per wafer to obtain a specular finish. Zn_3P_2 substrates that were polished with 6, 3, 1, and 0.25 μm diamond pastes showed RMS roughness in the 2–3 nm range, as shown by AFM scans in figure 2.11.

Abrasive films such as SiO_2 or SiC paper were useful for rapidly removing material for thickness control, but the distribution of abrasive particle size and the detachment of abrasive particles prevented these films from obtaining a specular finish. Alumina or diamond abrasive films showed much less abrasive detachment and higher abrasive uniformity. However even with careful use of diamond abrasive films the grain-dependent pitting was still apparent (figure 2.10).

Lapping with alumina abrasive films of 20 μm, followed by diamond abrasive film of 9, 6, 3, and 1 μm was sufficient to reach a specular finish. The lapping procedure based on diamond abrasive films was effective at preparing Zn_3P_2 substrates with a specular finish in 20–30 min which constituted a dramatic improvement over the 4–6 h required to polish with diamond pastes.

2.3.2 Final Polishing

To prepare substrates with ∼1 nm RMS roughness, wafers with a specular finish were subjected to a final polishing treatment. The three most useful approaches for final polishing were a mechanical polish with SiO_2 nanocrystalline slurry, a chemical-mechanical polish (CMP), and a Br_2 in methanol chemical polish.

The SiO_2 nancrystalline slurry appeared to give a good finish, but removing the residual SiO_2 particles proved difficult. Rinsing, sonicating, and/or wiping with detergent solutions were not effective for removing all of the SiO_2 particles. Future investigations could employ an HF dip to remove the nanocrystalline SiO_2 abrasive particles.

CMP with 0.05% Br_2 in methanol solutions or aqueous hypochlorite solutions were also attempted as a final polish. The dilute Br_2 in methanol solution showed promise for attaining smooth surfaces, but chemical compatability between the solvent, fabric pad and adhesives remained an issue. Also, the additional personal hazard of employing Br_2 in methanol for polishing was another disadvantage. Aqueous hypochlorite CMP resulted in significant differential etching of the grain structure in Zn_3P_2 substrates, although the overall smoothness within a grain was specular and the pitting appeared to be limited.

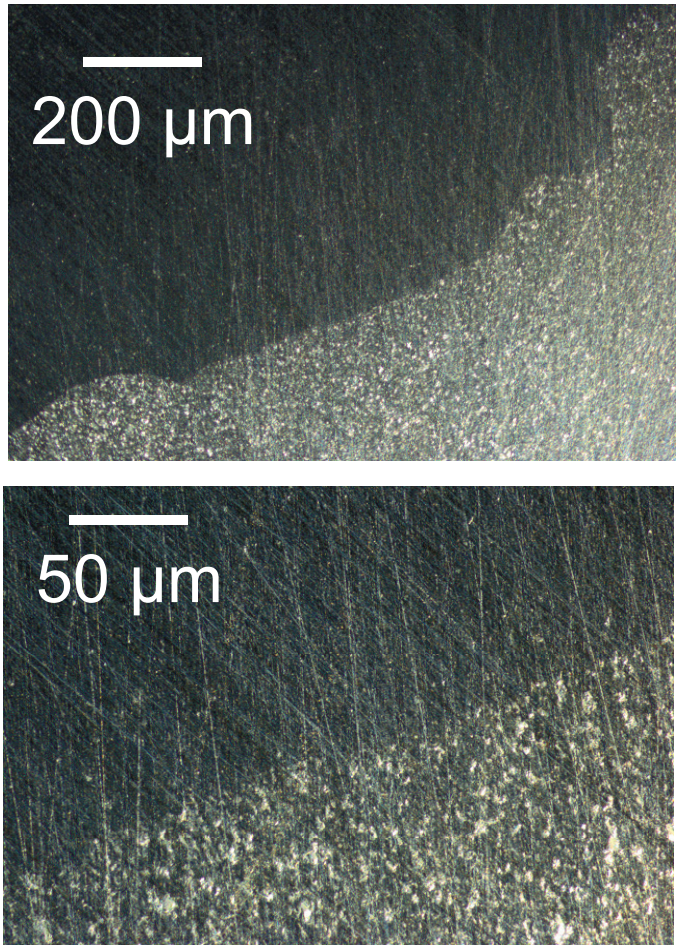

Figure 2.10. Microscope images of partially lapped Zn_3P_2 substrates showing orientation-dependent damage due to microfracturing.

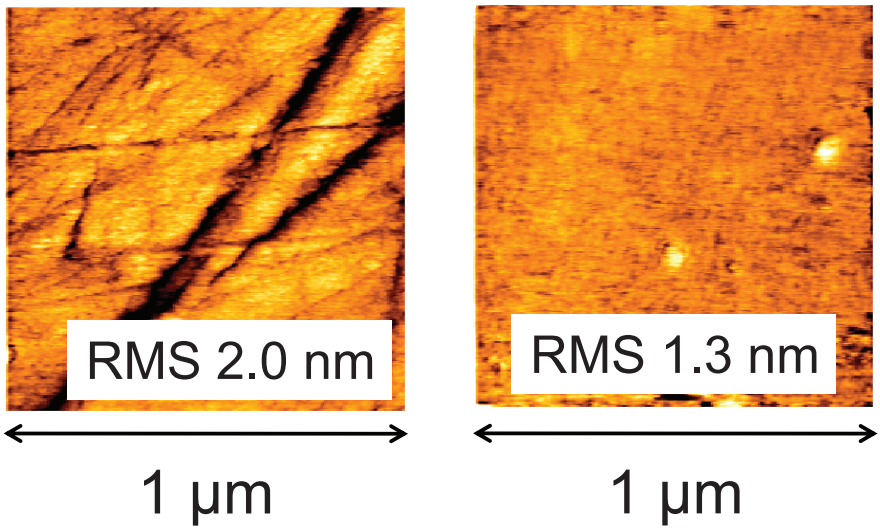

Figure 2.11. Surface roughness as measured by atomic force microscopy (AFM) of Zn_3P_2 substrates that were (left) polished with diamond pastes to 0.25 μm grit size and (right) polished with diamond pastes to 0.25 μm grit size and etched in 2% Br_2 in methanol for 30 s.

A 2% Br_2 in methanol chemical etch appeared to reduce the RMS roughness to ∼1 nm, as shown by the AFM scans in figure 2.11. The rapid etch rate observed for 2% Br_2 in methanol reduced the RMS roughness for the first tens of seconds, although longer times appeared to produce some mottling of the surface similar to the "orange-peel" effect reported for some compound semiconductors [25].

The Zn_3P_2 substrates resulting from these procedures were quasi-single crystal α-Zn_3P_2 substrates with 1–10 mm^2 grain size, >99.999% purity, and 1–2 nm RMS roughness. The steps outlined in this chapter and detailed in appendix A provide a direct route for producing high quality Zn_3P_2 substrates from elemental zinc and phosphorus starting materials.

Chapter 3

Bulk Optoelectronic Properties of Zn_3P_2

The steady-state photoluminescence spectra of zinc phosphide (Zn_3P_2) wafers have revealed a fundamental indirect band gap at 1.38 eV, in close proximity to the direct band gap at 1.50 eV. These values are consistent with the values for the indirect and direct band gaps obtained from analysis of the complex dielectric function deduced from spectroscopic ellipsometric measurements. Bulk minority carrier lifetimes of 20 ns were observed by time-resolved photoluminescence decay measurements, implying minority carrier diffusion lengths of $\geq$7 μm. Controlled p-type doping in the range of 10^{13}–10^{18} holes $\cdot$ cm^{-3} and hole mobility values of 15–20 cm$^2 \cdot$ V$^{-1} \cdot$ s^{-1} were demonstrated, confirming the nearly ideal bulk optoelectronic properties of Zn_3P_2 for photovoltaic applications.

3.1 Introduction

Zinc phosphide (Zn_3P_2) has significant potential as an absorber in thin film photovoltaics. Zn_3P_2 has been reported to have a direct, 1.5 eV band gap, high ($>10^4$–10^5 cm^{-1}) light absorbance in the visible region [1], and long (5–10 μm) minority carrier diffusion lengths [26]. To date, Zn_3P_2 has been produced almost exclusively with p-type doping [27], preventing the fabrication of *p-n* homojunctions. Solar cells using Zn_3P_2 have therefore been constructed from Schottky contacts, *p-n* semiconductor heterojunctions [13, 14, 15], or liquid contacts [16, 17], with p-Zn_3P_2/Mg Schottky diodes having exhibited 6% solar energy conversion efficiency [2].

However, even the basic materials parameters of Zn_3P_2, such as the energy gap, remain controversial. A direct interband transition has been observed at ≈1.5 eV, but

the more gradual decline in absorption between 1.3 and 1.5 eV indicates that either an indirect gap and/or a defect band contributes to the absorption tail [28, 29, 30, 31, 32, 33]. Some absorption measurements have led to assignments of the fundamental band gap as direct [28, 29, 30] whereas others have concluded that the fundamental gap is indirect [31, 32, 33]. Computational methods using empirical pseudopotentials have also yielded both direct [11, 12, 34] and indirect [12, 35] transitions at the fundamental band gap, depending whether the Zn_3P_2 lattice is modeled as a cubic antifluorite or as a tetragonal structure. A fundamental indirect gap is supported by investigations of the spectral response properties of Mg Schottky diodes [36] and of aqueous photoelectrochemical cells [16], which have produced estimates of an indirect gap at 1.37 and 1.43 eV, respectively.

3.2 Band Gap and Optical Absorption

To better elucidate the band structure of Zn_3P_2, we have performed steady-state photoluminescence (PL) measurements of Zn_3P_2 near room temperature. In addition, we report spectroscopic ellipsometric data on Zn_3P_2 and the n(ω), k(ω) spectra derived therefrom. Both PL measurements and $\alpha(\omega)$ data are consistent with the assignment of the fundamental indirect band gap at 1.38 eV and the direct band gap at 1.50 eV.

3.2.1 Steady-State Photoluminescence Measurements

Photoluminescence (PL) measurements provide a sensitive means of probing semiconductor band structure, defect energies and recombination dynamics. To perform PL measurements, laser emission is focused on a semiconducting substrate where the laser emission photon energy is greater than the semiconductor band gap. The laser excitation is strongly absorbed in the semiconductor and generates electron-hole pairs that quickly thermalize to the band edge energy of the semiconductor. The thermalized electron-hole pairs can engage in radiative recombination, whereby the energy of the electron-hole pair is converted to a photon with approximately the energy of the semiconductor band gap. Analysis of the spectrum of photon emitted

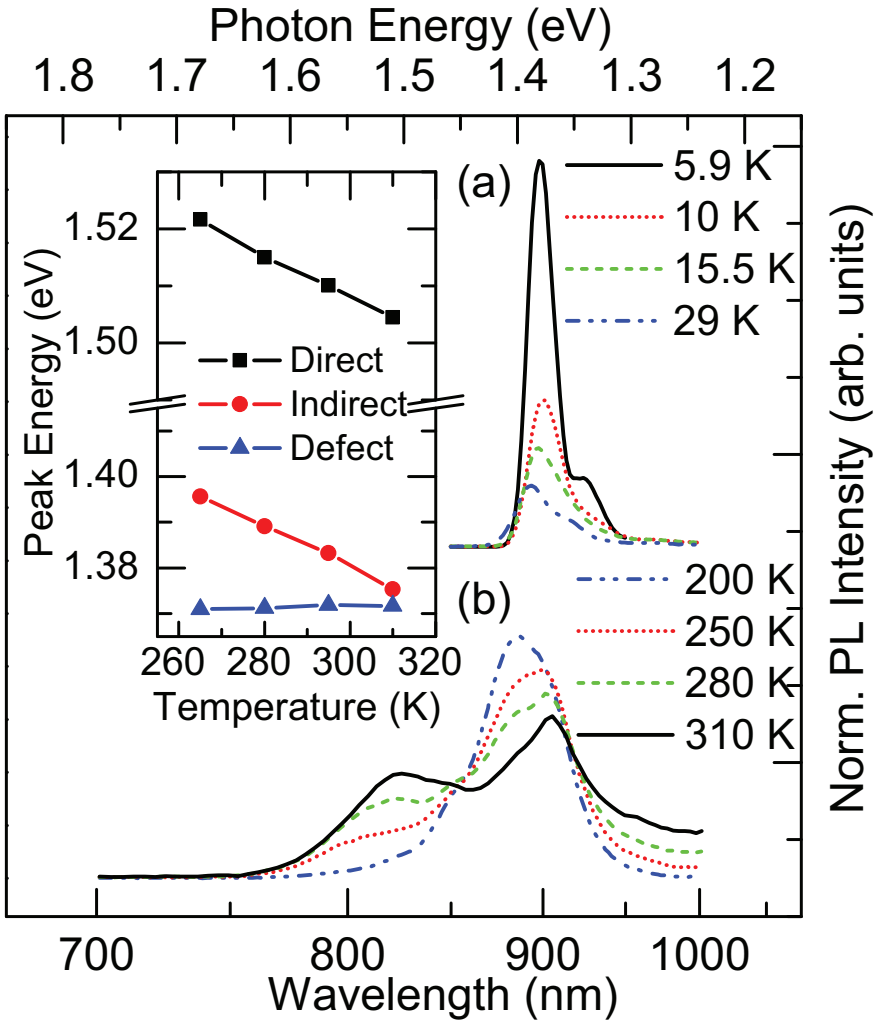

Figure 3.1. Normalized PL spectra of Br_2-etched Zn_3P_2 substrates in the temperature ranges (a) 5.9–29 K and (b) 200–310 K. The inset shows the energies, as a function of temperature, of the direct and indirect interband transitions, as well as a defect-assisted transition.

by radiative recombination yields precise information about the band structure of the semiconductor.

PL measurements were collected using Zn_3P_2 substrates that had been freshly etched in 2% Br_2 in methanol for 30 s, rinsed in methanol and immediately loaded into a closed-cycle cryostat that was then evacuated to 5×10^{-6} Torr. For steady-state PL measurements, excitation was performed using the 488 nm line of an Ar-ion laser that was chopped at 10 kHz using an acousto-optic modulator. The emission was passed through a monochromator and focused onto an infrared photomultiplier tube, and the PL signal was monitored using a lock-in amplifier. The closed-cycle cryostat allowed for ± 1 °C control of the temperature of the Zn_3P_2 substrates and was loaded with either liquid nitrogen or liquid helium depending on the desired operating temperature. Liquid helium transfer was performed directly from 60 L dewars using the pressure from a separate helium cylinder to push the cryogen through a vacuum-insulated transfer line. Low temperature PL measurements were performed in between dosing the cryostat with the cryogen.

Between 5 and 20 K, Zn_3P_2 samples exhibited an intense PL signal at 1.36 eV, as well as a phonon replica at 1.32 eV (figure 3.1, upper panel). The 43 meV energy of the phonon is in agreement with the longitudinal optical phonon observed in previous low-temperature PL studies of Zn_3P_2 [37]. Between 200 and 310 K, steady-state PL spectra showed a peak near 1.4 eV, along with a shoulder at $\approx$1.5 eV that became more prominent at higher temperatures (figure 3.1, lower panel). In addition to the two main peaks, a smaller feature at 1.37 eV that saturated at higher excitation intensity, was observed, as would be expected for defect luminescence. A small feature at 1.30 eV was produced by a diffracted laser line.

Fitting of the data obtained at a range of laser excitation intensities at each temperature yielded precise positions of the centers of the PL peaks. At room temperature, the two main peaks were centered at 1.38 ± 0.01 eV and 1.50 ± 0.01 eV (figure 3.1, inset). With decreasing temperature, the peaks centered at 1.38 and 1.50 eV exhibited blue shifts of -3.8×10^{-4} and -4.5×10^{-4} eV $\cdot$ K^{-1} respectively, broadly consistent with the well-documented energy gap changes of III–V compound semi-

conductors [38].

As observed previously [37], at cryogenic temperatures, the PL signal exhibited a significant blue shift as the laser excitation intensity was increased. In contrast, near room temperature, the centers of the peaks at 1.38 and 1.50 eV did not change with increasing pump power (figure 3.2). The lack of a shift in the centers of 1.38 and 1.50 eV peaks in response to increasing pump power suggests a high density of states in the Zn_3P_2 and is consistent with these signals being derived from interband transitions. Hence, at room temperature, the steady-state PL spectra was ascribed to luminescence from both the fundamental indirect gap at 1.38 eV and the nearby direct gap at 1.50 eV. Similar direct and indirect gap PL features have been reported for room temperature radiative recombination in germanium [39], which is a material with a fundamental indirect transition at 0.66 eV and a direct interband transition at 0.80 eV.

3.2.2 Spectroscopic Ellipsometry

Spectroscopic ellipsometry was performed at an angle of incidence of 50°, 60°, and 70°, respectively, for 300 nm $< \lambda <$ 2200 nm with a Xe lamp visible light source and a Fourier-transform infrared spectrometer. The $\Psi(\omega), \Delta(\omega)$ (amplitude ratio and phase shift, respectively, of the reflectance at frequency ω) behavior obtained from spectroscopic ellipsometric measurements on bulk Zn_3P_2 substrates was used to generate values for the refractive index, $n(\omega)$, and extinction coefficient, $k(\omega)$, functions of Zn_3P_2. The $\Psi(\omega), \Delta(\omega)$ data were converted to $n(\omega)$, $k(\omega)$ values assuming a bulk, isotropic substrate. Inclusion of a 1–2 nm overlayer in the model, to account for surface roughness and chemical overlayers, was not found to materially affect the derived $n(\omega)$, $k(\omega)$ data.

Figure 3.3a shows representative $n(\omega)$, $k(\omega)$ data for Zn_3P_2 substrates over the 0.5–4.1 eV spectral range. The $n(\omega)$, $k(\omega)$ data indicated that Zn_3P_2 has a very high optical absorption, with $\alpha > 10^4$ cm^{-1} throughout the visible region. The feature in the $n(\omega)$, $k(\omega)$ data at 2.5 eV indicated a high density of states, perhaps associated with a higher lying band at the Γ_{25} point (figure 1.3). The complete $n(\omega)$, $k(\omega)$ data

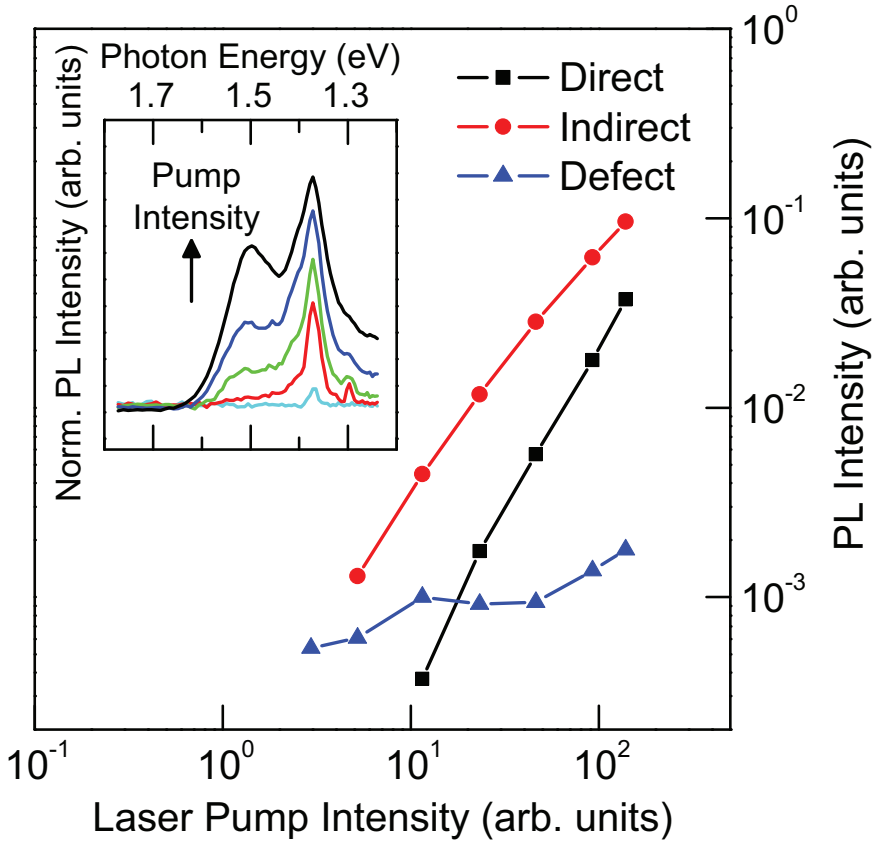

Figure 3.2. Relative intensities of the direct gap, indirect gap and defect-assisted PL of Br_2-etched Zn_3P_2 substrates as a function of laser pump intensity at 295 K. The inset shows the normalized PL spectra across the same range of laser pump intensities.

set extending through the visible and near infrared spectrum was valuable for device characterization and modeling of Zn_3P_2 solar cells. For example, section 5.3 uses the k(ω) data set to estimate the minority carrier diffusion length in ITO/Mg/Zn_3P_2 solar cells from spectral response measurements.

The derived spectral data for the absorption coefficient function, $\alpha(\omega)$, for Zn_3P_2 indicated a direct transition at 1.49 $\pm$ 0.03 eV (figure 3.3b) and an indirect transition at 1.31 $\pm$ 0.05 eV (figure 3.3c). The $\alpha^{1/2}$ plots versus energy shows linear regions associated with both phonon absorption, $\alpha_a^{1/2}$, and emission, $\alpha_e^{1/2}$, yielding $E_{\mathrm{g}} + E_{\mathrm{p}}$ and $E_{\mathrm{g}} - E_{\mathrm{p}}$ intercepts that indicated $E_g = 1.31 \pm 0.05$ eV and $E_p = 0.04 \pm 0.02$ eV. The linearity of the α^2 and $\alpha^{1/2}$ plots versus energy is consistent with the presence of both direct and indirect gaps, but the resolution for extinction measurements at low values of k (<0.07) made the values of the band gap energies determined by spectroscopic ellipsometry less precise than those derived from the PL data.

3.3 Minority Carrier Lifetime and Diffusion Length

To measure minority carrier lifetimes in Zn_3P_2 substrates, time-resolved PL measurements were performed. Time-resolved PL measurements provide information about both surface and bulk recombination rates, and in this section we will focus on the PL decay dynamics >10 ns after the laser excitation pulse when the decay rate is most sensitive to bulk recombination rates. Section 4.3.2 contains detailed analysis of PL decay data to extract both a surface recombination velocity and a bulk minority carrier lifetime. Time-resolved PL measurements of Br_2-etched Zn_3P_2 substrates were performed at 10 kHz with 70 ps, 355 nm pulses produced by frequency-tripling of regeneratively amplified, mode-locked Nd:YAG laser pulses. The emission was collected using a fiber optic and the signal was integrated using a streak camera.

Time-resolved PL measurements at room temperature were fit by a double exponential decay, with time constants of 4 and 20 ns describing the decay behavior for

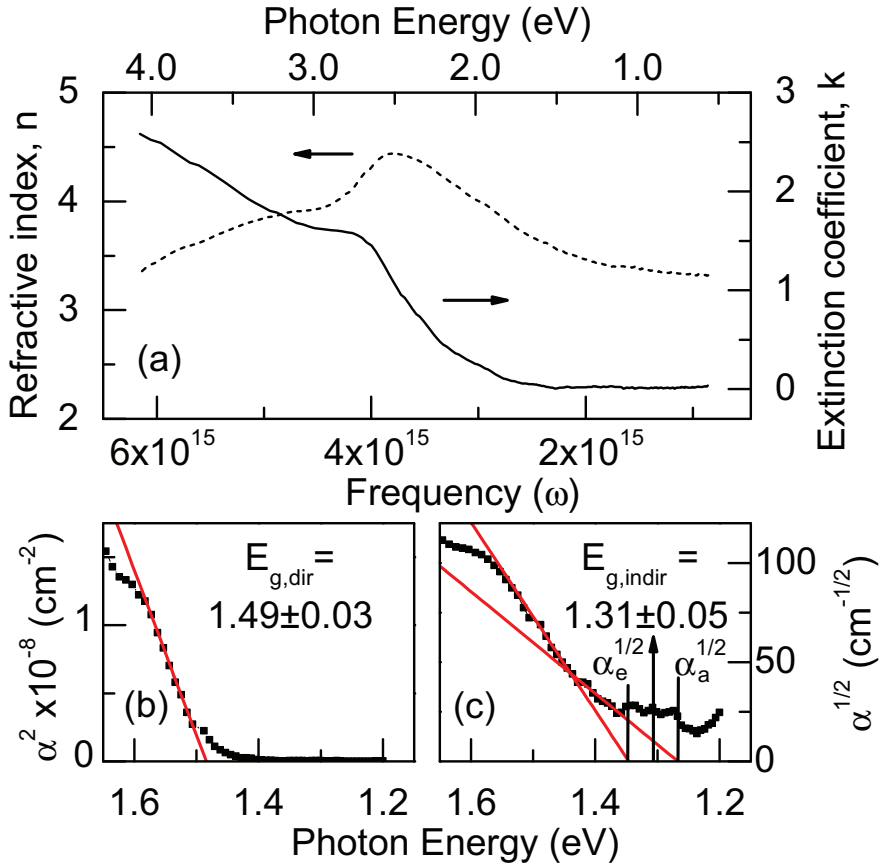

Figure 3.3. Spectroscopy ellipsometric analysis of Br_2-etched Zn_3P_2 wafers at 295 K showing (a) the derived n(ω), k(ω) data in the spectral range 0.5–4.0 eV; (b) the test of $\alpha(\omega)$ for direct transitions; and (c) the test of $\alpha(\omega)$ for indirect transitions.

excitation levels of 0.5–10 nJ $\cdot$ pulse^{-1} (figure 3.4). The double exponential behavior suggested that these time constants were related to both bulk and surface recombination processes. Minimal surface potentials have been reported for Br_2-etched Zn_3P_2 [14], so the recombination processes represented by the TRPL did not likely contain a field component even under low level injection. The Zn_3P_2 wafer strongly absorbed the 355 nm pump light with a 90% absorbance depth of $\sim$8 nm. The high concentration of photogenerated carriers near the surface resulted in an observed PL decay rate that was dominated by surface recombination in the first $\sim$10 ns after the laser pulse. After the first $\sim$10 ns, the observed PL decay rate was dominated by bulk recombination and corresponded to a bulk minority carrier lifetime of 20 ns. Hence, assuming an electron mobility of 1000 cm$^2 \cdot$ V$^{-1} \cdot$ s^{-1} [36], the measured minority carrier recombination lifetimes corresponded to minority carrier diffusion lengths of $\geq$7 μm, which is sufficient for unity internal quantum yields across the visible spectrum. The long minority carrier diffusion lengths inferred from the time-resolved PL measurements highlight the favorable material properties of Zn_3P_2 for photovoltaic applications.

3.4 Majority Carrier Density and Mobility

Controlling the p-type doping from the 10^{13} to 10^{18} cm^{-3} hole density of Zn_3P_2 has been accomplished by intrinsic phosphorus doping and by extrinsic Ag doping. Zn_3P_2 substrates without intentional doping typically show resistivity in the 10^4 $\Omega \cdot$ cm range, but these values can be reduced to 1–10 $\Omega \cdot$ cm by annealing in elemental phosphorus. Further increases in carrier density to values approaching 10^{18} holes $\cdot$ cm^{-3} can be accomplished by introducing Ag to the crystal. For both types of samples, hole mobilities have been measured in the 15–20 cm$^2 \cdot$ V$^{-1} \cdot$ s^{-1} range. Attempts to prepare n-type Zn_3P_2 by doping with chalcogens such as S, Se, and Te have only yielded high resistivity, presumably compensated, material.

Hall effect measurements were used to evaluate the bulk majority carrier density and mobility for Zn_3P_2 substrates. Figure 3.5 shows a schematic of the method for performing Hall effect measurements. Doped Zn_3P_2 substrates of dimensions 5$\times$5 mm

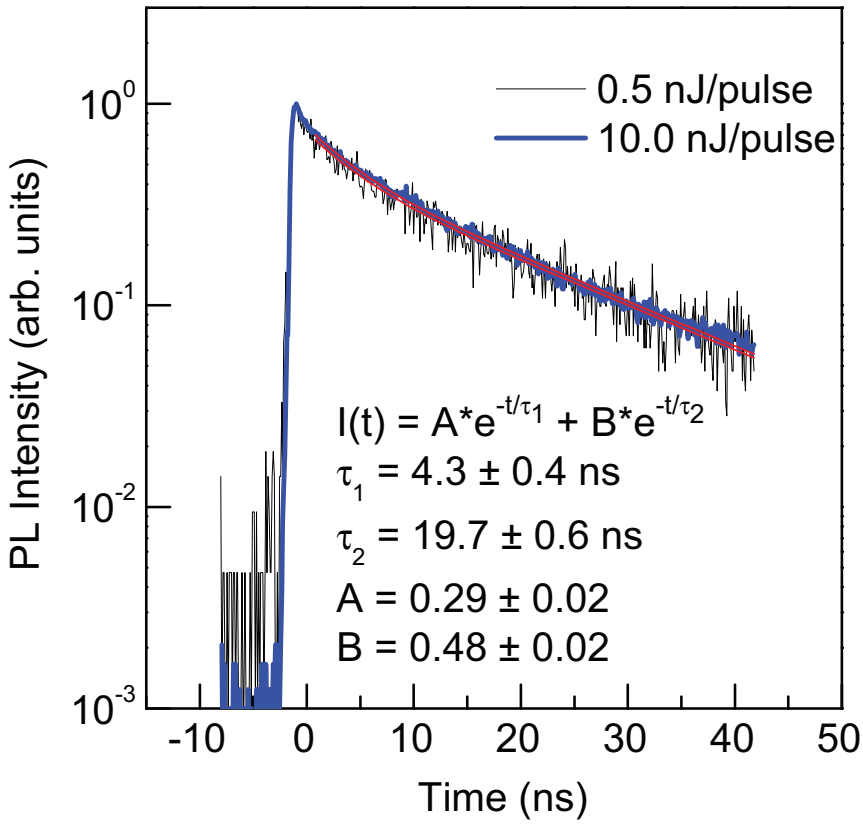

Figure 3.4. Time-resolved PL decay measurements of Br_2-etched Zn_3P_2 substrates at 295 K, showing double exponential decay behavior.

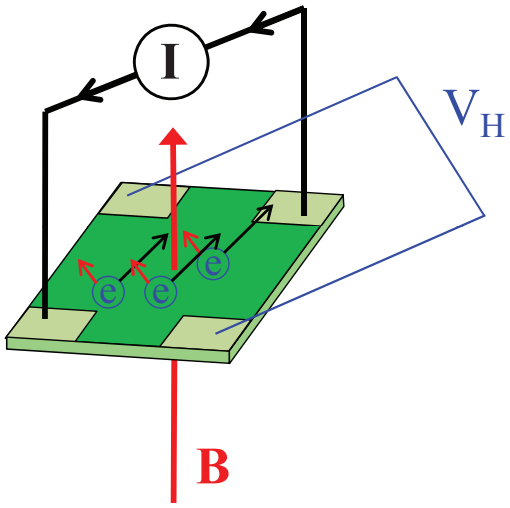

Figure 3.5. Schematic representation of Hall effect measurements, where a current (black, I) is sourced orthogonal to a magnetic field (red, B) that results in a Hall voltage orthogonal to both (blue, V_H).

or 2.5×2.5 mm were scribed in the corners and pressed with indium metal to make four ohmic contacts. The substrates were then contacted electrically with a probe station and placed inside an electromagnet with 1.4 tesla maximum magnetic field.

A current is sourced between two opposite contacts, and the orthogonal voltage is monitored across the other contacts. For an ideal sample under zero magnetic field, the voltage orthogonal to the sourced current should be zero. When a magnetic field is applied normal to the plane of the sample, however, the charge carriers are affected by the magnetic field and create a voltage orthogonal to the sourced current. The effect of changing magnetic field on the voltage orthogonal to the sourced current alows one to calculate the charge carrier type and mobility. Four-point Van der Pauw measurements on the same sample yield resistivity values that are used to compute the carrier density from the carrier mobility [40].

3.4.1 Intrinsic Phosphorus Doping

Previous reports have described annealing Zn_3P_2 samples in P_4 to reversibly adjust the resistivity as a function of phosphorus pressure [27]. Red phosphorus and

Br_2-etched Zn_3P_2 wafers were loaded in a vacuum-sealed quartz ampoule, the red phosphorus was converted to white phosphorus at 550 °C and then entire ampoule was annealed at 400–450 °C for 20 h. The Hall effect measurements of Zn_3P_2 substrates doped intrinsically with phosphorus were consistent with previous reports, corresponding to acceptor concentrations of $\sim 10^{16}$ cm^{-3} and hole mobility in the range of 15–20 $cm^2 \cdot V^{-1} \cdot s^{-1}$ (data shown in table 3.1). There was some indication that p-type doping for intrinsically doped Zn_3P_2 changed over a period of several months to become more resistive, but the effect was not quantitatively evaluated.

3.4.2 Silver Doping

The p-type conductivity of Zn_3P_2 was increased by introducing silver dopants to the crystal. Two methods were explored for introducing Ag impurities: adding Ag to the growth of the Zn_3P_2 crystal, and metallizing a Zn_3P_2 wafer followed by solid-source diffusion.

Doping with Ag during the crystal growth resulted in a highly nonuniform distribution of doping properties within the crystal. In the absence of Ag doping the resistivity of Zn_3P_2 appeared to be rather uniform, but high in the 10^4–10^5 $\Omega \cdot cm$ range. With the addition of 10–30 mg of Ag shot to the growth ampoule, the resistivity of the majority of the crystal remained in the range typical of phosphorus-doped samples. However, the growth end of the crystal displayed significantly reduced resistivity. Further experiments to introduce Ag into the raw Zn_3P_2 powders rather than to the crystal growth may be an effective strategy for increasing the conductivity.

Metallization of Zn_3P_2 substrates with Ag followed by solid-source diffusion gave more uniform results and was the preferred method for controlling p-type doping. Hall effect measurements were conducted on Zn_3P_2 samples doped with Ag and in all cases p-type conductivity was observed (data shown in table 3.1). The electronic properties of Ag-doped Zn_3P_2 substrates annealed in white phosphorus were broadly consistent with previous reports and p-type doping in the high 10^{17} cm^{-3} with hole mobility of 17 ± 1 $cm^2 \cdot V^{-1} \cdot s^{-1}$ was achieved. Metallization with thicker Ag films did not appear to increase the Zn_3P_2 substrate acceptor concentration above the

Table 3.1. Results from Hall effect measurements of Zn_3P_2 substrates showing controlled p-type doping in the 10^{13}–10^{18} cm^{-3} range for intrinsic P and extrinsic Ag dopants introduced at 400 °C for 20 h

Dopant	Anneal Ambient	p (cm^{-3})	μ_p (cm^2 V^{-1} s^{-1})
none	none	10^{13} –10^{14}	16 ± 3
none	P_4	$3.7 \pm 0.4 \times 10^{16}$	12 ± 1
Ag (1.3 nm)	P_4	$3.0 \pm 0.1 \times 10^{17}$	14 ± 1
Ag (12 nm)	P_4	$7.6 \pm 0.8 \times 10^{17}$	17 ± 2
Ag (80 nm)	P_4	$7.5 \pm 0.4 \times 10^{17}$	17 ± 1

threshold of $\sim 10^{18}$ holes $\cdot$ cm^{-3}.

Hall effect measurements across the temperature range 80–300 K were also performed on phosphorus-doped and Ag-doped Zn_3P_2 substrates (figure 3.6). The Joule–Thompson effect is used to provide cooling power to the stage, whereby high pressure N_2(g) at 120–130 atm is allowed to escape through a small capillary and undego expansionary cooling. For the measurement the sample contacts were replaced thin manganin wires to minimize heat transfer to the cooling stage. For phosphorus-doped substrates, neither hole mobility nor hole density values were found to be strong functions of temperature. For Ag-doped samples, hole mobility values were not found to be a strong function of temperature but hole density values decreased by an order of magnitude in the 80–300 K temperature range.

3.4.3 Chalcogen Doping

A long-standing goal of work with Zn_3P_2 has been reliable and controllable n-type doping. Achieving Zn_3P_2 substrates or thin films with high electron density without reducing minority carrier lifetimes would allow for the fabrication of p-n homojunction devices based on Zn_3P_2. One report of Zn_3P_2 with a zinc excess of 10% to 15% reported n-type doping but only with electron density of 10^{13} cm^{-3}. By analogy with InP and other Group III–V semiconductors, the substitutional inpurity of a Group

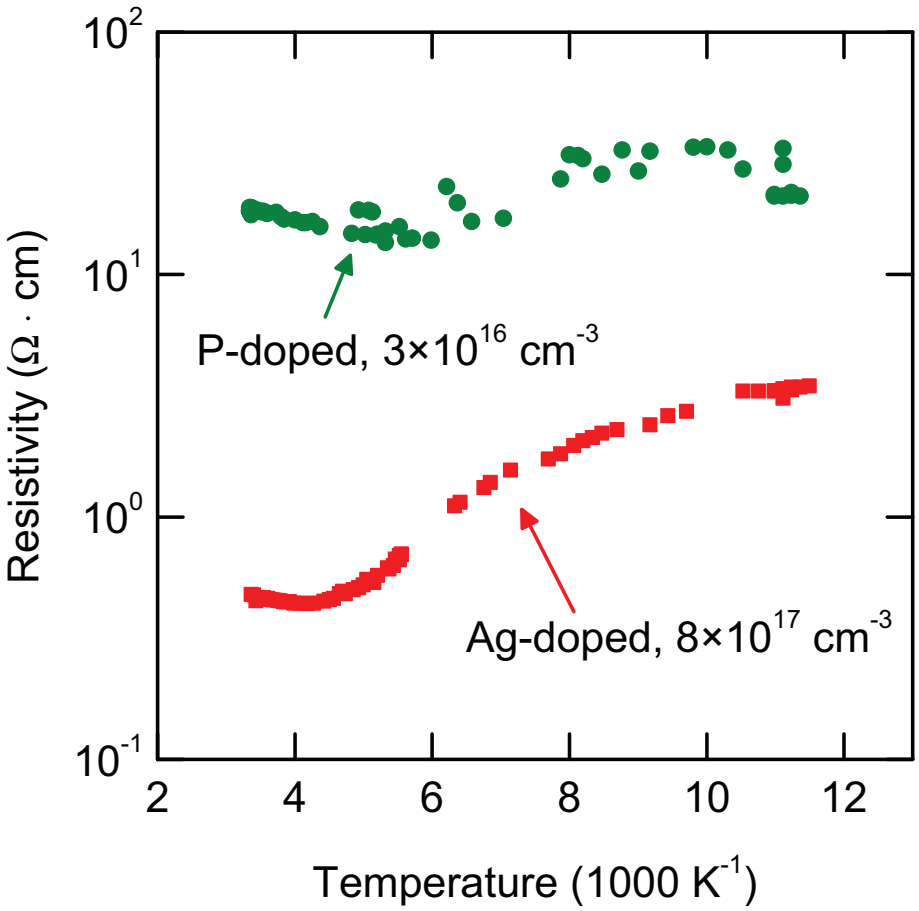

Figure 3.6. Resistivity of both P-doped (green) and Ag-doped (red) Zn_3P_2 substrates as a function of temperature in the range 80–300 K. Hall mobility was not found to be a strong function of temperature in this range.

VI chalcogen on a Group V lattice site could yield n-type doping behavior in Zn_3P_2.

Zn_3P_2 substrates were annealed in the presence of elemental sulfur at 350, 450, and 550 °C for 24 h, but secondary-ion mass spectrometry (SIMS) analysis did not indicate any dopant incorporation in the bulk of the substrate. Furthermore, at the highest temperature of 550 °C, the roughening of the wafer surface was too severe for device applications. Sections 5.2.1 and 5.3.2 contain more information about analysis of impurities by SIMS in Zn_3P_2 substrates and devices.

Due to the difficulty in introducing chalcogen to finished Zn_3P_2 substrates, elemental chalcogen and zinc chalcogenide were introduced as dopant material to the crystal growth of Zn_3P_2. Zinc chalcogenides including ZnS, ZnSe, and ZnTe were added to the Zn_3P_2 powders of the crystal growth ampoule, but did not completely incorporate during the 850 °C physical vapor transport process. Starting and final masses were equal within error, suggesting that zinc chalcogenides did not incorporate well during the crystal growth. Adding elemental chalcogen to the crystal growth was also attempted, but zinc chalcogenide was observed to form and accounted for most of the weight of the additional chalcogen.

Finally the elemental chalcogen was added to the ampoule with an increased sublimation temperature of 1100 °C. In the higher temperature the selenium and telerium material appeared to be incorporated in the Zn_3P_2 crystal. Analysis by ICPMS confirmed increased levels of Se and Te. Zn_3P_2 samples with introduced chalcogen displayed lower hole mobility values than control samples, but hole density values were of the same order. Chalcogen incorporation into Zn_3P_2 substrates did not yield n-type material for any of the conditions explored.

3.5 Conclusions

The Zn_3P_2 substrates prepared as described in chapter 2 demonstrated optoelectronic properties nearly ideal for application in photovoltaics. The high purity of the Zn_3P_2 substrates allowed the first measurements of room temperature photoluminescence from Zn_3P_2 and the determination of the nature of the fundamental band gap. Spec-

Table 3.2. Results from Hall effect measurements and ICPMS impurity concentrations for chalcogen impurities in Zn_3P_2 introduced at 850 and 1100 °C

Dopant	°C	p (cm^{-3})	μ_p ($cm^2 \cdot V^{-1} \cdot s^{-1}$)	Se ratio	Te ratio
control	850	$3.0 \pm 0.7 \times 10^{16}$	15 ± 2	1.0	1.0
ZnS	850	$2.2 \pm 0.8 \times 10^{16}$	13 ± 2	n/a	n/a
ZnSe	850	$3.1 \pm 1.5 \times 10^{15}$	11 ± 2	44.6	1.35
control	1100	$6 \pm 3 \times 10^{15}$	15 ± 4	1.0	1.0
Se	1100	$3 \pm 2 \times 10^{15}$	13 ± 1	36.2	1.8
Te	1100	$8 \pm 5 \times 10^{15}$	12 ± 6	2.8	5.8

troscopic ellipsometry measurements were consistent with the band gap assignment derived from photoluminescence and provided an n(ω), k(ω) model for Zn_3P_2 across the visible and near infrared spectral range. Long minority carrier lifetimes of 20 ns corresponded to minority carrier diffusion lengths of $\geq 7\mu m$ as measured by time-resolved photoluminescence. Control of p-type doping control from 10^{13} to 10^{18} cm^{-3} hole densities was observed by combined intrinsic phosphorus and extrinsic silver dopants. Chalcogen doping in an attempt to acheive n-type doping by chalcogens did not greatly affect the native p-type doping of the Zn_3P_2 substrates. The bulk optoelectronic properties of Zn_3P_2 substrates prepared by PVT from elemental Zn and P appear to be nearly ideal for application in solar energy conversion devices.

Chapter 4

Composition and Electronic Properties of Zn_3P_2 Interfaces

Control of the chemical composition and electronic defect density of Zn_3P_2 surfaces is a critical prerequisite for demonstrating high efficiency devices for solar energy conversion. The formation of stoichiometric Zn_3P_2 surfaces nearly free of overlayers was accomplished by two-step etching with 2% Br_2 in methanol followed by treatment with HF:H_2O_2 (aq). The chemical composition and surface recombination velocity were investigated by x-ray and UV photoelectron spectroscopy, steady-state and time-resolved photoluminescence, as well as metal/insulator/semiconductor capacitance analysis. Chemically treated Zn_3P_2 surfaces with 1–2 monolayers (ML) coverage of elemental phosphorus (P^0) exhibited slower surface recombination rates than those with ≈4 ML P^0 coverage. The oxidation of chemically treated Zn_3P_2 surfaces in air resulted in even further reduced surface recombination velocity to values below 2×10^3 cm $\cdot$ s^{-1}. The relationship between chemical composition and surface recombination reported here provides a foundation for further surface passivation and device integration of Zn_3P_2.

4.1 Introduction

Zn_3P_2 is a promising candidate for solar energy conversion devices due to its direct band gap at 1.5 eV, long (5–10 μm) minority carrier diffusion lengths and controllable p-type doping (10^{13}–10^{18} cm^{-3}). However, the difficulty in preparing n-type Zn_3P_2 has prevented the formation of *p-n* homojunctions and has led to a focus

on Schottky contacts [41] and *p*-*n* heterojunctions. Although p-Zn_3P_2/Mg diodes have achieved 6% solar energy conversion efficiency [2], solar cells based on Zn_3P_2 *p*-*n* heterojunctions have so far been fabricated with solar energy conversion efficiencies $\leq$2% [15, 42, 43, 44]. The open-circuit voltages and barrier heights of Zn_3P_2 *p*-*n* heterojunction solar cells have been limited by Fermi-level pinning due to high concentrations of interface states as well as interfacial chemical reactions [14]. Therefore, the development of improved etching and passivation treatments for Zn_3P_2 is necessary to produce interfaces that are chemically inert and electrically passive.

Etching with 2% Br_2 in methanol has been used almost exclusively to prepare Zn_3P_2 substrates for incorporation into devices, but only a few qualitative accounts of the resulting surface have been reported [45, 46, 47]. Comparing novel treatments to the 2% Br_2 in methanol etch requires a quantitative analysis of the chemical composition and electronic properties for surfaces prepared by each method. Some authors have used capacitance measurements to estimate surface state densities of $>10^{13}$ cm^{-2} at solid-state Zn_3P_2 junctions [14, 44], but the surface states generated by wet chemical etching or solid-state interface reactions could not be distinguished. Characterizing the recombination rates of freshly prepared surfaces is a critical step toward achieving high quality interfaces and high efficiency devices with Zn_3P_2.

In this chapter, we describe an improved wet chemical surface preparation for Zn_3P_2 and investigate the passivating properties of native oxides on Zn_3P_2. Surface science techniques including x-ray photoelectron spectroscopy (XPS) and ultraviolet photoelectron spectroscopy (UPS) were used to determine the surface composition of chemically treated Zn_3P_2. Steady-state and time-resolved photoluminescence (PL) measurements were then employed to elucidate the effect of chemical treatment on surface recombination rates. Capacitance measurements of metal/insulator/semiconductor (MIS) structures incorporating Zn_3P_2 yielded surface trap densities that were consistent with the surface recombination rates deduced from time-resolved PL. We report here chemical methods for the control of Zn_3P_2 surface properties and illustrate how changes in surface composition affect the energetic and electronic properties of Zn_3P_2 interfaces.

4.2 Surface Composition

Ultra high vacuum surface science techniques such as XPS allow for quantitative analysis of the atomic composition first 1–10 nm of a semiconductor surface. The high selectively for surface composition in XPS arises because the core electrons ejected by the incident x-rays typically have only a 1–3 nm average escape depth from the sample. Analyzing the ejected photoelectrons within a narrow energy range yields information about the concentration and chemical bonding for specific elements at the surface.

4.2.1 X-ray Photoelectron Spectroscopy

The surface chemical species of Zn_3P_2 substrates with different chemical treatments were monitored by XPS using a Kratos surface science instrument. Typical base pressures of 5×10^{-10} Torr were used during the measurements. Monochromated x-rays of 1486.7 eV from an Al K-α source were used to eject photoelectrons from Zn_3P_2 samples. The detection line width of the system was 0.35 eV under the analysis conditions, and emitted photoelectrons were typically collected with the detector 0° from the surface normal [48]. High resolution XPS of the Zn $2p_{3/2}$ and P $2p$ regions were processed using linear baseline subtraction and standard peak fitting routines to obtain binding energies and integrated areas. High resolution XPS signals were fit in the Zn $2p_{3/2}$ region using 9:1 Gaussian–Lorentzian product functions and in the P $2p$ region using pure Lorentzian functions. The P $2p$ signal was fit by three doublets attributed to bulk Zn_3P_2, elemental phosphorus, and oxidized phosphorus, where each set of doublets was constrained to have an area ratio of 2:1 and a doublet separation of 0.83 eV. The Zn $2p_{3/2}$ signal was fit by a pair of line shapes corresponding to bulk Zn_3P_2 and oxidized zinc. The energy scale was corrected to the bulk Zn_3P_2 P $2p$ signal averaged over 8 samples as 127.9 ± 0.05 eV.

The overlayer coverages compiled in table 4.2 were calculated from integrated XPS signal intensity by

$$d_a = \lambda_a \cos\theta \cdot \ln\left(\frac{I_a \sigma_b \lambda_b}{I_b \sigma_a \lambda_a} + 1\right) \quad , \tag{4.1}$$

where d_a is the overlayer thickness in nanometers, λ_x is the escape depth of the photoelectron in nanometers, I_x is the integrated peak counts, θ is the angle between the surface normal and the detector, σ_x is the tabulated relative sensitivity factor, "a" designates the overlayer, and "b" designates the substrate [49]. Escape depths were computed using the method of Seah and Dench and relative sensitivity factors were estimated from tabulated standard values [49]. The thickness of overlayer coverage was converted to monolayer units using the estimated atomic volume of the overlayer species.

Figure 4.1 shows representative XPS survey scans of both polished and chemically treated Zn_3P_2 substrates. Photoelectrons corresponding to zinc and phosphorus core transitions were the predominant features, without any contamination by bromine or fluorine from the etching chemistry. The high compositional purity of the surface of samples is consistent with analysis by inductively-coupled mass spectrometry that showed >99.999% bulk purity in the Zn_3P_2 substrates. Carbon and oxygen contamination were observed to be submonolayer for freshly etched samples, but samples exposed to air for several days showed 3–7 ML of adventitious carbon and native oxidation.

Further analysis of the zinc and phosphorus surface species was conducted using high resolution XPS analysis of the Zn $2p_{3/2}$ and P $2p$ regions. Figure 4.2 shows the representative high resolution XP spectra of polished Zn_3P_2 substrates before and after chemical treatment and table 4.2 shows the coverages of P^0, adventitious carbon and native oxides estimated from the XP spectra. Polished substrates were found to be zinc-rich in the bulk substrate and almost pure zinc oxide in the oxidized overlayer. After etching in 2% Br_2 in methanol for 30 s, the substrates were free of zinc and phosphorus surface oxidation and displayed decreased contamination by oxygen and carbon. Although the bulk, stoichiometric Zn_3P_2 substrate was clearly observed, significant residual elemental phosphorus (P^0) remained after etching in 2% Br_2 in

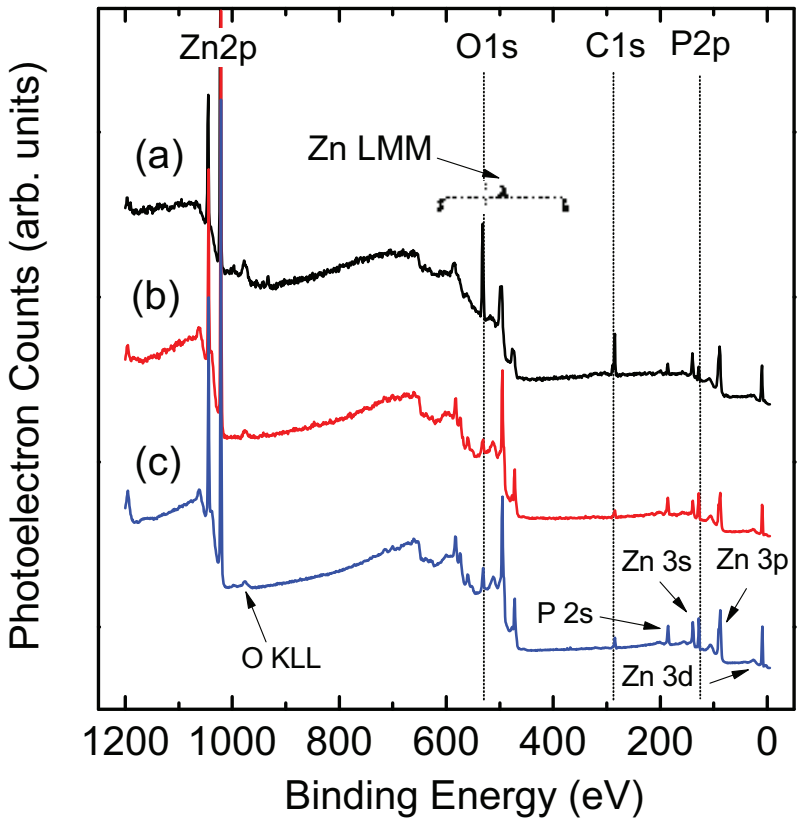

Figure 4.1. XPS survey scans of Zn_3P_2 substrates (a) polished, (b) etched in 2% Br_2 in methanol for 30 s, and (c) etched in 2% Br_2 in methanol for 30 s and then treated with 10% HF–0.25% H_2O_2 (aq) for 60 s.

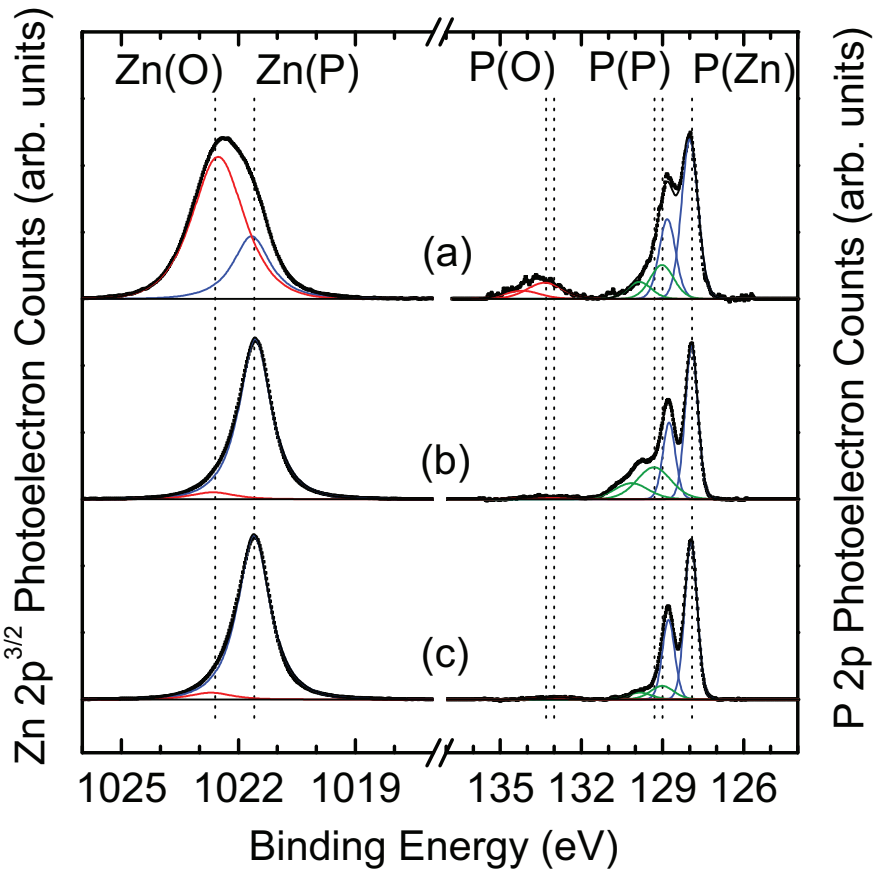

Figure 4.2. XP spectra of the Zn $2p_{3/2}$ and P $2p$ regions for Zn_3P_2 substrates (a) polished, (b) etched in 2% Br_2 in methanol for 30 s, and (c) etched in 2% Br_2 in methanol for 30 s and then treated with 10% HF–0.25% H_2O_2 (aq) for 60 s.

methanol that was resistant to rinsing and sonication treatments. Treatment of Zn_3P_2 substrates that had been etched in 2% Br_2 in methanol with 10% HF–0.25% H_2O_2 (aq) was effective at selectively removing the majority of the residual P^0 surface layer. The high resolution XP spectra showed the reduction of the P^0 to 1–2 ML coverage without significant oxidation of zinc or phosphorus or alteration of the substrate stoichiometry.

Figure 4.3 shows high resolution XPS analysis of etched Zn_3P_2 substrates that had been exposed to air for one week. The substrates exhibited oxidized species of both zinc and phosphorus while retaining bulk, stoichiometric Zn_3P_2 substrates. The residual P^0 did not appear to oxidize during air exposure, but affected the sto-

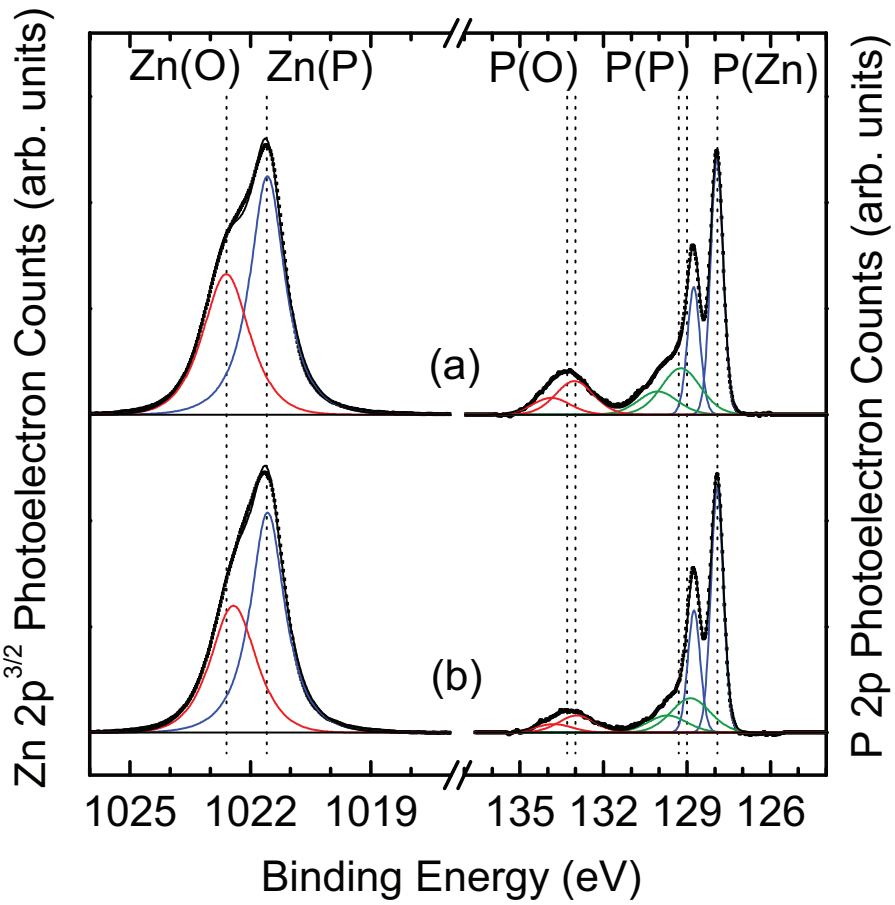

Figure 4.3. XP spectra of the Zn $2p_{3/2}$ and P $2p$ regions for Zn_3P_2 substrates that were (a) etched in 2% Br_2 in methanol for 30 s and exposed to air for one week and (b) etched in 2% Br_2 in methanol for 30 s, treated with 10% HF–0.25% H_2O_2 (aq) for 60 s, and exposed to air for one week.

ichiometry of the native oxide that formed. Samples with thicker residual P^0 grew stoichiometric oxides, while samples with limited P^0 grew oxides slightly depleted in phosphorus. In both cases, however, the native oxide layer contained at least 25% phosphorus by metals basis. The binding energies of the oxidized phosphorus and oxidized zinc signals were consistent with the presence of a $Zn_x(PO_3)_y$ species rather than a fully oxidized PO_4 species [50].

Table 4.1 shows the binding energies observed for surface zinc and phosphorus species with different chemical bonding environments. For bulk Zn_3P_2, the

Table 4.1. XPS binding energies for Zn $2p_{3/2}$ and P $2p$ species including bulk Zn_3P_2, residual elemental phosphorus, and native oxidation

core level	species	binding energy (eV)	Gaussian width (eV)
Zn $2p_{3/2}$	Zn_3P_2	1021.6 ± 0.05	0.96 ± 0.02
Zn $2p_{3/2}$	ZnO_x	1022.6 ± 0.05	1.4 ± 0.1
P $2p_{3/2}$	Zn_3P_2	127.9 ± 0.05	0.54 ± 0.02
P $2p_{3/2}$	P^0	129.0 ± 0.1	1.0 ± 0.1
P $2p_{3/2}$	P^0	129.3 ± 0.1	1.5 ± 0.2
P $2p_{3/2}$	PO_x	133 ± 0.3	1.5 ± 0.1

binding energy of Zn $2p_{3/2}$ is 1021.6 ± 0.05 eV and the binding energy of P $2p$ is 127.9 ± 0.05 eV. Oxidized zinc and phosphorus species exhibit binding energies for the Zn $2p_{3/2}$ of 1022.6 ± 0.05 eV and for the P $2p$ of 133.1 ± 0.3 eV. The additional signal attributed to ≈4 ML P^0 overlayers has a binding energy of 129.3 eV while that attributed to 1–2 ML P^0 overlayers has a binding energy of 129.0 eV.

4.2.2 Ultraviolet Photoelectron Spectroscopy

Spectra of the valence band region of chemically treated Zn_3P_2 samples were recorded using He (I) radiation with $h\nu = 21.2$ (figure 4.4). Valence band spectra were collected with the analysis chamber at 10^{-8} Torr and Cu, Au and Si standards were evaluated to calibrate the energy scale. Freshly prepared samples were measured immediately after introduction to the vacuum chamber, and Ar-ion sputtered samples were measured without annealing after light sputtering with 2 keV energy ions. The linear intersection of the low binding energy baseline and the rising valence band was used to determine the valence band edge; the linear intersection of the high binding energy baseline and the secondary electron cutoff was used to determine the work function. The zero binding energy point for each spectrum was corrected to the expected separation between the Fermi energy and the valence band edge as computed from the bulk doping concentration in the substrate [40].

Table 4.2. Overlayer coverage of elemental phosphorus (P^0), adventitious carbon, and native oxidation as derived from XPS analysis of chemically treated Zn_3P_2 substrates

sample	P^0 (ML)	C (ML)	ZnO_x (ML)
polished	3.5 ± 1	≥6	≥10
(i)	4.1 ± 0.5	0.9 ± 0.2	0.4 ± 0.2
(ii)	1.4 ± 0.2	0.7 ± 0.2	0.3 ± 0.2
(i), 1 week air	4 ± 1	4 ± 2	4 ± 2
(ii), 1 week air	3 ± 1	4 ± 2	4 ± 2

(i) = 2% Br_2 in methanol for 30 s.

(ii) = (i) + 10% HF–0.25% H_2O_2 (aq) for 60 s.

"-" indicates that the peaks were of too low intensity to assign.

The Zn_3P_2 samples showed the characteristic valence band emission feature at 10 eV that corresponded to Zn 3*d* photoelectrons. For Zn_3P_2 substrates freshly etched in 2% Br_2 in methanol, the feature exhibited low intensity, but brief sputtering treatment was sufficient to clearly resolve the Zn 3*d* peak. The electron affinity, χ, of the measured Zn_3P_2 samples was calculated by

$$\chi = W_F - (E_g - |E_v - E_F|) \quad , \tag{4.2}$$

where W_F is computed from the difference between the photon energy and secondary electron cutoff, E_g = 1.38 eV, and $|E_v - E_F| = 0.30 \pm 0.05$ eV is estimated from the known doping concentration. In agreement with previous valence band analysis [45], the electron affinity of Zn_3P_2 was found to be 3.2 ± 0.1 for chemically etched Zn_3P_2 samples and 3.6 ± 0.1 for lightly sputtered samples. No significant change was observed in the Zn $2p_{3/2}$ binding energy before and after sputtering, implying that the surface remained under similar band-bending conditions. Therefore, the discrepancy between the apparent values of electron affinity for the chemically etched and sputtered surfaces was ascribed to the low electron affinity of P^0 and/or adventitious

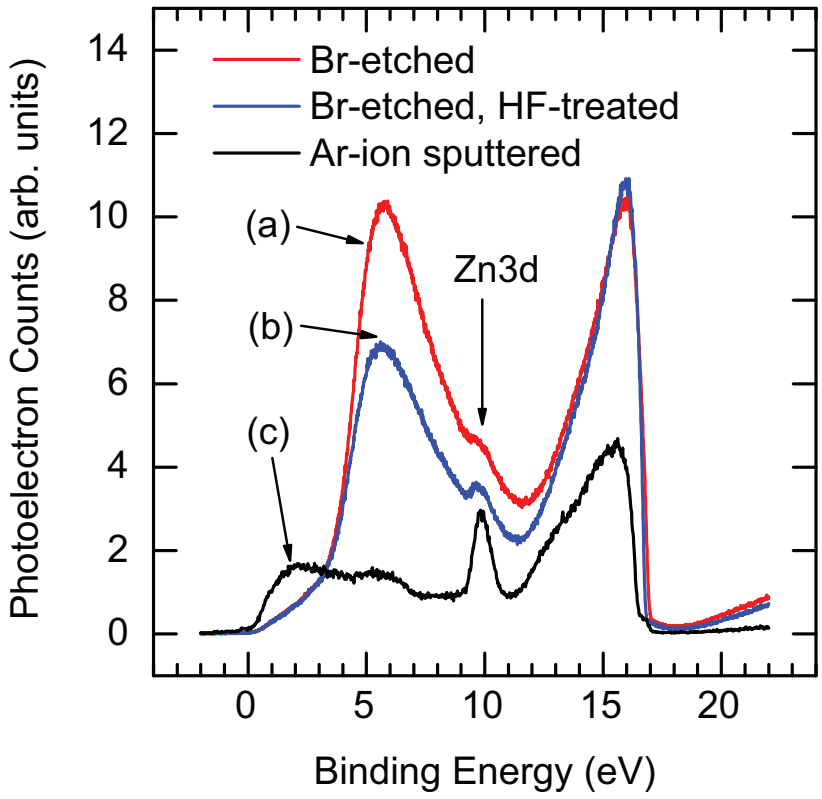

Figure 4.4. Valence band spectra excited with He (I) radiation $h\nu = 21.2$ eV of Zn_3P_2 substrates that were (a) etched in 2% Br_2 in methanol for 30 s, (b) etched in 2% Br_2 in methanol for 30 s and then treated with 10% HF–0.25% H_2O_2 (aq) for 60 s, and (c) etched in 2% Br_2 in methanol for 30 s and briefly sputtered with Ar ions at 2 keV.

carbon chemical overlayers.

4.3 Electronic Effect of Chemical Treatments

The effect of chemical treatment on the surface recombination rates of Zn_3P_2 substrates was investigated by steady-state and time-resolved room temperature PL measurements. A higher density of surface defects increases the proportion of electron-hole pairs that recombine nonradiatively relative to those that recombine radiatively. Therefore, a lower density of surface defects is expected to correlate with increased

intensity of steady-state PL. Although steady-state PL intensity provides a qualitative measure of surface quality, time-resolved PL decay measurements allow for quantitative analysis of both surface and bulk recombination rates. The trends in surface quality observed by PL measurements were confirmed by impedence analysis using metal/insulator/semiconductor devices fabricated with chemically treated Zn_3P_2 substrates.

4.3.1 Steady-State Photoluminescence

For steady-state PL measurements, excitation was performed using the 488 nm line of an Ar-ion laser that was chopped at 10 kHz using an acousto-optic modulator. The emission was passed through a monochromator and focused onto an infrared photomultiplier tube, and the PL signal was monitored using a lock-in amplifier. Steady-state PL was collected at room temperature in air using a laser power of <10 mW $\cdot$ cm^{-2}, under low-level injection, because at larger laser powers laser degradation was observed in air.

Figure 4.5 shows the steady-state PL spectra collected from freshly prepared Zn_3P_2 substrates in air, under low-level injection. Polished samples did not exhibit room temperature PL even at laser powers $>100\times$ those required to measure chemically treated samples. Chemical etching by 2% Br_2 in methanol was effective at removing the zinc-rich surface layer and subsurface mechanical damage from the polished samples, allowing room temperature PL to be readily observed. Further treatment with 10% HF–0.25% H_2O_2 (aq) increased steady-state PL intensity by a factor of at least 2.3 ± 0.2. Error bars were produced using the measured PL intensities of at least five positions on each sample.

Figure 4.6 shows the steady-state PL characteristics of chemically treated Zn_3P_2 substrates that had been exposed to air for one week. After one week exposure to air, chemically treated Zn_3P_2 substrates exhibited a steady-state PL intensity greater than that observed for substrates freshly etched in 2% Br_2 in methanol, but less than that observed for substrates etched in 2% Br_2 in methanol and then treated with 10% HF–0.25% H_2O_2 (aq). Under low-level injection, changes in both surface recombination

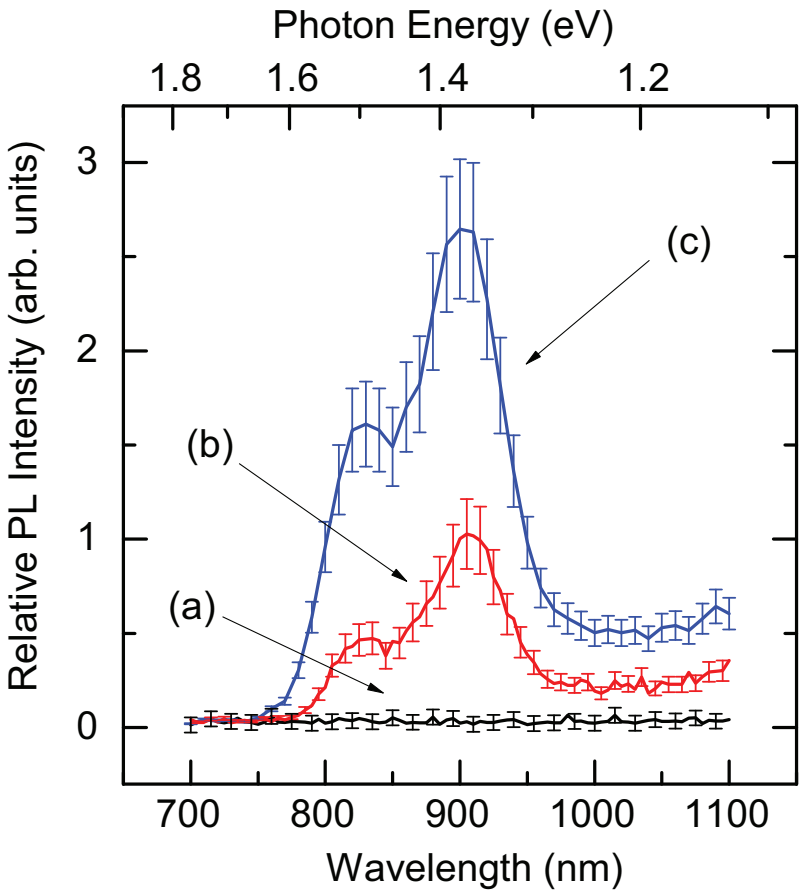

Figure 4.5. Steady-state photoluminescence spectra under ambient conditions for Zn_3P_2 substrates (a) polished, (b) etched in 2% Br_2 in methanol for 30 s and (c) etched in 2% Br_2 in methanol for 30 s and then treated with 10% HF–0.25% H_2O_2 (aq) for 60 s. The excitation source was an Ar-ion laser operating at 488 nm.

rates and surface band-bending affect the observed PL intensity [51, 52], limiting steady-state PL intensity measurement as a qualitative metric.

4.3.2 Time-Resolved Photoluminescence

To quantitatively compare the surface recombination rates of Zn_3P_2 substrates with different chemical composition, time-resolved PL studies were conducted under high-level injection conditions. The high intensity of the laser pulses used for time-resolved PL is sufficient to reach the flat band condition and suppresses the effects of surface band-bending in the semiconductor [53]. Under high-level injection, the PL decay dynamics immediately after the laser pulse are dominated by the effects of surface recombination, and allow quantitative estimates of surface recombination velocity (SRV) values to be extracted.

Time-resolved PL measurements were performed at 10 kHz with 70 ps, 355 nm pulses produced by frequency tripling of regeneratively amplified, mode-locked Nd:-YAG laser pulses. Pulse powers ranging from 100 $nJ \cdot pulse^{-1}$ to 10 $\mu J \cdot pulse^{-1}$ were used in the study, but no significant differences in the decay dynamics as a function of pulse energy were observed. The emission was collected using a fiber optic and the signal was integrated using a streak camera. Time-resolved PL measurements were performed under Ar(g) atmosphere using a custom sample holder built by Jeffery Lefler. PL decay traces were not affected by the position on a sample, the collection time, or whether samples were spinning or stationary.

Analysis of the time-resolved PL data was performed using simulated PL decay traces generated by numerically solving the continuity equations under the assumption of high-level injection and with transport dominated by ambipolar diffusion (see appendix B) [53, 54]. In our simulation, photogenerated carriers were introduced into the substrate with an exponential depth profile based on the absorption coefficient and a Gaussian time profile based on a pulse width of 130 ps. The carriers were allowed to diffuse and recombine nonradiatively at the surface and in the bulk of the sample, with the spatially and temporally resolved *np* product determining the simulated PL intensity as a function of time. With fixed assumptions for bulk nonradiative

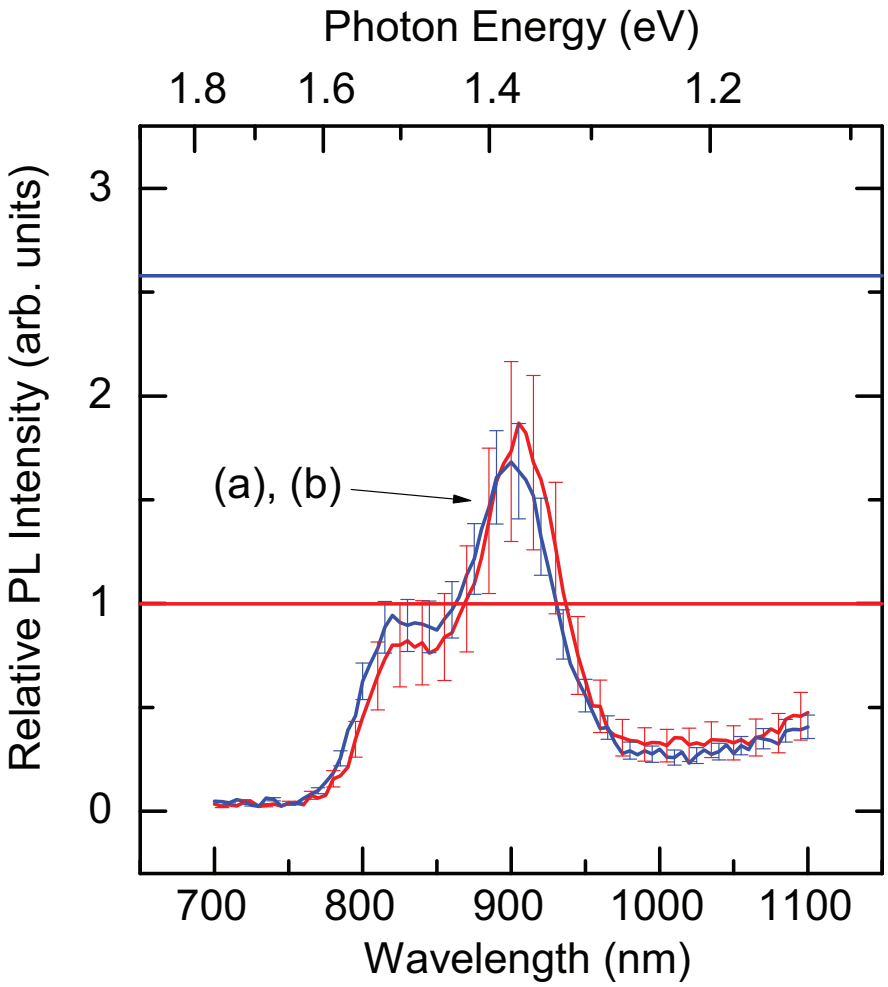

Figure 4.6. Steady-state photoluminescence spectra under ambient conditions for Zn_3P_2 substrates (a) etched in 2% Br_2 in methanol for 30 s and exposed to air for one week and (b) etched in 2% Br_2 in methanol for 30 s, treated with 10% HF–0.25% H_2O_2 (aq) for 60 s, and exposed to air for one week. The horizontal lines denote steady-state PL intensity observed for freshly etched substrates (figure 4.5).

lifetime of 20 ns and ambipolar diffusion coefficient of 1 $cm^2 \cdot s^{-1}$, the only adjustable parameter was the surface recombination velocity (SRV), which was varied from 10^3 to 10^7 $cm \cdot s^{-1}$ in the simulation [36, 40].

Representative time-resolved PL data for Zn_3P_2 substrates with different chemical treatments are shown in figure 4.7. Zn_3P_2 substrates that were etched with 2% Br_2 in methanol showed the most rapid PL decays in the measured samples with SRV of $2.8 \pm 0.1 \times 10^4$ $cm \cdot s^{-1}$. Zn_3P_2 substrates that were etched with 2% Br_2 in methanol and then treated by 10% HF–0.25% H_2O_2 (aq) showed significantly reduced SRV of $1.0 \pm 0.1 \times 10^4$ $cm \cdot s^{-1}$. Zn_3P_2 substrates that were etched with 2% Br_2 in methanol and then exposed to air for one week showed much longer PL decays than samples tested immediately after etching, with SRV values of $1.8 \pm 0.1 \times 10^3$ $cm \cdot s^{-1}$.

Table 4.3 displays the steady-state PL intensities and SRV values for a series of chemically treated Zn_3P_2 substrates. Surface defect densities were calculated using the relationship $S = N_t \cdot \sigma \cdot v_{th}$ [40], where S is the SRV in units of $cm \cdot s^{-1}$, N_t is the area density of surface traps in units of cm^{-2}, σ is the cross section for carrier capture (estimated as 10^{-16} cm^2 for typical surface traps of InP) [55], and v_{th} is the thermal velocity of carriers (estimated as 10^7 $cm \cdot s^{-1}$). Assuming defects with similar capture cross sections, Zn_3P_2 substrates that were etched with 2% Br_2 in methanol and then treated by 10% HF–0.25% H_2O_2 (aq) exhibited a threefold reduction in the active surface recombination sites relative to Zn_3P_2 substrates that had only been etched with 2% Br_2 in methanol. By the same metric, the formation of native oxides on Zn_3P_2 substrates that were etched with 2% Br_2 in methanol corresponded to the passivation of greater than 90% of the active surface recombination sites.

4.3.3 Impedance Analysis of MIS Devices

Capacitance measurements of $Hg/Al_2O_3/Zn_3P_2$ metal/insulator/semiconductor (MIS) devices were used to estimate the surface trap density values for chemically treated Zn_3P_2 substrates. Zn_3P_2 substrates that had been freshly etched with 2% Br_2 in methanol were compared to those that had been exposed to air for one week. After preparation of the Zn_3P_2 substrates, insulating layers of Al_2O_3 of ≈60 nm thickness

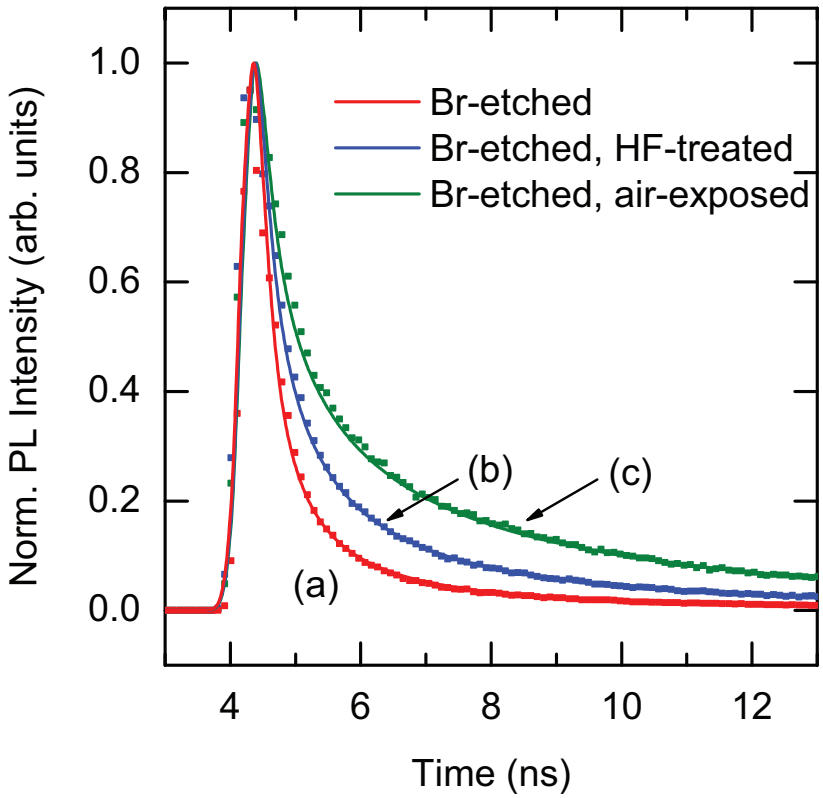

Figure 4.7. Time-resolved photoluminescence decay traces collected under Ar at 295 K from Zn_3P_2 substrates that were (a) etched in 2% Br_2 in methanol for 30 s, (b) etched in 2% Br_2 in methanol for 30 s and then treated with 10% HF–0.25% H_2O_2 (aq) for 60 s, and (c) etched in 2% Br_2 in methanol for 30 s and exposed to air for one week.

Table 4.3. Results of photoluminescence-based characterization of chemically treated Zn_3P_2 where relative photoluminescence intensity was recorded at 890 nm, and time-resolved photoluminescence decays were used to determine surface recombination velocity (SRV) and surface trap density (N_t)

sample	relative PL signal (arb. units)	SRV ($cm \cdot s^{-1}$)	N_t (cm^{-2})
polished	<0.02	-	-
(i)	1.0 ± 0.2	$2.8 \pm 0.1 \times 10^4$	3×10^{13}
(ii)	2.3 ± 0.2	$1.0 \pm 0.1 \times 10^4$	1×10^{13}
(i), 1 week air	1.7 ± 0.2	$1.8 \pm 0.1 \times 10^3$	2×10^{12}

(i) = 2% Br_2 in methanol for 30 s.

(ii) = (i) + 10% HF–0.25% H_2O_2 (aq) for 60 s.

"-" indicates that the peaks were of too low intensity to assign.

were deposited by electron-beam evaporation. Hg drop electrodes with contact area of ∼1 mm^2 were used as the metal gate electrode in the MIS devices due to its ease of application and insensitivity to pinholes. Using a Princeton Applied Research (PAR 2273) potentiostat with electrochemical impedance spectroscopy module, the MIS devices were swept from accumulation to depletion at 80 $mV \cdot s^{-1}$, and capacitance was monitored at 10 kHz with a 10 mV alternating potential. Bode plots of the devices showed a 85° to 90° phase angle in the complex impedance for the −2 to +4 V gate biases used for analysis of the capacitance data.

Surface state density distributions were estimated using the high-frequency capacitance method first developed by Terman [40, 56]. Using values of $\epsilon_{Al_2O_3} = 4.5$, $\epsilon_{Zn_3P_2} = 11$, and dopant density of 10^{15} cm^{-3} [57], the measured capacitance was used to compute the capacitance of the depletion width and the surface potential as functions of gate bias. The relationship of surface potential to gate bias was related to surface state density by

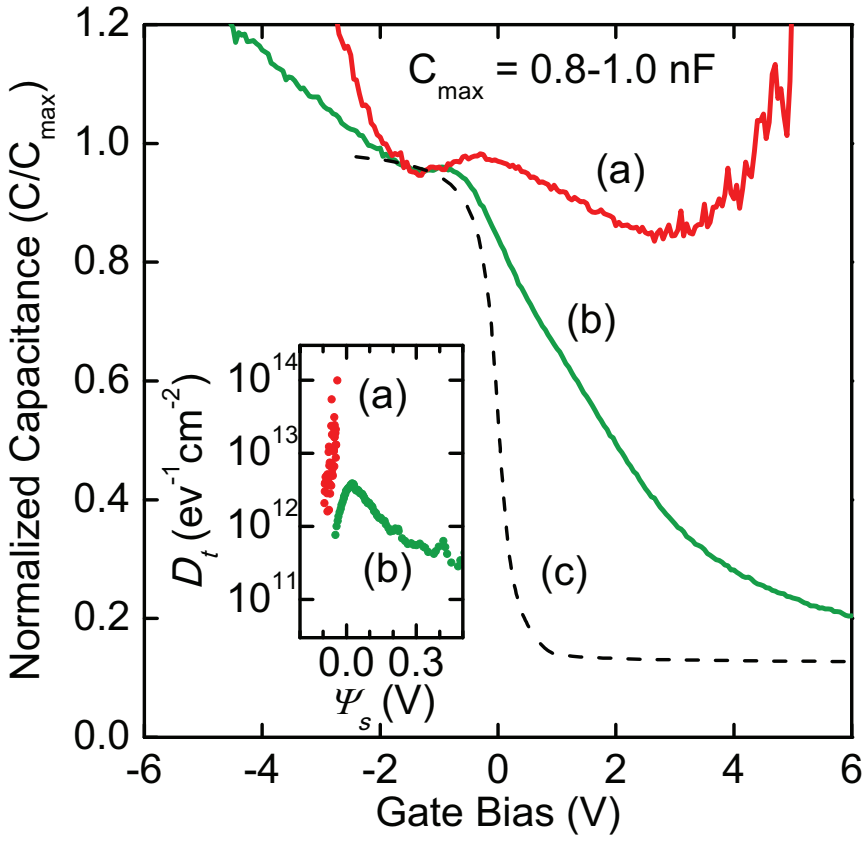

Figure 4.8. High-frequency (10 kHz) capacitance as a function of gate bias for $Hg/Al_2O_3/Zn_3P_2$ devices where the substrate was (a) etched in 2% Br_2 in methanol for 30 s, or (b) etched in 2% Br_2 in methanol for 30 s and exposed to air for one week. Trace (c) shows the expected capacitance for ideal $Hg/Al_2O_3/Zn_3P_2$ devices in the absence of surface trap states. The inset shows the estimated surface trap density distribution D_t as a function of surface potential Ψ_s.

$$D_t = \frac{C_i}{q}\left[\left(\frac{d\Psi_s}{dV}\right)^{-1} - 1\right] - \frac{C_D}{q^2} \quad , \tag{4.3}$$

where D_t is the surface trap density distribution in $eV^{-1} \cdot cm^{-2}$, C_i is the capacitance of the Al_2O_3 layer in farads, q is the charge of an electron in coulombs, Ψ_s is the surface potential in volts, V is the gate bias in volts and C_D is the capacitance of the depletion width in farads [56].

Figure 4.8 shows normalized capacitance data collected from $Hg/Al_2O_3/Zn_3P_2$ MIS devices compared to the expected ideal performance in the absence of surface trap states. Ideal MIS devices with p-type semiconductors show decreased capacitance with increasing positive gate bias as the semiconductor depletion width increases. MIS devices incorporating Zn_3P_2 substrates that had been freshly etched in 2% Br_2 in methanol, however, show only small modulation of capacitance with gate bias that is consistent with a high density of surface traps. The capacitance data from Br-etched Zn_3P_2 substrates with native oxides shows significant depletion of the semiconductor with positive gate bias and allows for an estimate of the surface trap density distribution (figure 4.8 inset). Freshly Br-etched surfaces are estimated to have surface trap density distributions that are $>10^{13}$ $eV^{-1} \cdot cm^{-2}$ but ethced surfaces that had been exposed to air are estimated to have values that are $\sim 10^{12}$ $eV^{-1} \cdot cm^{-2}$.

4.4 Conclusions

4.4.1 Electronic Quality of Chemically Etched Zn_3P_2

One striking feature of etched Zn_3P_2 surfaces is the large and persistent coverage of P^0 overlayers. Although phosphorus species with similar binding energy have been observed on etched InP surfaces, the amount of P^0 is typically submonolayer [58]. With respect to elemental group V overlayers, GaAs provides a closer analogy to Zn_3P_2 where As^0 is often found in several monolayer coverage [59, 60]. Etching of Zn_3P_2 by Br_2 in methanol is proposed to proceed by the following reaction [61, 62]:

$$Zn_3P_2 + 6\ Br_2 + 6\ CH_3OH \longrightarrow$$
$$3\ ZnBr_2 + 2\ (CH_3O)_2PHO + 2\ CH_3Br + 4\ HBr.$$

Etching with Br_2 concentrations from 0.05% to 3% in methanol was found to yield similar ≈4 ML coverage of P^0. Reaction of Br_2 with Zn (–185 kJ·(mol Br)$^{-1}$) yields a higher free energy than reacting with Ga (-146 kJ·(mol Br)$^{-1}$) or In (–160 kJ·(mol Br)$^{-1}$) [63]. As a result, there is a thermodynamic driving force for Br_2 in methanol to deplete the Zn_3P_2 surface of Zn and leave residual elemental phosphorus.

The results presented in this work show a correlation between the coverage of P^0 overlayers and the rate of surface recombination on Zn_3P_2. Some authors have proposed an analogous correlation for As^0 on GaAs [64], but the relationship between the electronically active recombination sites and As^0 coverage is by no means direct [18, 65]. Active surface recombination centers based on phosphorus antisite defects are consistent with the observed correlation of excess phosphorus with increased recombination rates on Zn_3P_2.

The estimated surface trap density values in table 4.3 support the hypothesis that a major factor limiting devices based on Zn_3P_2 is the high defect density of Zn_3P_2 substrates freshly etched with 2% Br_2 in methanol. Surface trap density values of $>10^{13}$ cm^{-2} have been measured for both $Al/Al_2O_3/Zn_3P_2$ metal/insulator/semiconductor devices and Zn_3P_2/ZnO *p*-*n* heterojunctions, in agreement with the surface trap density values computed in this work for freshly etched Zn_3P_2 substrates. Although solid-state reactions at the Zn_3P_2 junction could serve to further increase the surface trap density, the electronic defects of Zn_3P_2 substrates freshly etched in 2% Br_2 in methanol may be sufficient to account for the observed Fermi-level pinning. Further work to achieve lower P^0 overlayer coverage for chemically treated Zn_3P_2 substrates appears to be a promising route to reduced surface trap density and improved devices performance.

4.4.2 Composition and Passivity of Surface Oxidation

The measurement of SRV values below 2×10^3 cm $\cdot$ s^{-1} and improved MIS performance on oxidized Zn_3P_2 surfaces highlights a new method for surface passivation and device integration. The low SRV values suggest that the semiconductor/oxide interface has a low density of midgap states and that the oxide is a wide band gap material. The relatively low binding energy of the oxidized phosphorus signal is associated with a $Zn_x(PO_3)_y$ species rather than a fully oxidized PO_4 phosphate species [50]. Based on optical characterization of cadmium zinc phosphate glasses with similar oxygen content [66], the phosphorus-rich oxides observed on Zn_3P_2 are likely to have band gaps in excess of 5 eV, significantly greater than that of ZnO at 3.4 eV.

The data suggest that native oxides of Zn_3P_2 are similar in their chemical nature and electronic properties to the native oxides of InP. Oxides such as $In(PO_3)_3$ and In_2O_3 have been incorporated at the interfaces of high efficiency heterojunction [67] and MIS solar cells [68], and can be grown anodically with remarkable quality [69]. The low surface recombination rate of oxidized Zn_3P_2 surfaces measured in this work motivates further effort to apply physical and/or chemical oxidation techniques to Zn_3P_2 surface passivation and device integration.

Chapter 5

Junction Analysis of Mg/Zn_3P_2 Devices

Mg/Zn_3P_2 diodes are the highest performing solar cells based on Zn_3P_2 absorbers to date and reach 6% solar energy conversion efficiency [2]. As-fabricated Mg/Zn_3P_2 solar cells exhibited V_{oc} values below 100 mV, but after 1–2 h annealing in air at 100 °C, V_{oc} values increased to 500–600 mV. The high density of surface defects for freshly etched Zn_3P_2 substrates (chapter 4) is consistent with the low initial performance, but the mechanism of the annealing process has not been elucidated. This chapter explores the nature of the annealing process in Mg/Zn_3P_2 solar cells to instruct new strategies for approaching the higher V_{oc} values of 900–970 mV expected for ideal Zn_3P_2 devices.

5.1 Introduction

Figure 5.1 shows several compelling explanations for the improvement in V_{oc} and barrier height values upon annealing Mg/Zn_3P_2 devices. The first hypothesis suggests that a Mg-doped region of n-type Zn_3P_2 forms under the Mg metal and results in a *p-n* homojunction [36, 70]. The second hypothesis suggests that a Mg_3P_2 or Mg–Zn–P region of n-type conductivity forms under the Mg metal and results in a *p-n* heterojunction [71]. The third hypothesis is that Mg metal acts to passivate surface defects upon annealing and results in a passivated Mg/Zn_3P_2 Schottky diode.

Identifying the most accurate picture would motivate new strategies for investigating Zn_3P_2 devices for solar energy conversion. If the homojunction hypothesis applied, then investigations into high Mg doping levels would enable higher V_{oc} and other dication dopant metals should be explored. If the heterojunction hypothesis

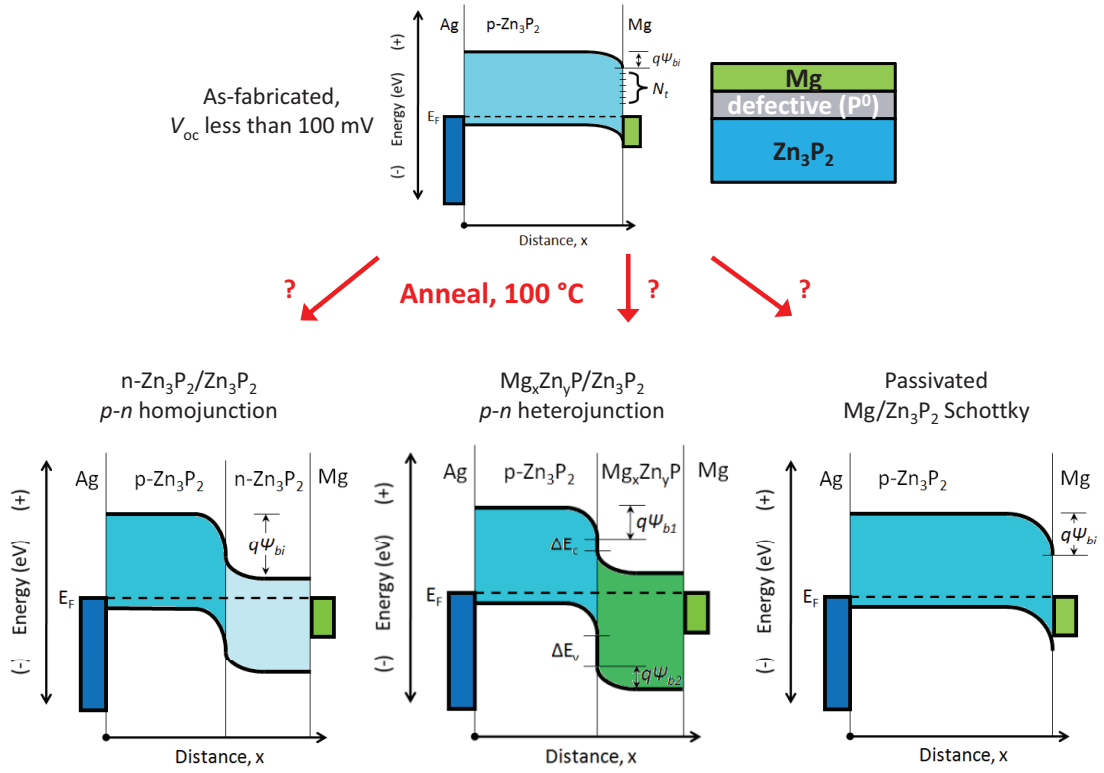

Figure 5.1. Band structure diagrams representing three hypotheses for the annealing process in Mg/Zn_3P_2 devices: (left) Mg-doped p-n homojunction hypothesis, (center) Mg_xZn_yP/Zn_3P_2 p-n heterojunction hypothesis and (right) passivated Mg/ Schottky diode hypothesis.

applied, then investigations in n-type metal phosphides, especially those that could form with reactive metals in contact with Zn_3P_2, should be explored. If the passivation hypothesis applied, then effective methods of removing Mg would allow for other kinds of heterojunctions or semiconductor/liquid junctions to be fabricated using Mg-passivated Zn_3P_2 wafers. The following sections describe the experiments designed to test each of the three hypotheses.

5.2 Mg-Doped *p-n* Homojunctions

The suggestion that Mg/Zn_3P_2 diodes transformed into Mg-doped p-n homojunctions upon annealing in air was the first explanation for the improvement in V_{oc} values ob-

tained by annealing [36, 70]. To assess this hypothesis, we studied the diffusion properties of Mg atoms in Zn_3P_2 as a function of temperature using secondary-ion mass spectrometry (SIMS). In addition, we subjected a series of Mg/Zn_3P_2 solar cells to rapid thermal annealing (RTA) with the goal of obtaining higher Mg doping concentrations and sharper impurity gradients. Finally, we investigated the electronic effects of introducing Mg impurities to Zn_3P_2 by Hall effect measurements and determined that n-type doping by Mg is unlikely to occur in Zn_3P_2.

5.2.1 Mg Impurity Diffusion Profiles

The diffusion of Mg in Zn_3P_2 was investigated quantitatively by secondary-ion mass spectroscopy (SIMS). SIMS analysis was conducted using an O^- primary ion beam at 10 kV and 20 nA that was rastered over the 100×100 μm analysis area. Raw counts for each atomic species (counts·s^{-1}) versus sputtering time (s) were converted into atomic concentration (atoms · cm^{-3}) versus depth (nm). Atomic concentrations of Zn and P were estimated using the stabilized Zn and P counts in the substrate, and atomic concentrations of Mg were estimated using an ion implantation standard with 10^{14} cm^{-2} Mg ions. Sputtering rates were assumed to be constant for SIMS profiling and were approximated using the final crater depth as measured by profilometry. Mg-doping of Zn_3P_2 substrates was performed by solid source diffusion. Zn_3P_2 substrates that had been etched by 2% Br_2 in methanol were metallized with 80 nm of Mg and subjected to heat treatment. Substrates intended for SIMS analysis were annealed at 100–300 °C under active vacuum of $<10^{-6}$ Torr for 20–100 min and stripped of excess Mg with 25 mM EDTA*–10% H_2O_2 (aq, pH 10).

SIMS profiling of the Mg content in Zn_3P_2 substrates doped by solid source diffusion revealed a narrow region of reaction at the Mg/Zn_3P_2 interface as well as penetration of Mg into the substrate at high concentration (figure 5.2a). For diffusions carried out at 100 °C for 100 min, the first 10–50 nm of the sample showed greatly increased Mg and P counts along with Zn depletion. Crystal orientation dependence was ob-

*ethylenediaminetetraacetic acid

served for the Mg profile at depths greater than 100 nm with peak concentrations in the range of 10^{18}–10^{20} cm^{-3} (figure 5.2a, 5.2b). At a depth <500 nm, samples treated at 100 °C showed a return to background levels in Mg concentration of $<10^{15}$ cm^{-3}. Zn_3P_2 substrates treated at 300 °C for 100 min showed an extensive reaction at the Mg/Zn_3P_2 interface in addition to high levels of Mg incorporation in the Zn_3P_2 substrate (figure 5.2c). The first 500 nm of the samples annealed at 300 °C revealed strongly elevated P and Mg counts as well as greatly reduced Zn counts consistent with a Mg–Zn–P alloy rather than a pure Zn_3P_2 matrix. At depths approaching 800 nm–1 μm, a Zn_3P_2 matrix doped with Mg to 10^{19}–10^{20} cm^{-3} was observed. In samples annealed at 300 °C, the depth at which Mg concentration reached baseline appeared to be >2 μm. The observation of Mg impurities in the 10^{16}–10^{19} cm^{-3} range is consistent with the hypothesis of Mg-doped *p*-*n* homojunctions.

5.2.2 Rapid Thermal Annealing of Mg/Zn_3P_2 Devices

A series of solar cells similar to those reported in section 1.5 were subjected to rapid thermal annealing (RTA) treatments with the intention of creating highly Mg-doped n-type emitters for the hypothesized Zn_3P_2 *p*-*n* homojunction solar cells. For a homojunction solar cell, increasing the doping of the emitter region increases the open-circuit potential, V_{oc}. The two conditions explored experimentally were 15-min treatments at 200 °C and 5-min treatments at 300 °C. Treatments above 350 °C were found to damage and roughen the specular finish of the substrates.

The results of annealing treatment at 200 °C are presented in figure 5.3, and contrary to expectations, yielded decreases in V_{oc} for the devices tested. Furthermore, devices heated at 300 °C were completely shorted after the treatment. The degradation in device performance as a function of annealing temperature suggested that Mg impurities either do not behave as n-type dopants with high activation or diffuse too rapidly to yield abrupt *p*-*n* homojunctions.

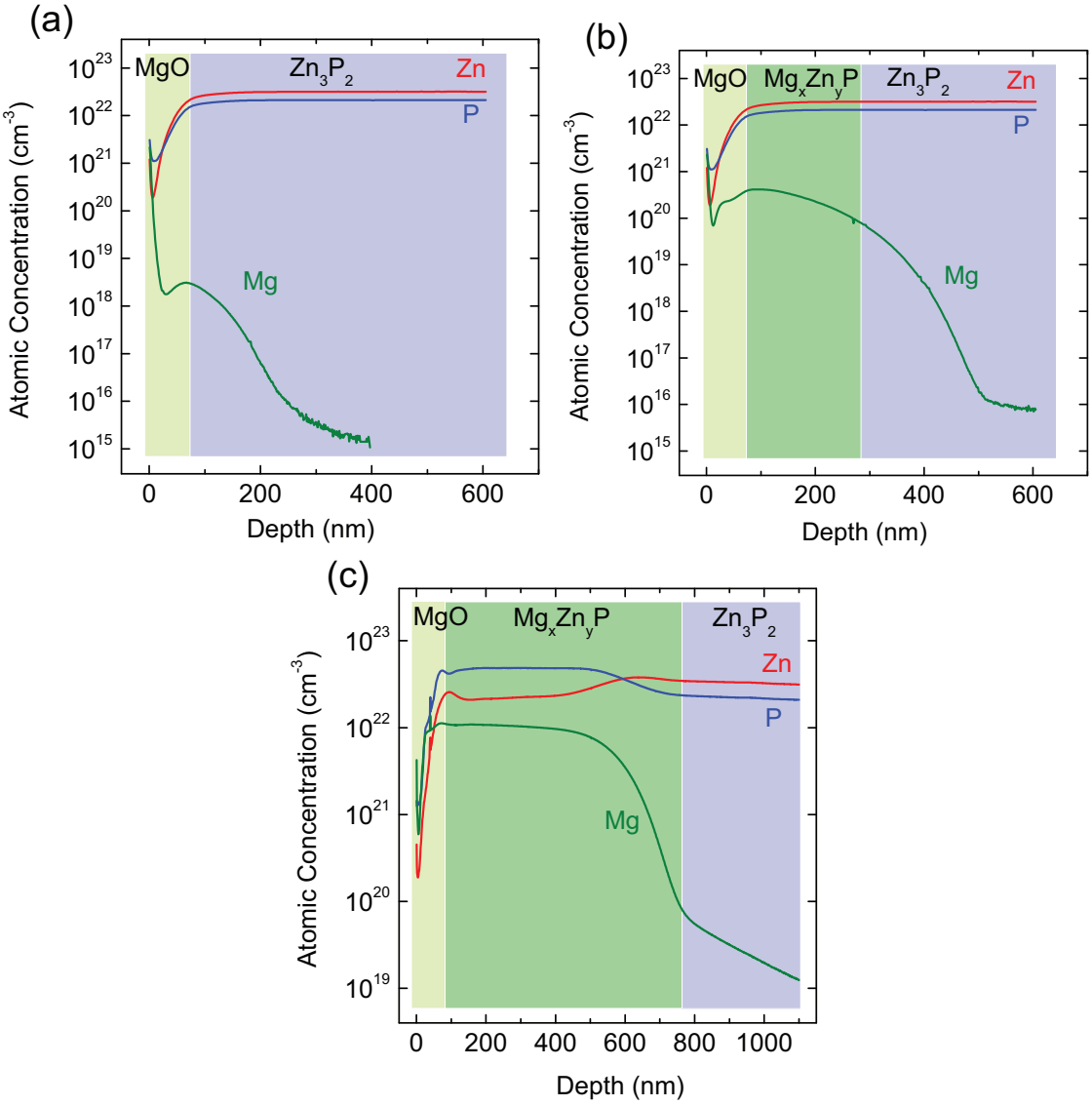

Figure 5.2. Secondary-ion mass spectrometry (SIMS) profiles of Zn, P and Mg atomic concentrations as a function of depth in Zn_3P_2 substrates subjected to solid source doping by Mg. The profiles were collected from Zn_3P_2 substrates that had been annealed at (a), (b) 100 °C and (c) 300 °C under an active vacuum of $<10^{-6}$ Torr for 100 min. Profiles (a) and (b) correspond to regions of different crystallographic orientation on the same Zn_3P_2 substrate.

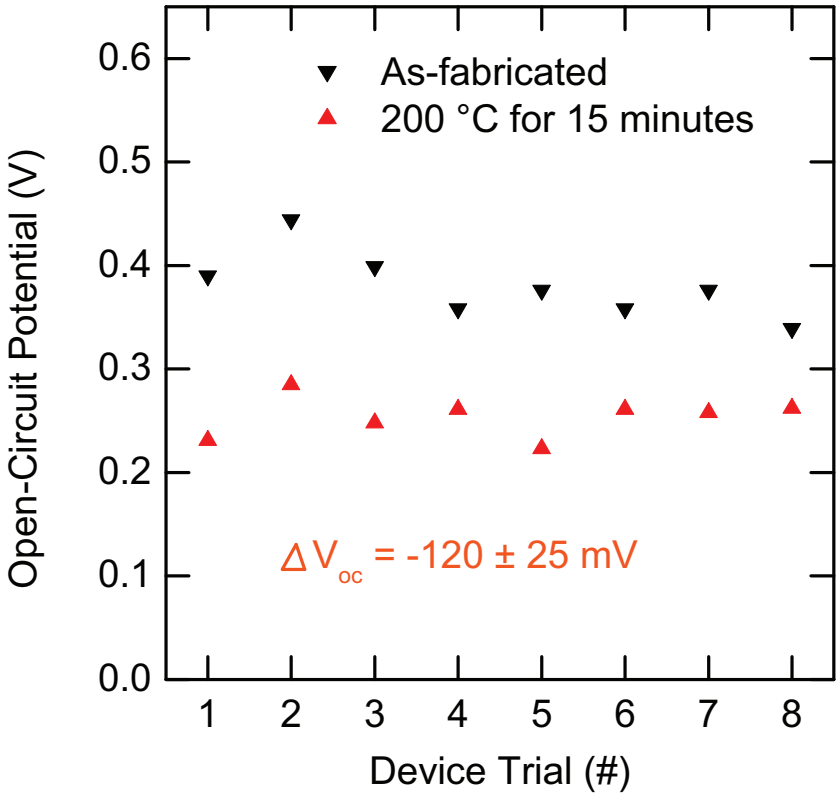

Figure 5.3. Open-circuit voltage of a series of Mg/Zn_3P_2 Schottky diodes under simulated AM1.5 illumination before and after rapid thermal annealing (RTA) treatment of 200 °C for 15 min showing an average $\Delta V_{oc} = -120 \pm 25$ mV.

5.2.3 Electronic Effects of Mg Dopants

To explore the electronic effects of Mg dopants in Zn_3P_2, high levels of Mg impurities were introduced and the effect on majority carrier density and mobility was monitored. Zn_3P_2 substrates were metallized with 80 nm of Mg metal and annealed at 400 °C for 24 h under a variety of annealing ambients. Samples were typically annealed under passive vacuum of $\sim 10^{-5}$ Torr with 15–20 mg of added red phosphorus, and in some trials an additional 30–40 mg of Mg was added. After the annealing treatment, the Zn_3P_2 substrates were stripped of excess Mg with 25 mM EDTA–10% H_2O_2 (aq, pH 10), diced into 2.5×2.5 mm samples appropriate for Hall effect measurements and contacted at the corners with pressed indium.

Substrates doped with Mg at 400 °C showed p-type conductivity with very low acceptor concentrations in the range of 10^{12}–10^{14} cm^{-3} (table 5.1) despite Mg concentrations estimated in the range of 10^{17}–10^{19} cm^{-3}. Mg impurities introduced by solid state diffusion appeared to compensate the intrinsic p-type doping to produce resistive material. Perhaps Mg impurities could be introduced under different conditions and successfully activated as n-type dopants, but in the Mg/Zn_3P_2 solar cells under investigation the formation of Mg-doped *p-n* homojunctions appears unlikely.

5.3 Mg-Alloyed *p-n* Heterojunctions

The first suggestion that Mg/Zn_3P_2 devices might rely on the formation of a *p-n* heterojunction came from Kazmerski et al. who observed evidence of Mg_3P_2 at the junction of annealed Mg/Zn_3P_2 solar cells [71]. The *p-n* heterojunction hypothesis suggests that metal in a Schottky junction with Zn_3P_2 reacts with the underlying Zn_3P_2 substrate to produce a thin n-type alloyed layer that then governs the device performance. The selection of the reactive metal plays a strong role in how the hypothesized *p-n* heterojuction device would operate. A high heat of reaction with Zn_3P_2 is needed to drive the reaction under the mild annealing conditions, and the V_{oc} of the resulting device should be strongly affected by the conduction band offset between the n-type emitter and the p-type Zn_3P_2 substrate.

Table 5.1. Carrier concentration and mobility results from Hall effect measurements of doped Zn_3P_2 substrates, where Mg impurities were introduced by solid source diffusion at 400 °C for 24 h in vacuum ampoules contained small quantities of P and/or Mg

Dopant	Anneal ambient	p (cm^{-3})	μ_p ($cm^2 \cdot V^{-1} \cdot s^{-1}$)
none	none	10^{13} – 10^{14}	16 ± 3
none	P_4	$3.7 \pm 0.4 \times 10^{16}$	12 ± 1
Mg (80 nm)	P_4	$3.8 \pm 0.8 \times 10^{13}$	19 ± 3
Mg (80 nm)	P_4 + Mg	$5.4 \pm 0.8 \times 10^{13}$	41 ± 18
Mg (80 nm)	vacuum	$6.0 \pm 3.2 \times 10^{12}$	48 ± 25
Mg (80 nm)	Mg	$1.5 \pm 0.4 \times 10^{14}$	9 ± 2

5.3.1 Devices Based on Thin Reactive Metals

In section 1.5 and section 5.2.2, microstructured Mg films were used to allow light to penetrate the top contact of the Schottky diode. Microstructured devices are not compatible with bulk SIMS or XPS junction profiling because a lateral uniformity of 100–600 μm is required to collect a profile. To enable combined photovoltaic device analysis and junction profiling techniques, a series of devices were fabricated with 10–50 nm, semitransparent metal films capped with an ITO top contact (figure 5.4).

Ag-doped Zn_3P_2 substrates were incorporated into solar cells with an ITO/Mg/Zn_3P_2 device configuration. Using optical photolithography a series of devices with 1 mm^2 active area were patterned and 10–40 nm Mg followed by 70 nm ITO were deposited by RF magnetron sputtering on Zn_3P_2 substrates that had been etched with 2% Br_2 in methanol. Ag back contacts of 200 nm thickness were then deposited by vacuum evaporation. Photovoltaic performance of the devices was studied under simulated 1 sun AM1.5 illumination at room temperature. Spectral response measurements were conducted at short-circuit using 10 nm band pass pulsed illumi-

nation from a xenon lamp source and under 1 sun light bias.

Figure 5.4 displays the light J–V results from ITO/Mg/Zn_3P_2 solar cells as-fabricated and after annealing at 100 °C in air. The performance of devices with 30 and 20 nm thick Mg layers is shown in red and blue, respectively. For solar cells with a 30 nm Mg layer, as-fabricated devices exhibited poor V_{oc} values $\leq$100 mV, but annealing at 100 °C for 100 min in air greatly improved the junction properties and yielded V_{oc} values reaching 550 mV. The low observed J_{sc} values were consistent with expected reflection losses from the optically-thick 30 nm Mg layer. For solar cells with a 20 nm Mg layer, annealing at 100 °C in air also increased V_{oc} values, but only to 300–400 mV. The lower V_{oc} values were likely due to increased shunting because thinner $\leq$15 nm Mg layers (data not shown) resulted in cells that were shorted. J_{sc} values reaching 26.0 $mA \cdot cm^{-2}$ and solar energy conversion efficiencies of 2.7% were observed in the cells with 20 nm Mg layers due to reduced reflection losses from the Mg metal. The spectrally-resolved external quantum yield data also showed the strong relationship between Mg layer thickness and photocurrent in ITO/Mg/Zn_3P_2 solar cells (figure 5.5). Although devices with a 30 nm Mg layer showed less than 20% external quantum yield, devices with thinner 20 nm Mg layers were observed to have external quantum yields approaching 80%. Minority carrier diffusion lengths of $\geq$3 μm were estimated from the external quantum yield data in the 650–850 nm spectral range using previously reported absorption data (figure 3.3) and assuming a depletion width of 300 nm in the Zn_3P_2 [72]. As demonstrated in the device results, the annealing treatment of Mg/Zn_3P_2 diodes was critical for improved device performance.

Devices incorporating Ca metal but otherwise similar to those reported above were also investigated. From the the values of table 5.2, Ca is expected to react more strongly with Zn_3P_2 than Mg, and the resulting Ca_xZn_yP layers may be of lower electron affinity than Mg_xZn_yP layers. Solar cells with Ca or Ca/Mg bilayers as the reactive metal layers exhibited improved as-fabricated V_{oc} values compared to solar cells with only Mg as the reactive layer (figure 5.6). Ca was found to react more strongly with the ITO layer than Mg in control tests on glass slides. In no cases were

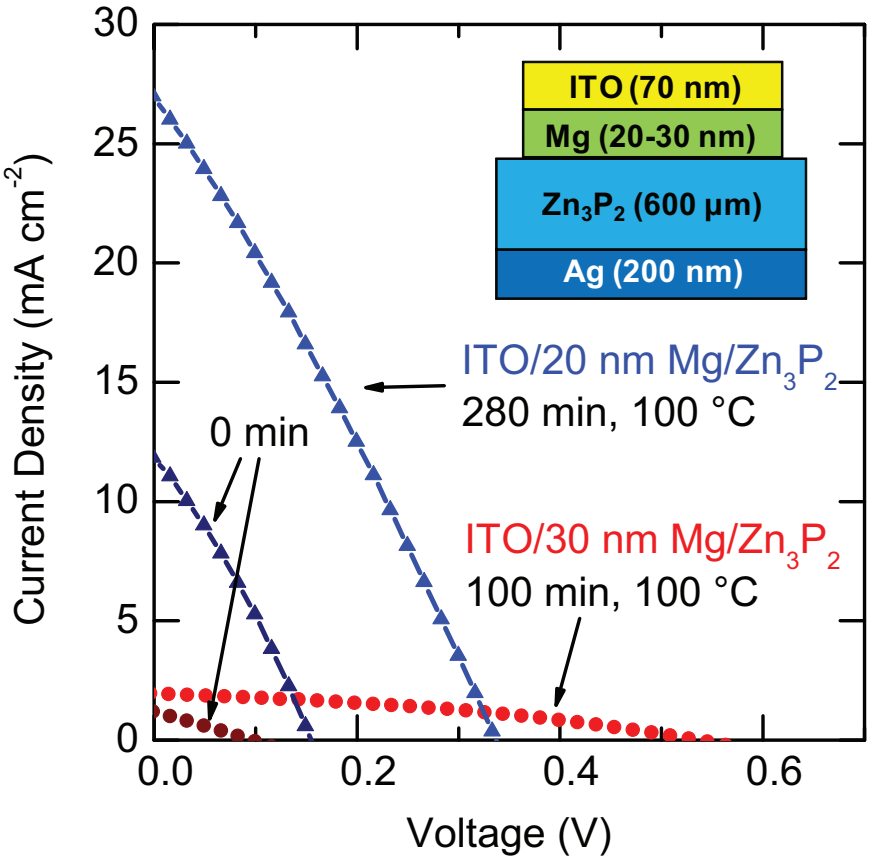

Figure 5.4. Photovoltaic performance under simulated AM1.5 illumination observed in ITO/Mg/Zn_3P_2 solar cells. Red traces show annealed devices with 30 nm Mg layer, where dark red corresponded to the as-fabricated device; and blue traces show the annealed devices with 20 nm Mg layer, where dark blue corresponds to the as-fabricated device.

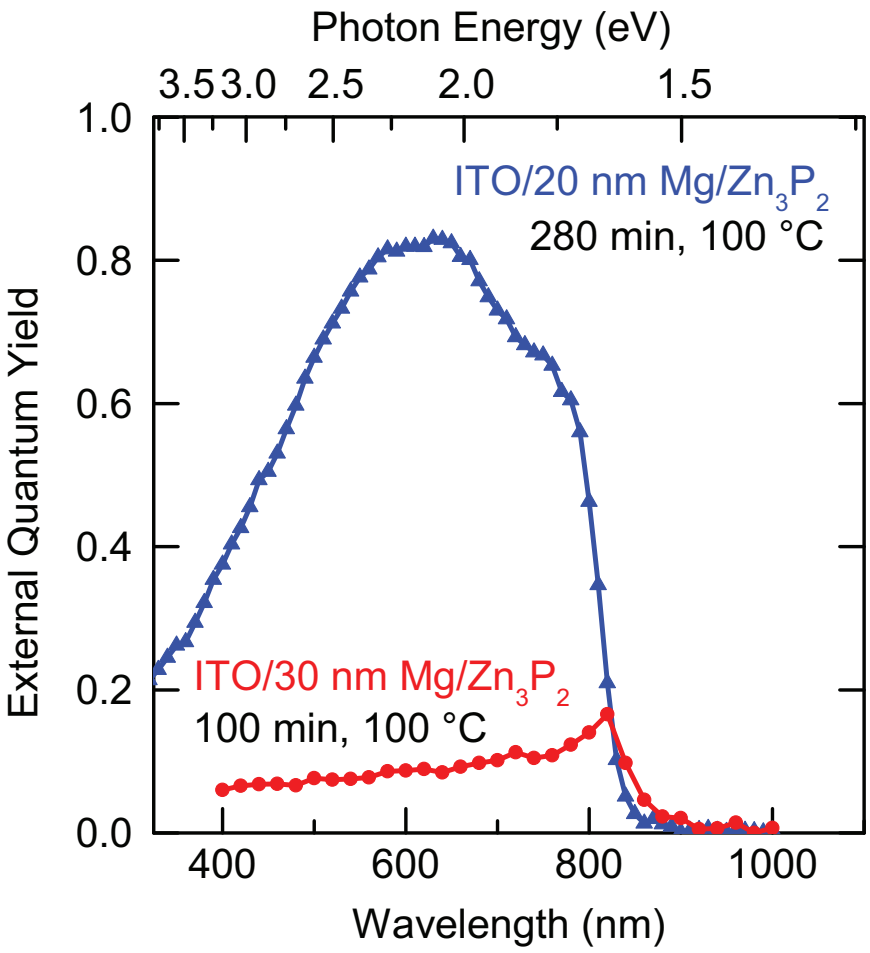

Figure 5.5. External quantum yield observed in ITO/Mg/Zn_3P_2 solar cells after annealing at 100 °C in air. Devices with 20 nm Mg layers (blue) show high external quantum yield, but devices with 30 nm Mg layers (red) show reduced external quantum yield due to reflection losses.

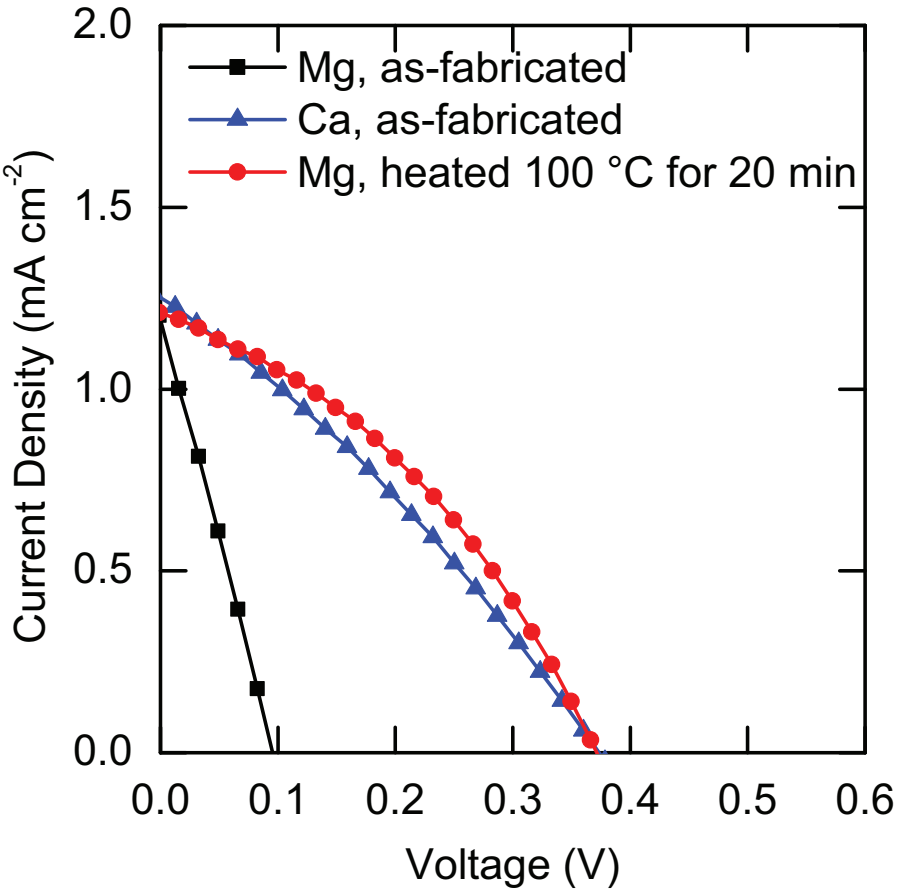

Figure 5.6. Photovoltaic performance under simulated AM1.5 illumination observed in ITO/Mg/Zn_3P_2 and ITO/Ca/Zn_3P_2 solar cells. Without an annealing treatment, ITO/Ca/Zn_3P_2 devices (blue triangles) show improved V_{oc} values as compared to ITO/Mg/Zn_3P_2 devices (black squares). ITO/Mg/Zn_3P_2 devices required an annealing treatment at 100 °C for 20 min (red circles) to reach comparable V_{oc} values to ITO/Ca/Zn_3P_2 devices without annealing.

Table 5.2. Compiled data of metal work function, ionic radius, and heat of phosphide formation for a series of metals that display reactivity with phosphorus [63, 73]

Element	Φ (eV)	Ionic radius (Å)	Compound	ΔH_f° (kJ·(mol·P)$^{-1}$)
Zn	4.3	0.74	Zn_3P_2	–240
Mg	3.68	0.65	Mg_3P_2	–416
Ca	2.9	0.99	Ca_3P_2	–543
Sr	2.59	1.12	Sr_3P_2	–607
Ti	4.33	0.61	TiP	–275
Zr	4.05	0.72	ZrP	–402

V_{oc} values observed over 400 mV in solar cells incorporating Ca reactive layers, but altering the reactive metal species in Zn_3P_2 solar cells remains a promising route to devices with improved V_{oc} values.

5.3.2 Junction Profiling

ITO/Mg/Zn_3P_2 solar cells annealed at 100 °C for 24–72 h showed obvious contrast between devices that was dependent on the crystallographic orientations of the substrate (figure 5.7). The light yellow devices appeared similar to the as-fabricated devices, but the dark green devices only changed appearance after 24–72 h annealing at 100 °C. The junction profiling presented later in this section combined with electron backscattered diffraction (EBSD) identified the light yellow devices as low-diffusivity grains with (110) orientation and the dark green devices as high-diffusivity grains with (010) orientation. Inspection of the crystal structure along the (110) orientation shows a dense network of zinc atoms and along the (010) orientation shows channels in the network of zinc atoms. During the period of greatest V_{oc} increase, the first 100 min of annealing at 100 °C, both high- and low-diffusivity orientations showed

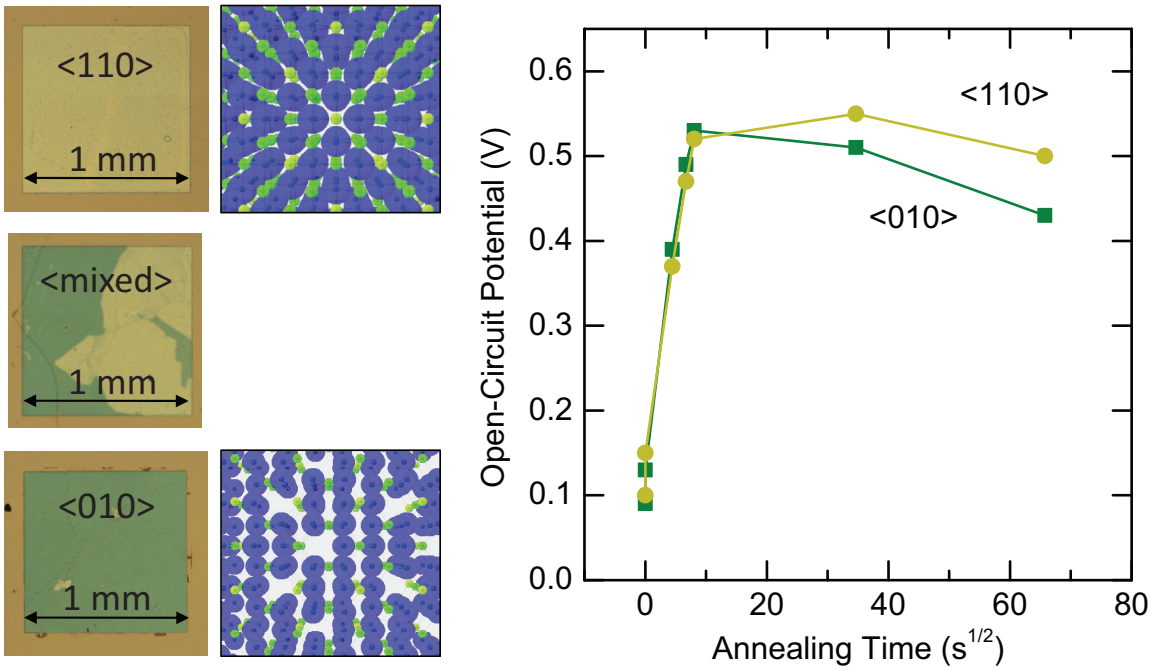

Figure 5.7. (a) micrographs of ITO/Mg/Zn_3P_2 solar cells after 72 h annealing at 100 °C with orientations identified by electron backscattered diffraction (EBSD). Crystal structure images, with phosphorus atoms as green and zinc atoms as blue, show channels in the (010) direction where Mg diffusion occurs readily, (b) V_{oc} as a function of annealing at 100 °C for ITO/Mg/Zn_3P_2 solar cells.

the same V_{oc} trends. However, after longer annealing times of 1–3 days, the highly diffusive grains exhibited faster degradation. The evidence suggests that Mg-alloying is not the critical step required for improved V_{oc} in Mg/Zn_3P_2 devices.

Junction profiling of the metal-semiconductor junction was performed using secondary-ion mass spectrometry (SIMS) and x-ray photoelectron spectroscopy (XPS). The ITO/Mg/Zn_3P_2 devices used for composition profiling were fabricated using 30 nm of Mg followed by 70 nm of ITO, annealed for 72 h at 100 °C in air, and exhibited V_{oc} values from 450 to 550 mV. Sputtering rates were assumed to be constant for both SIMS and XPS profiling and were approximated using the crater depth as measured by profilometry. SIMS analysis was conducted using an O^- primary ion beam at 10 kV and 20 nA that was rastered over the 100×100 μm analysis area. Atomic concentrations of Zn and P were estimated using the stabilized Zn and

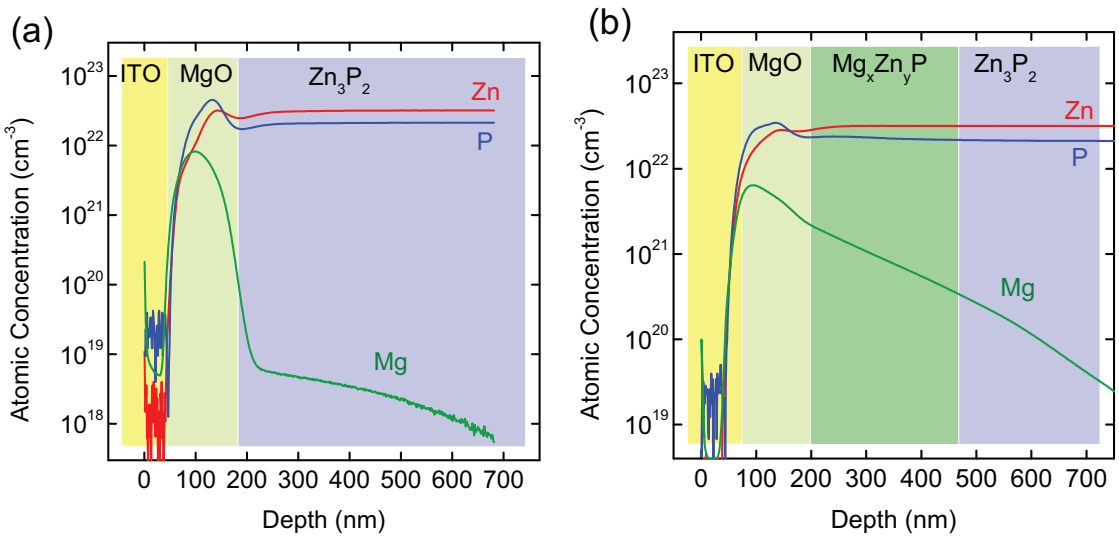

Figure 5.8. Secondary-ion mass spectrometry (SIMS) profiles of ITO/Mg/Zn_3P_2 devices that were annealed for 72 h at 100 °C where (a) close to the (110) orientation and (b) is close to the (010) orientation.

P counts in the substrate, and atomic concentrations of Mg were estimated using an ion-implantation standard with 10^{14} cm^{-2} Mg ions.

SIMS profiling was performed to probe the composition of the interface after annealing ITO/Mg/Zn_3P_2 solar cells (figure 5.8). Quantitative SIMS analysis was used in regions with >99% Zn_3P_2 composition to directly measure Mg impurity concentrations. However, in mixed regions the SIMS data was only qualitatively reliable due to the unknown matrix. After reading baseline counts in the ITO layer, the next layer was assigned as MgO from the XPS profiling data. For the grains of the Zn_3P_2 substrate with (110) orientation (figure 5.8a), essentially no Mg-alloyed Zn_3P_2 was observed although a Mg-doped Zn_3P_2 region with impurity concentrations of 10^{18}–10^{19} cm^{-3} was still present. For the grains of the Zn_3P_2 substrate with (010) orientation (figure 5.8b), a 1% to 10% Mg-rich Zn_3P_2 alloyed region was observed followed by Mg-doped Zn_3P_2 with Mg impurity concentrations of 10^{19}–10^{21} cm^{-3}.

XPS profiling measured the atomic concentration and oxidation state of elements across the junction by monitoring the photoelectrons from In $3d_{5/2}$, O $1s$, Mg KLL, Zn $2p_{3/2}$, and P $2s$ core levels. Monochromated x-rays of 1468.7 eV from an Al K-α

source were used to eject photoelectrons from the sample which were collected with the detector 0° from the surface normal. Ar-ion sputtering steps at 2 kV were alternated with XPS analysis to profile the junction. For each step, the photoelectron spectra from the In $3d_{5/2}$, O $1s$, Zn $2p_{3/2}$, and P $2s$ core levels were fit using a Tougaard baseline and a single Gaussian–Lorentzian product line shape to compute the area. The Mg KLL Auger region was fit by three line shapes that were assigned to MgO at binding energy 305.5 eV (kinetic energy of 1181.2 eV), elemental Mg at 301.0 eV (1185.7 eV) and Mg–Zn–P at 303.0 eV (1183.7 eV) [74]. The relative sensitivity factor (RSF) for In $3d_{5/2}$, O $1s$, Zn $2p_{3/2}$, and P $2s$ core levels were taken from tabulated values, and the RSF for Mg KLL was estimated using the observed Zn LMM to Zn $2p_{3/2}$ photoelectron count ratio and the tabulated Zn LMM to Mg KLL photoelectron count ratio [49].

Figure 5.9 shows XPS profiling data where the concentration and bonding environment of In, O, Mg, Zn, and P were tracked across the junction interface of annealed ITO/Mg/Zn_3P_2 solar cells. The behavior of In, O, Zn, and P showed little intermixing and the profile clearly transitioned past ITO after 100 nm and into bulk Zn_3P_2 after several hundred nanometers into the profile. The Mg KLL photoelectron spectra showed complex behavior during the transition from ITO to Zn_3P_2 and was fit by line shapes corresponding to MgO, Mg metal, and Mg–Zn–P. After the ITO layer, the MgO signal centered at binding energy 305.5 eV was found to increase rapidly along with a small Mg metal signal centered at 301.0 eV. For the grains of the Zn_3P_2 substrate with (110) orientation (figure 5.9a), the Mg–Zn–P signal at binding energy 303.0 eV was negligible, and after the MgO layer the Mg KLL region exhibited a baseline count rate. For the grains of the Zn_3P_2 substrate with (010) orientation (figure 5.9b), the Mg–Zn–P signal at binding energy 303.0 eV grew in to become the dominant signal in the Mg KLL region. After several hundred nanometers into the profile, the Mg–Zn–P signal decreased to yield the bulk Zn_3P_2 composition of the substrate.

Figure 5.10 shows the TEM cross section of ITO/Mg/Zn_3P_2 solar cells that had been annealed at 100 °C for 100 min, the optimal annealing condition for improved

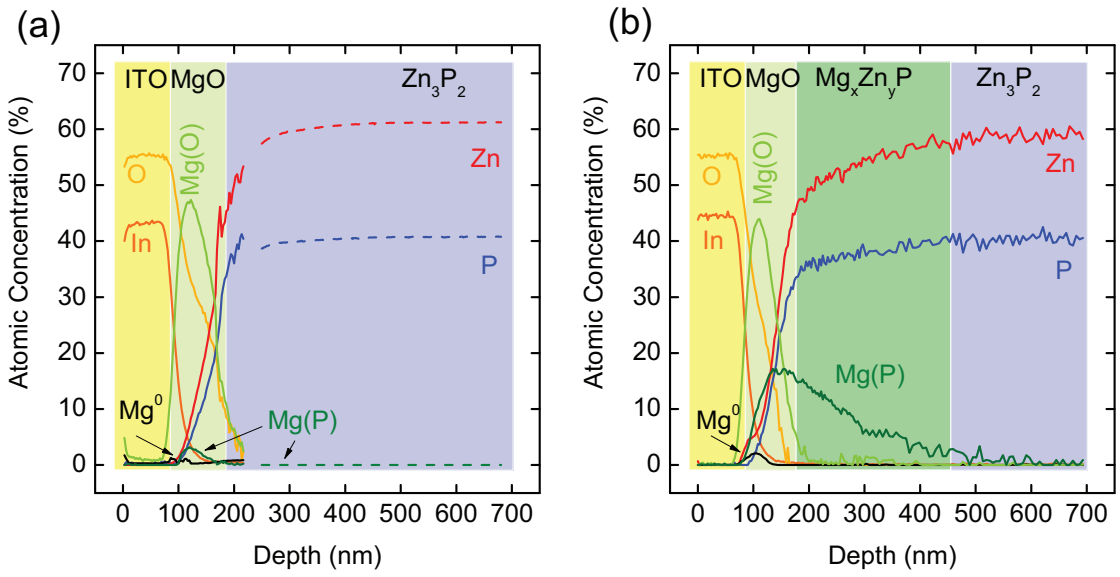

Figure 5.9. X-ray photoelectron spectroscopy (XPS) sputtered profiles of ITO/Mg/Zn_3P_2 devices that were annealed for 72 h at 100 °C where (a) close to the (110) orientation and (b) is close to the (010) orientation.

V_{oc} values. Cross-sectional samples of the solar cells were prepared by focused ion beam milling after deposition of a protective layer of Cr metal onto the devices. The TEM instrument used for the measurement was a JEOL 2010F FEG electron microscope operating at 200 keV electron energy. The TEM profile showed 2.65 ± 0.05 Å fringes between the ITO and Zn_3P_2 layers, matching the (002) planes for Mg metal. The Zn_3P_2 substrate in contact with the Mg metal showed an abrupt interface and no significant Mg alloying after annealing at 100 °C for 100 min.

Alloyed layers of Mg–Zn–P were only observed in ITO/Mg/Zn_3P_2 solar cells fabricated with Zn_3P_2 substrates of certain crystallographic orientations and after annealing times of >24 h at 100 °C. Devices fabricated on Zn_3P_2 with (010) orientation showed 100–200 nm of Mg–Zn–P material after 72 h annealing at 100 °C, but devices fabricated on Zn_3P_2 with (110) orientation showed no evidence for Mg–Zn–P formation by SIMS or XPS profiling. TEM profiles of devices subjected to 100 min of annealing at 100 °C revealed an abrupt (<5 nm) interface between Mg metal and the Zn_3P_2 substrate. The results suggest that *p*-*n* heterojunction formation via Mg

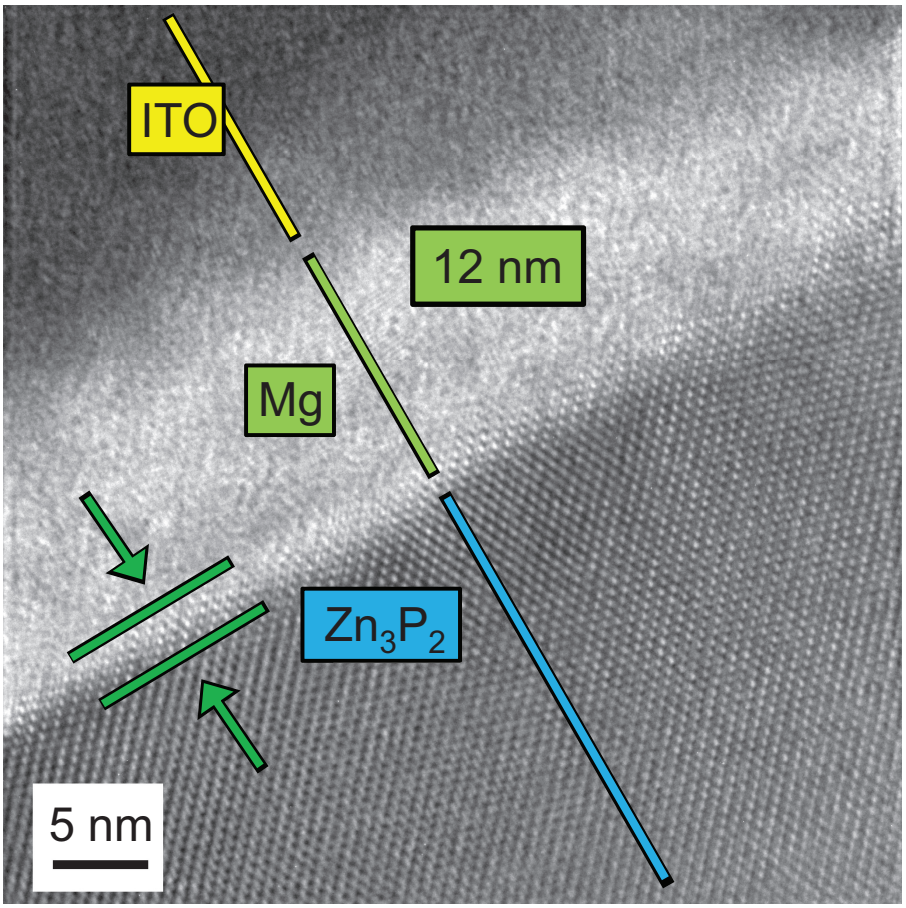

Figure 5.10. Transmission electron microscopy (TEM) of the ITO/Mg/Zn_3P_2 junction interface showing the presence of Mg metal and <5 nm region of reaction between the Mg metal and Zn_3P_2 substrate.

alloying with the Zn_3P_2 substrate is not likely to be responsible for improved V_{oc} values for Mg/Zn_3P_2 diodes annealed for 100 min at 100 °C.

5.4 Mg Passivation of Zn_3P_2 Surface Defects

Another explanation for the improved V_{oc} values observed in annealed Mg/Zn_3P_2 devices is that the Mg metal passivates the surface defects of freshly etched Zn_3P_2 substrates. In chapter 4 we showed that Zn_3P_2 substrates freshly etched with 2% Br_2 in methanol had high surface recombination rates that correlated with the presence of elemental phosphorus (P^0) impurities at the surface. Reaction with Mg metal removed P^0 impurities and reduced the density of interface defects in Mg/Zn_3P_2 devices, increasing the V_{oc} observed in annealed Mg/Zn_3P_2 devices. One route to improved devices based on Zn_3P_2 substrates is optimizing the reactive metal passivation and using the passivated Zn_3P_2 substrates to fabricate solid state *p*-*n* heterojunctions.

5.4.1 Surface Composition

Zn_3P_2 substrates were subjected to Mg metallization and annealing to assess the effect of the treatment on surface composition. Before metallization the Zn_3P_2 substrates were etched with 2% Br_2 in methanol for 30 s to remove residual oxidation and polishing damage. Substrates were sputtered with 100 nm of Mg metal using an RF source at 25 W and a sputter rate of $\approx$1 nm $\cdot$ min^{-1} in 3 mTorr Ar pressure. Then the Zn_3P_2 substrates were annealed at 100 °C for 90 min and the Mg metal was etched in 20 mM EDTA–10% H_2O_2 (aq, pH 10). The etch was complete in 2–5 s, after which the substrate was rinsed and immediately introduced into the x-ray photoelectron spectroscopy (XPS) analysis chamber.

The composition and oxidation state of the Zn_3P_2 substrate was monitored by XPS analysis as shown in figure 5.11. After treatment with Mg metal, the signal from the Zn $2p_{3/2}$ and P $2p$ core electrons was consistent with a Zn_3P_2 substrate largely free of residual elemental phosphorus and oxidation. For Zn_3P_2 substrates that had been treated with Mg metal and then etched for 2–5 s in 20 mM EDTA–10% H_2O_2 (aq, pH

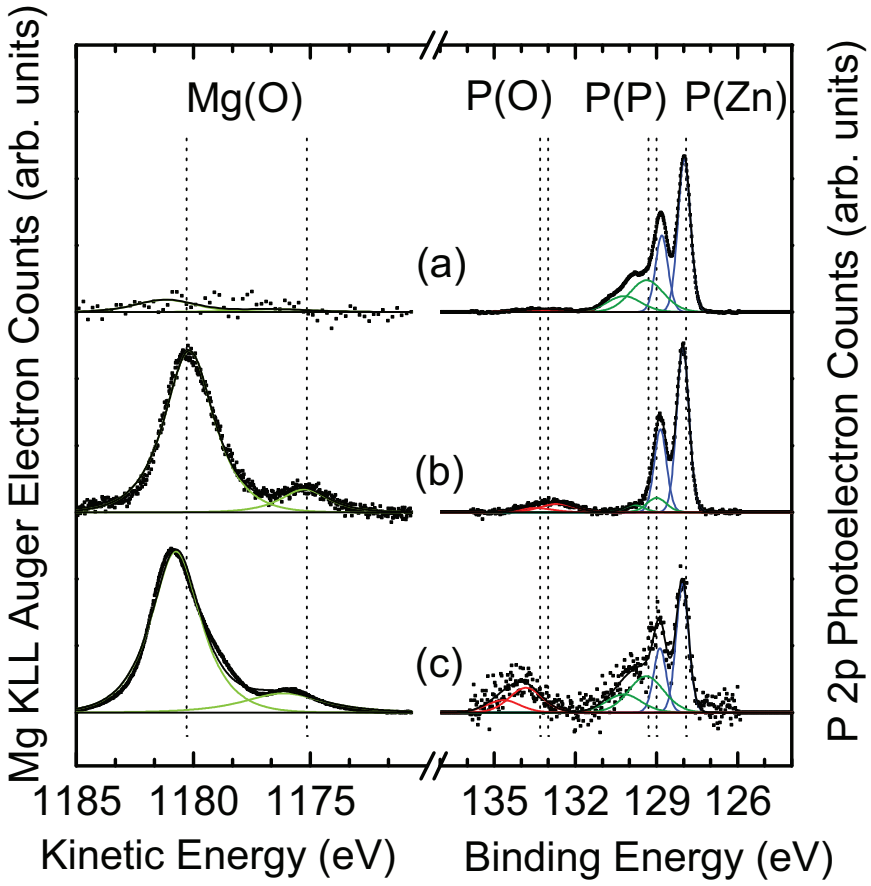

Figure 5.11. Auger electron spectra of the Mg KLL region (left) and XP spectra of the P 2*p* region (right) for Zn_3P_2 substrates that were (a) polished, (b) metallized with 100 nm of Mg metal, annealed at 100 °C for 90 min, and etched in 20 mM EDTA–10% H_2O_2 (aq, pH 10) for 4 s, and (c) metallized with 100 nm of Mg metal, annealed at 100 °C for 90 min, and etched in 20 mM EDTA–10% H_2O_2 (aq, pH 10) for 60 s.

10), only 1–2 nm of MgO was observed at the surface. Zn_3P_2 substrates that were instead etched for 60 s showed the presence of 10–15 nm of MgO. The MgO residue left by the chemical etching step was expected to degrade device performance for Zn_3P_2 substrates, motivating futher work with other metallizations (such as Ca) or other etching treatments (such as organic acids in nonaqueous solvents). The results of the surface composition analysis indicated that Zn_3P_2 substrates exhibited minimal elemental phosphorus contamination after metallization, annealing, and removal of Mg metal and supported the hypothesis that Mg metal passivates Zn_3P_2 surface defects.

5.4.2 Photoelectrochemical Measurements

As confirmation of the high quality of Zn_3P_2 substrates treated with Mg, photoelectrochemical measurements were performed on both freshly etched and Mg-treated substrates. These measurements were conducted as described in appendix C. Photoelectrochemical measurements serve as a very sensitive means of assessing surface quality for semiconductor absorbers. The selection of the electrolyte and redox couple allows for a rectifying contact to be made for a semiconductor of known doping and electron affinity. For Zn_3P_2 substrates as prepared in appendix A, an electrolyte containing $CoCp_2^{+/0}$ was expected to yield a high barrier contact.

Zn_3P_2 substrates etched with 2% Br_2 in methanol for 30 s consistently revealed low open-circuit voltage values when tested in contact with $CoCp_2^{+/0}$. Further treatment in 10% HF–0.25% H_2O_2 (aq) allowed for somewhat increased open-circuit voltage values to be observed. Figure 5.12 shows the low, ∼50 mV V_{oc} for Zn_3P_2 substrates etched in 2% Br_2 in methanol and increased V_{oc} values, ∼100 mV, for Zn_3P_2 substrates that were etched in 2% Br_2 in methanol and subsequently treated in 10% HF–0.25% H_2O_2 (aq).

To assess the electronic quality of Zn_3P_2 surfaces that had been annealed with Mg metal, electrodes were fabricated with Zn_3P_2 substrates for which the Mg had been annealed but not yet removed. Then, after the epoxy had cured and the electrode was ready for testing, the Mg was etched away and the photoelectrochemical properties

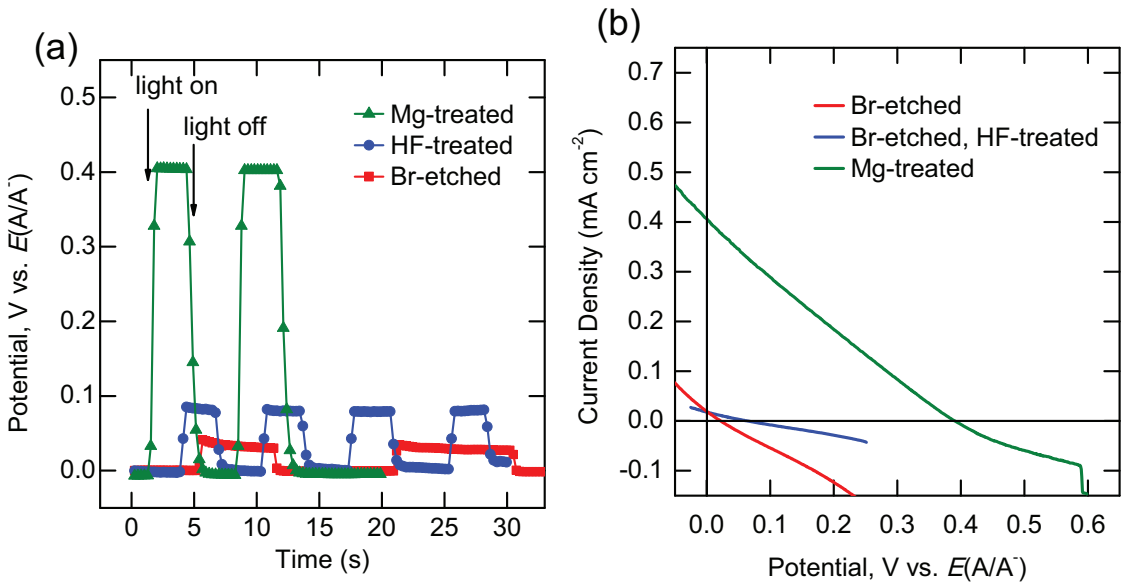

Figure 5.12. Photoelectrochemical properties of chemically treated Zn_3P_2 substrates in contact with CH_3CN–1.0 M $N(Bt)_4{\cdot}PF_6$ containing 0.020 M $CoCp_2^+$–0.002 M $CoCp_2$. (a) Open-circuit potential as a function of time for flashed simulated 1 sun illumination, (b) J–E curves under simulated 1 sun illumination. "Mg-treated" Zn_3P_2 substrates were metallized with 100 nm of Mg metal, annealed at 100 °C for 90 min, and etched in 5 mM EDTA (aq, pH 10) for 15 s. "HF-treated" Zn_3P_2 substrates were etched with 2% Br_2 in methanol 30 s and then treated in 10% HF–0.25% H_2O_2 (aq) for 60 s. "Br-etched" Zn_3P_2 substrates were etched with 2% Br_2 in methanol for 30 s.

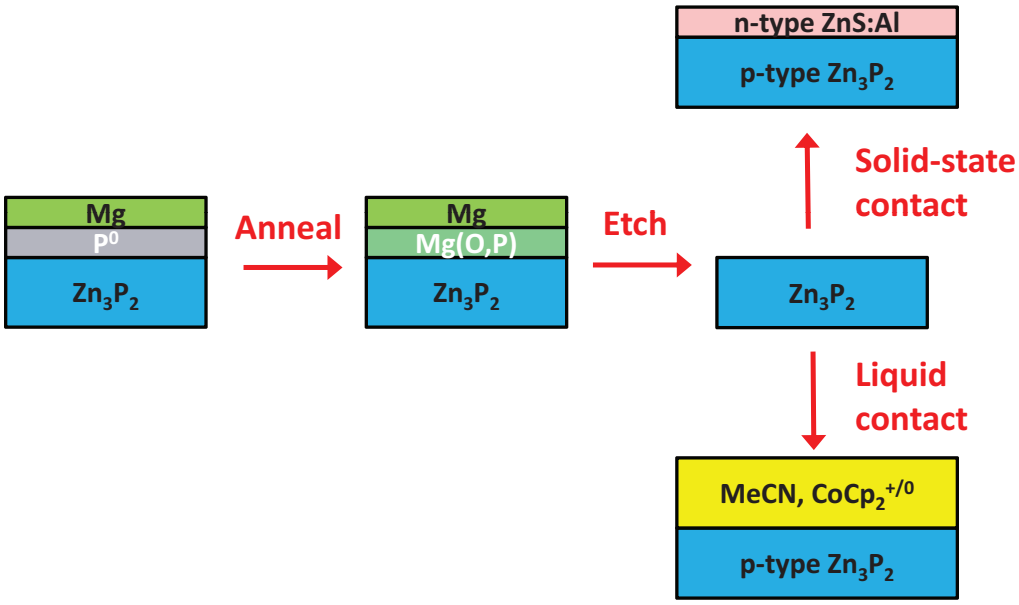

Figure 5.13. Schematic depicting the proposed process of Mg-passivation for Zn_3P_2 substrates where Zn_3P_2 substrates are metallized with 100 nm of Mg metal, annealed at 100 °C for 90 min, and etched in 25 mM EDTA–10% H_2O_2 (aq, pH 10) for 4 s. The resulting passivated Zn_3P_2 substrates are then incorporated into solid state *p*-*n* heterojunctions or photoelectrochemical cells.

of the electrodes were measured. For Zn_3P_2 substrates metallized with 100 nm of Mg metal, annealed at 100 °C for 90 min, and etched in 5 mM EDTA (aq, pH 10) for 15 s, the V_{oc} values observed in contact with $CoCp_2^{+/0}$ were >400 mV.

The *J*–*E* data shown in figure 5.12b demonstrate the large improvements of V_{oc} for Zn_3P_2 substrates annealed with Mg compared to those that were freshly etched in 2% Br_2 in methanol. The other device parameter such as fill factor and J_{sc} appeared to be strongly limited by series resistance due to MgO overlayers apparent from the XPS spectra (figure 5.11). Mg impurities that had diffused into the bulk wafer to create a resistive, Mg-doped region (such as in table 5.1) also contributed to increased series resistance.

Several methods could allow for improved performance of the Zn_3P_2 substrates in the photoelectrochemical cell. One route would explore other reactive metals that undergo the passivation reaction more readily. Section 5.2 showed that Mg impurities

were highly diffusive and also electrically compensating. Another metal such as Ca or Sr could yield the same passivation effect but with shorter annealing times or even at room temperature. The device work presented in figure 5.6 earlier is consistent with the hypothesis that Ca metal undergoes passivation reactions with Zn_3P_2 under ambient conditions. Another direction would be the development of a chemical etchant for Mg metal that did not leave MgO residue. One promising nonaqueous etchant for Mg metal is a solution of an organic acid such as pyridinium triflate in tetrahydrofuran or methanol. Such a solution readily removes Mg metal and would be unlikely to produce residual MgO, but the nature of the resulting Zn_3P_2 surface has not yet been investigated.

The surface composition and electrochemical measurements are consistent with the hypothesis that Mg metal passivates surface defects of freshly etched Zn_3P_2 substrates. The resulting surface can be incorporated into other devices such as photoelectrochemical cells and also solid state *p-n* heterojunctions (figure 5.13). The passivation of Zn_3P_2 by a solid state reactive species appears to be a promising route to improved device performance of both thin film and bulk Zn_3P_2 absorbers.

5.5 Conclusions

We have presented evidence that the increased V_{oc} values measured for annealed Mg/Zn_3P_2 solar cells are the result of the passivation of Zn_3P_2 surface defects by Mg metal. Mg-doped *p-n* homojunction and Mg-alloyed *p-n* heterojunction formation are not likely to account for the increased V_{oc} values observed in Mg/Zn_3P_2 solar cells.

Experiments to prepare n-type Zn_3P_2 through the incorporation of Mg impurities only yielded resistive Zn_3P_2 material for a variety of conditions. The results suggest that Mg-doping occurs in Mg/Zn_3P_2 diodes but that it is a degradation process by which the series resistance of the Zn_3P_2 substrate is increased and the fill factor is reduced.

Up to several hundred nanometers of alloyed Mg–Zn–P has been observed in SIMS

and XPS junction profiles for ITO/Mg/Zn_3P_2 devices subjected to 72 h annealing at 100 °C. However, for devices only heated for 1–2 h the alloyed region appears to be <5 nm in thickness. In addition, the increases in V_{oc} with annealing appear to be independent of orientation, but the Mg-alloying behavior is strongly orientation dependent. The results suggest that the formation of an n-type Mg–Zn–P layer within 100 min of annealing at 100 °C of sufficient thickness to create a *p*-*n* heterojunction is unlikely.

The hypothesis that Mg metal reacts with Zn_3P_2 to passivate surface defects is supported by both the device results and surface composition analysis. ITO/Mg/Zn_3P_2 devices begin with V_{oc} values <100 mV that are increased to 400–600 mV during annealing at 100 °C. Zn_3P_2 substrates that were metallized with 100 nm of Mg, annealed at 100 °C for 90 min, and etched in 25 mM EDTA–10% H_2O_2 (aq, pH 10) for 4 s show significantly reduced residual P^0 surface overlayers and greatly improved performance in semiconductor/liquid junctions, consistent with the hypothesis that Mg metal passivates the surface defects of freshly etched Zn_3P_2 substrates.

Chapter 6

High Open-Circuit Voltage from Cu_2O/CH_3CN Junctions

P-type cuprous oxide (Cu_2O) photoelectrodes prepared by the thermal oxidation of Cu foils exhibited open-circuit voltages in excess of 800 mV in nonaqueous regenerative photoelectrochemical cells. In contact with the decamethylcobaltocene$^{+/0}$ ($Me_{10}CoCp_2^{+/0}$) redox couple, cuprous oxide yielded open-circuit voltage, V_{oc}, values of 820 mV and short-circuit current density, J_{sc}, values of 3.1 mA $\cdot$ cm^{-2} under simulated air mass 1.5 illumination. The energy conversion efficiency of 1.5% was limited by solution absorption and optical reflection losses that reduced the short-circuit photocurrent density. Spectral response measurements demonstrated that the internal quantum yield approached unity in the 400–500 nm spectral range, but poor red response, attributable to bulk recombination, lowered the overall efficiency of the cell. X-ray photoelectron spectroscopy and Auger electron spectroscopy indicated that the photoelectrodes had a high-quality Cu_2O surface, and revealed no observable photocorrosion during operation in the nonaqueous electrolyte. The semiconductor/liquid junctions thus provide a noninvasive method to investigate the energy conversion properties of cuprous oxide without the confounding factors of deleterious surface reactions.

6.1 Introduction

Cuprous oxide (Cu_2O) is an attractive material for water photoelectrolysis and for photovoltaics because of its low cost, high availability, and straightforward processing

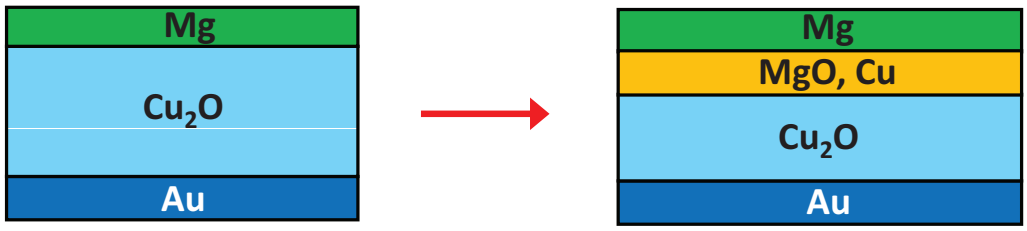

Figure 6.1. Schematic of Cu precipitation in Cu_2O solar cells showing the reaction of a metal, in this case Mg, with Cu_2O to yield metal oxide and elemental Cu. The interfacial Cu formation reaction limits solar cells based on Cu_2O absorbers by transforming them into low barrier height Cu/Cu_2O Schottky diodes.

[75, 76, 77]. Cu_2O is a p-type semiconductor doped by intrinsic copper vacancies, with a 2.0 eV band gap and high absorption coefficient in the visible region [75, 76, 78, 79]. Cu_2O synthesized by high temperature thermal oxidation of Cu has been shown to have high hole mobilities and long minority carrier diffusion lengths [75, 80, 81].

The efficiency of Cu_2O solar cells is however limited by the difficulty of preparing high-quality n-type Cu_2O and by the lack of a suitable n-type heterojunction partner. Interfacial chemical reactions at Cu_2O/metal Schottky junctions result in the precipitation of deleterious Cu metal that lowers the barrier height of the resulting Schottky junctions and limits the open-circuit voltage to <350 mV [75, 82]. Interfacial Cu formation also degrades the performance of p-Cu_2O heterojunctions formed from metal-insulator-Cu_2O contacts and transparent conducting oxide (TCO)/Cu_2O heterojunctions incorporating ZnO, In_2O_3, SnO_2, or CdO [83, 84, 85, 86, 87]. Figure 6.1 depicts the general schematic of interfacial Cu formation. Devices with higher barrier heights have been fabricated by minimizing interfacial Cu formation. For example, a Cu_2O/ZnO heterojunction solar cell has been reported to display an open-circuit voltage of 680 mV and an energy conversion efficiency of 3.8% [88].

Semiconductor/liquid junctions present an alternative to conventional solid-state photovoltaic devices. Semiconductor/liquid junctions offer the opportunity to tune the electrical and chemical properties of the interface to produce either highly rectifying or ohmic contacts to a semiconductor of interest [89, 90, 91]. In aqueous solutions,

Cu_2O is only thermodynamically stable in a limited range of pH and electrochemical potential [92]. However, in acetonitrile [93] and other nonaqueous electrolytes [94, 95, 96], Cu_2O exhibits minimal photocorrosion.

The very low energy (3.2 eV versus vacuum) of the conduction-band edge of Cu_2O poses special challenges in forming high barrier-height contacts to this semiconductor [97]. Typically only very reactive metals would be expected to yield high barrier heights in p-Cu_2O/metal Schottky barriers, and these metals would only be useful if thermodynamically allowed interfacial chemical reactions, that produce species such as Cu metal, can be avoided during contact formation (figure 6.1 depicts an example of deleterious interfacial reactions with Cu_2O). Few heterojunction contacts have the needed low electron affinity to provide suitable band-edge offsets for junctions with Cu_2O. For example, the barrier height in Cu_2O/ZnO heterojunctions is only 0.75–0.87 V, due to the band edge misalignment [98]. High quality *p-n* Cu_2O homojunctions have not been reported due to the difficulty of preparing n-type Cu_2O.

For semiconductor/liquid contacts, redox species that have very negative Nernstian redox potentials should be required theoretically to produce p-Cu_2O/liquid junctions that provide high open-circuit photovoltages and thus high solar energy conversion efficiencies. The potentials of such species are far more negative than the reduction potential of water to produce H_2, and thus such redox species should be short-lived in aqueous solution. However, the use of one-electron, outer-sphere redox couples that have very negative reduction potentials, such as cobaltocenium/cobaltocene ($CoCp_2^{+/0}$) or decamethylcobaltocenium/decamethylcobaltocene ($Me_{10}CoCp_2^{+/0}$) in inert, nonaqueous solvents offers an opportunity explore the limits on open-circuit voltage that can be obtained by use of very high barrier height contacts to Cu_2O photocathodes. The performance of such systems can be used to establish the photovoltage and energy conversion properties of Cu_2O contacts that do not suffer from interfacial chemical reactions or interdiffusion processes that are typically present in Cu_2O-based solid-state devices.

6.2 High Purity Cu_2O Substrates

To investigate the fundamental material properties of Cu_2O, high purity Cu_2O substrates were prepared by the thermal oxidation of copper metal. The crystallographic and optoelectronic properties of the substrates were appropriate for testing solar energy conversion devices based on Cu_2O absorbers. The preparation and characterization of high purity Cu_2O substrates are described in the following sections.

6.2.1 Preparation of Cu_2O Substrates

Large-grain polycrystalline Cu_2O substrates were prepared by the thermal oxidation of 250 μm thick copper sheet (99.9999%) that was diced into 6×6 mm squares. The Cu samples were then suspended in a quartz tube and loaded into a tube furnace. Oxidation to Cu_2O was initiated by heating the tube furnace to 800 °C under $<5 \times 10^6$ Torr. The temperature was ramped to 980 °C under a rough vacuum of 1×10^3 Torr, and the Cu foil was then oxidized by exposure to oxygen (ultra high purity) at 6 Torr for 2 h. Following oxidation, the tube furnace was cooled stepwise to room temperature, under successively decreasing oxygen pressures, to maintain the Cu_2O phase according to the Cu–O phase diagram (figure 6.2) [99]. The oxidized Cu_2O foils were lapped using diamond abrasive films, and polished in a colloidal silica slurry (South Bay Technology), to produce substrates that had a specular finish and a thickness of 100–150 μm, as measured by digital calipers. The photograph in figure 6.3 shows a typical high purity Cu_2O substrate.

6.2.2 Characterization of Cu_2O Substrates

Scanning electron microscope (SEM) images as well as maps of the crystallographic orientation by electron backscatter diffraction (EBSD) were collected using a ZEISS 1550. The average grain size of an as-grown Cu_2O substrate was 275 ± 120 μm in diameter, as shown by SEM images (figure 6.3). Across large sample areas, no strong preferential crystallographic orientation was observed in the substrate, as shown by the corresponding false-color representation of the crystal planes acquired by EBSD

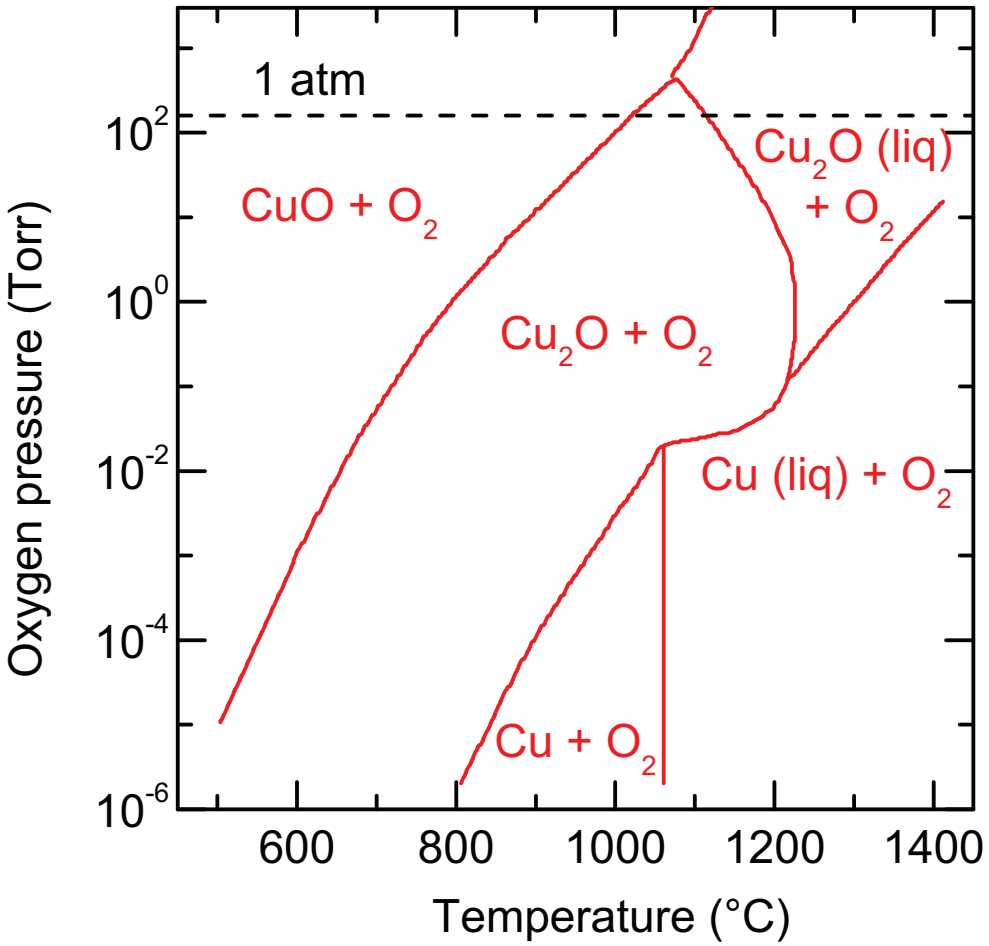

Figure 6.2. Phase diagram for Cu–O compounds as a function of temperature and oxygen pressure. Cu_2O is thermodynamically stable at room pressure at ∼1050 °C and under vacuum at reduced temperatures.

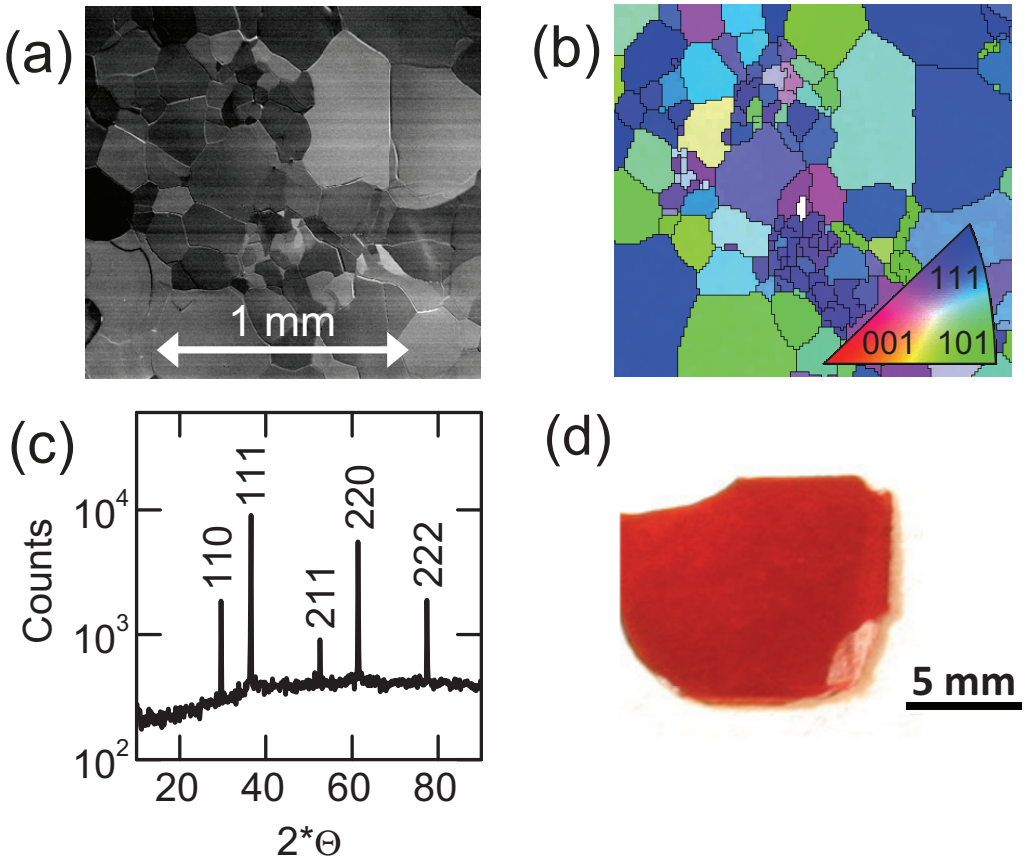

Figure 6.3. Crystallographic characterization of Cu_2O substrates. (a) Scanning electron microscope image showing the polycrystalline grain structure of the Cu_2O foil before lapping and polishing (scale bar, 1 mm). (b) Electron backscatter diffraction image showing the orientation map corresponding to the grain structure of the Cu_2O substrate. (c) X-ray diffraction measurement showing phase-pure Cu_2O. (d) Photograph of Cu_2O substrate.

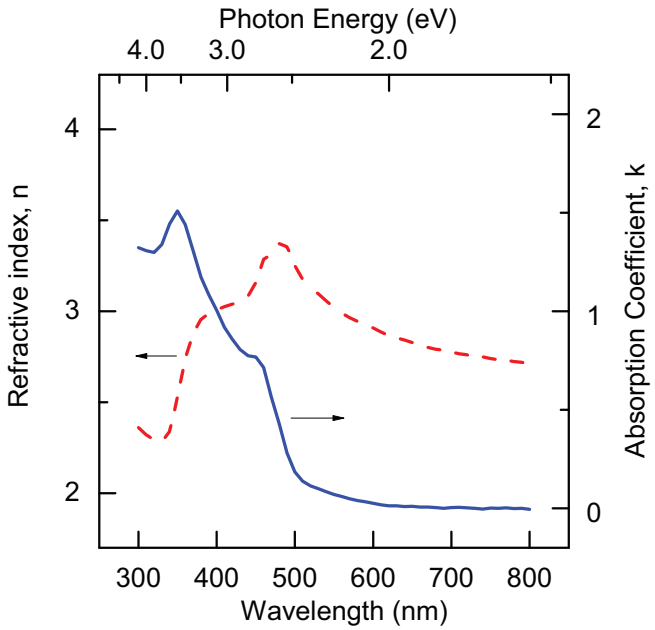

Figure 6.4. Real (red) and imaginary (blue) refractive indices of Cu_2O as a function of photon energy and optical wavelength.

(figure 6.3). X-ray diffraction (XRD) data were collected using a Philips XRD with Cu Kα radiation and all of the reflection peaks from the substrates were indexed to the Cu_2O cubic structure (figure 6.3). The SEM, EBSD, and XRD results thus indicated that the substrates synthesized by thermal oxidation consisted of large-grain polycrystalline Cu_2O.

Square Cu_2O substrates with evaporated gold contacts patterned at the four corners through a shadow mask were used for room temperature Van der Pauw and Hall effect measurements. As-grown polycrystalline Cu_2O substrates were found to be p-type with a hole concentration of 3.7×10^{13} cm^{-3} and a hole mobility of 65 cm$^2 \cdot$ V$^{-1} \cdot$ s^{-1}, which are comparable to literature values [81, 84]. Spectroscopic ellipsometry was performed at an angle of incidence of 50°, 60°, and 70°, for 300 nm $< \lambda <$ 850 nm, using a Xe lamp as the light source. The dielectric property $\Psi(\omega), \Delta(\omega)$ data were converted to n(ω), k(ω) values assuming a bulk, isotropic substrate. Cu_2O absorption data was consistent with the reported 2.0 eV band gap at room temperature.

6.3 Photoelectrochemical Measurements

The material properties of high purity Cu_2O electrodes were investigated by photoelectrochemical techniques (see appendix C) [100]. Ohmic contacts were made by evaporation of 100 nm of gold onto the unpolished side of the Cu_2O substrate. The Cu_2O substrates were then attached to copper wire by use of conductive silver paste between the wire and the gold film on the back of the Cu_2O. Exposed copper, silver, and gold surfaces were sealed to a supporting glass tube using epoxy (Hysol 1C), such that only the polished Cu_2O face was exposed to the electrolyte solution. The front surface of the photoelectrode was etched in 8 M HNO_3 (aq) for 1–2 s, rinsed with 18 MΩ resistivity water, and dried in a stream of N_2(g) [83, 84].

Figure 6.5a displays the *J*–*E* behavior of Cu_2O photocathodes in contact with either CH_3CN–1.0 M $LiClO_4$–0.020 M $CoCp^{2+}$–0.002 M $CoCp_2^0$ (red trace) or CH_3CN–1.0 M $LiClO_4$–0.020 M $Me_{10}CoCp_2^+$–0.002 M $Me_{10}CoCp_2^0$ (blue trace). Appendix C details the procedure for conducting photoelectrochemical measurements with a non-aqueous $CoCp^{+/0}$ redox couple. In contact with the $CoCp_2^{+/0}$ redox couple, Cu_2O photocathodes typically exhibited V_{oc} values of 500–550 mV. In contrast, in contact with the $Me_{10}CoCp_2^{+/0}$ redox couple, Cu_2O photocathodes exhibited V_{oc} values of 780–820 mV. In both cases, the Cu_2O photocathodes exhibited J_{sc} values between 3 and 4 $mA \cdot cm^{-2}$ and fill factors of 0.5–0.6.

In the dark and under forward bias, the stabilized electrodes passed only anodic current, as expected for a reversible photoelectrochemical system whose absolute anodic current was limited by the low concentration of the reduced species, either $CoCp_2^0$ or $Me_{10}CoCp_2^0$, respectively. In contrast to stabilized electrodes, freshly etched Cu_2O electrodes displayed V_{oc} values of >1 V under 1 sun of illumination, and V_{oc} = 0.3–0.4 V in the dark. The potential offset however was only observed prior to the first scan of the electrode. After passing a few $mC \cdot cm^{-2}$ of cathodic charge, the dark open-circuit voltage stabilized at 0.0 V, and the open-circuit voltage under 1 sun of illumination stabilized near 800 mV for Cu_2O/CH_3CN–$Me_{10}CoCp_2^{+/0}$ contacts and near 520 mV for Cu_2O/CH_3CN–$CoCp_2^{+/0}$ contacts during the entire

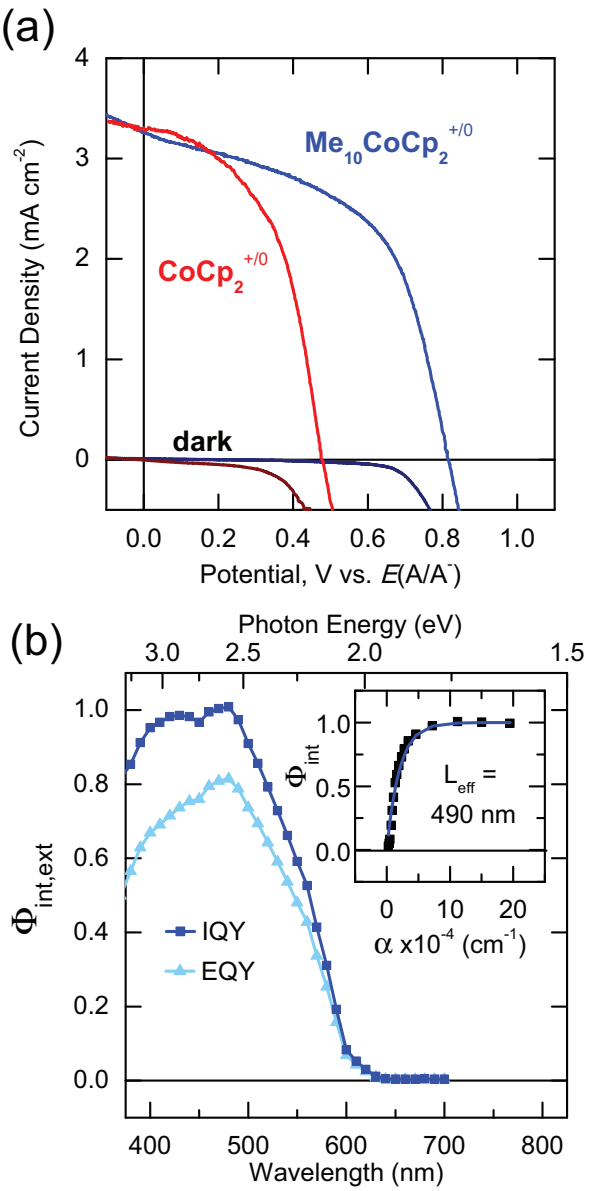

Figure 6.5. (a) J–E characteristics of Cu_2O photocathodes in the dark and under 1 sun simulated illumination in contact with CH_3CN–1.0 M $LiClO_4$ containing 0.020 M $Me_{10}CoCp_2^+$–0.002 M $Me_{10}CoCp_2$ (blue) or 0.020 M $CoCp_2^+$–0.002 M $CoCp_2$ (red). (b) Spectral response of Cu_2O photocathodes in CH_3CN–1.0 M $LiClO_4$–0.0020 M $Me_{10}CoCp_2^+$–0.0002 M $Me_{10}CoCp_2$, where the internal quantum yield is derived from the external quantum yield using solution optical absorption and reflection losses.

course of the experiments (a few h).

Figure 6.5b shows the external quantum yield (Φ_{ext} or EQY, light blue triangles) and the estimated internal quantum yield (Φ_{int} or IQY, dark blue squares) of Cu_2O photocathodes in contact with CH_3CN–$Me_{10}CoCp_2^{+/0}$. The external quantum yield peaked at 0.8 near 500 nm, with significant losses in both the blue and red spectral regions. Reflection losses were estimated using the Fresnel equations with the refractive indices of glass, CH_3CN, and Cu_2O in the spectral range of interest. The internal quantum yield, corrected for solution optical absorption and reflection losses, showed carrier collection approaching unity in the 400–500 nm spectral range. The solution absorption of diluted electrolyte was measured using a UV-Vis spectrometer and is shown in figure 6.6. The effective collection length, L_{eff}, was determined to be 490 nm by fitting the spectral response data to

$$\Phi(\lambda)_{int} = \frac{\int_0^{L_{eff}} q\Gamma_0\alpha(\lambda)e^{-\alpha(\lambda)x}dx}{q\Gamma_0} = 1 - e^{-\alpha(\lambda)L_{eff}} \quad , \tag{6.1}$$

where $q\Gamma_0\alpha(\lambda)e^{-\alpha(\lambda)x}$ is the electron-hole generation rate, Γ_0 is the incident photon flux per unit area and $\alpha(\lambda)$ is the absorption coefficient of Cu_2O substrates at each wavelength [72].

Figure 6.7a shows the effects of illumination intensity on the current density–voltage characteristics of Cu_2O/CH_3CN–$Me_{10}CoCp_2^{+/0}$ contacts. The maximum illumination intensity from the W-halogen ELH-type illumination corresponded to 100 $\text{mW} \cdot \text{cm}^{-2}$, i.e. 1 sun, whereas a series of neutral density filters was used to attenuate the light intensity to $\sim$2.3 $\text{mW} \cdot \text{cm}^{-2}$. Figure 6.7b shows the integrated external quantum yield as a function of the applied potential, where the integrated external quantum yield is the fraction of the observed photocurrent density relative to the estimated total photon flux at all energies above the Cu_2O band gap. The discrepancy between the absolute value of the integrated external quantum yield and the spectral response data shown in figure 6.5b is attributable to solution absorption. The integrated external quantum yield at J_{sc} increased as the light intensity decreased. The increase in Φ_{ext} is attributable to the decreased concentration of the

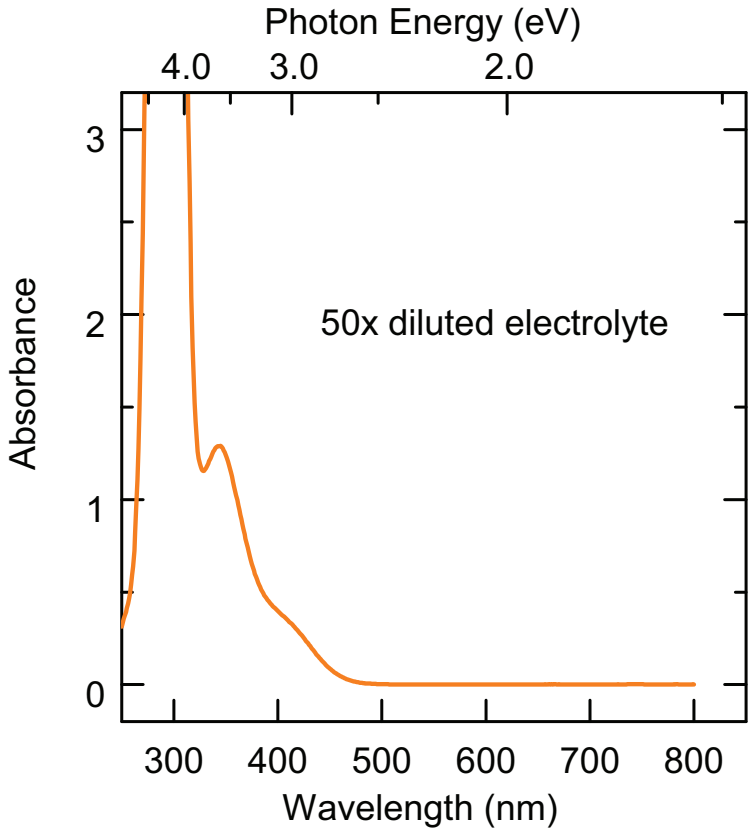

Figure 6.6. Optical absorbance of the electrolyte used for photoelectrochemical measurements diluted to a composition of approximately CH_3CN–20 mM $LiClO_4$ containing 0.40 mM $Me_{10}CoCp_2^+$–0.04 mM $Me_{10}CoCp_2$.

highly absorbing $Me_{10}CoCp_2{}^0$ species that is generated near the electrode surface at low cathodic current densities.

The V_{oc} of a semiconductor/liquid junction is given by equation (6.2) [40], where n is the diode quality factor, k_B is the Boltzmann constant, T is the temperature (in K), q is the charge on an electron, J_{ph} is the photocurrent density, and J_0 is the exchange current density:

$$V_{oc} = \frac{nk_BT}{q}\ln\left(\frac{J_{ph}}{J_0}\right) \quad . \tag{6.2}$$

For a photoconductor, J_0 is expected to be inversely proportional to the hole concentration (N_A) under illumination. The hole concentration (N_A) for Cu_2O photoelectrodes as a function of light intensity was computed from the cell series resistance that was estimated by fitting the slope of the J–E data in the region of V_{oc} (figure 6.7a inset). The deduced hole concentration showed a linear relationship on light intensity, consistent with other reports of photoconductivity in Cu_2O [101, 102]. At illumination intensities near 1 sun, a diode ideality factor of approximately 2.1 (figure 6.7b, inset) was obtained from the slope of V_{oc} versus J_{sc} by equation (6.2). The error bars in the inset represent the standard deviation from four samples that were analyzed under a series of illumination intensities.

6.4 Stability of Cu_2O Photoelectrodes

Figure 6.8a displays J–E data for freshly etched Cu_2O electrodes in contact with the aqueous methyl viologen ($MV^{2+/+}$) redox couple (purple), as well as the J–E behavior of $Cu_2O/Me_{10}CoCp_2{}^{+/0}$ contacts before (blue) and after (orange) photoelectrochemical measurements of $Cu_2O/MV^{2+/+}$ (aq) contacts. Appendix C details the procedure for conducting photoelectrochemical measurements with a $MV^{2+/+}$ redox couple. The J–E data of the $Cu_2O/MV^{2+/+}$ (aq) contacts exhibited $V_{\rm oc} < 200$ mV. Moreover, after the measurements visible Cu precipitation was observed at the electrode surface, consistent with significant photocorrosion. Freshly etched Cu_2O electrodes demonstrated $V_{\rm oc}$ ~800 mV in contact with CH_3CN–$Me_{10}CoCp_2{}^{+/0}$ electrolytes, but elec-

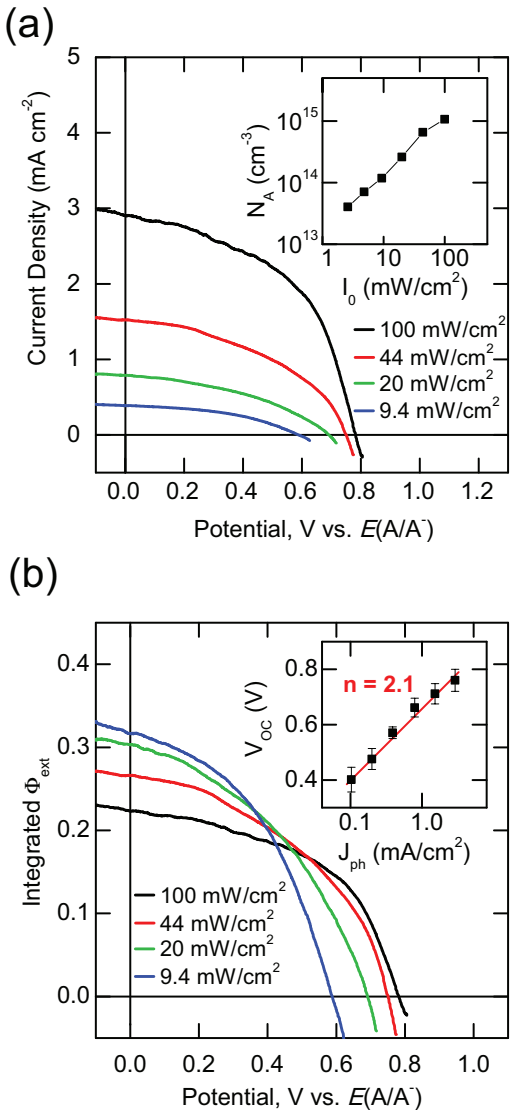

Figure 6.7. (a) J–E characteristics and (b) external quantum yield, Φ_{ext}, as a function of illumination intensity for Cu_2O photocathodes in contact with CH_3CN–1.0 M $LiClO_4$–0.020 M $Me_{10}CoCp_2^+$–0.002 M $Me_{10}CoCp_2$. The external quantum yield was calculated using the theoretical maximum current density for the illumination intensity. (b, inset) Linear fits to V_{oc} as a function of illumination intensity using the ideal diode equation to give estimates of the diode ideality factor, n.

trodes that had first been exposed to $MV^{2+/+}$ (aq) electrochemical scans exhibited $V_{oc} < 300$ mV in contact with $Me_{10}CoCp_2^{+/0}$. The degradation of the photoelectrochemical performance caused by photocorrosion of Cu_2O in aqueous methyl viologen experiments was however reversed by etching the Cu_2O electrodes in concentrated HNO_3 (aq).

X-ray photoelectron spectroscopy (XPS) and X-ray excited Auger electron spectroscopy (XAES, or AES) data were obtained at base pressures $<1 \times 10^{-9}$ Torr using an M-Probe spectrometer. A monochromated Al Kα x-ray source generated a 300 μm spot size and high-resolution spectra were acquired with a 100 mm hemispherical electron analyzer with a pass energy of 20 eV. The Cu_2O samples were freshly prepared and immediately loaded into the spectrometer. In addition to freshly prepared Cu_2O samples, XP and Auger spectra were also acquired on Cu_2O substrates that had been used as electrodes in photoelectrochemical cells. In all cases, spectra were fit with Gaussian–Lorentzian lineshapes above a Shirley baseline.

In Cu $2p_{3/2}$ photoelectron spectra, metallic Cu^0 exhibits a peak centered at 932.6 eV, whereas Cu_2O shows a peak at 932.4 eV and CuO shows a primary photoelectron peak at 933.6 eV and secondary shake-up peaks at 940–945 eV [103]. Hence, the Cu $2p_{3/2}$ spectral region can be used to unambiguously identify the presence of CuO surface species, but cannot be used to distinguish between Cu_2O and metallic Cu^0 surface species. In contrast, metallic Cu^0 produces a peak centered at 918.5 eV in the Cu LMM Auger electron region, whereas Cu_2O exhibits a signal at 916.8 eV, and CuO shows a signal at 917.8 eV [103, 104, 105, 106]. The kinetic energies observed in the Cu LMM Auger region can thus discriminate between Cu_2O and metallic Cu^0 surface species.

Figure 6.8b depicts the spectra from the Cu $2p_{3/2}$ photoelectron and Cu LMM Auger electron regions observed for Cu_2O substrates that were either freshly etched (i), used as photoelectrodes in contact with CH_3CN–$Me_{10}CoCp_2^{+/0}$ (ii), or used as photoelectrodes in contact with $MV^{2+/+}$ (aq) (iii). Although all of the XP spectra were well fit with two peaks, additional peaks at both high- and low-binding energy were needed to effectively fit the Auger spectra [103]. Dashed lines have been included

in the Auger spectra at 916.8 eV, indicative of the Cu_2O species, and at 918.5 eV, indicative of metallic Cu^0. Dashed lines have been included in the XP spectra at 934.4 eV, indicative of CuO species, and at 932.1 eV, indicative of either Cu_2O or metallic Cu^0.

As shown in part (i) of figure 6.8b, the Cu $2p_{3/2}$ spectral region of the freshly etched Cu_2O surface showed a large peak at 932.1 eV and a smaller feature centered at 934.3 eV, indicating that little CuO or surface hydroxide was present on the surface of the sample. Furthermore, the Cu LMM Auger peak at 917.1 eV, and the absence of any significant feature at 918.5 eV, indicated that the thermal oxidation of Cu foil to Cu_2O, and subsequent etching with HNO_3 (aq), produced a Cu_2O surface that was free of metallic Cu^0. The Auger spectrum in part (i) and all further Auger spectra show features attributed to an additional peak towards the lower binding energy at ≈912.5 eV and a further peak towards the higher binding energy at ≈921.0 eV. Figure 6.8b, part(ii) demonstrates that the surface composition was essentially unchanged after photoelectrochemical experiments in contact with CH_3CN–$Me_{10}CoCp_2^{+/0}$. This result is consistent with the expected stability of Cu_2O in nonaqueous photoelectrochemical cells.

In contrast, use of the Cu_2O in contact with $MV^{2+/+}$ (aq) yielded significant changes in the XP and Auger spectra, as shown in figure 6.8b, part (iii). In particular, the strongest feature in the Cu LMM Auger spectrum shifted from 917.1 to 916.4 eV, and an additional feature appeared at 918.5 eV, denoted by the bold, green fitted trace, which is ascribable to metallic Cu^0. The Auger spectrum of figure 6.8b part (iii) corroborates the results described above, in which interfacial metallic Cu^0 formed by aqueous photocorrosion processes significantly degraded the photoelectrochemical performance of the Cu_2O/CH_3CN–$Me_{10}CoCp_2^{+/0}$ contact.

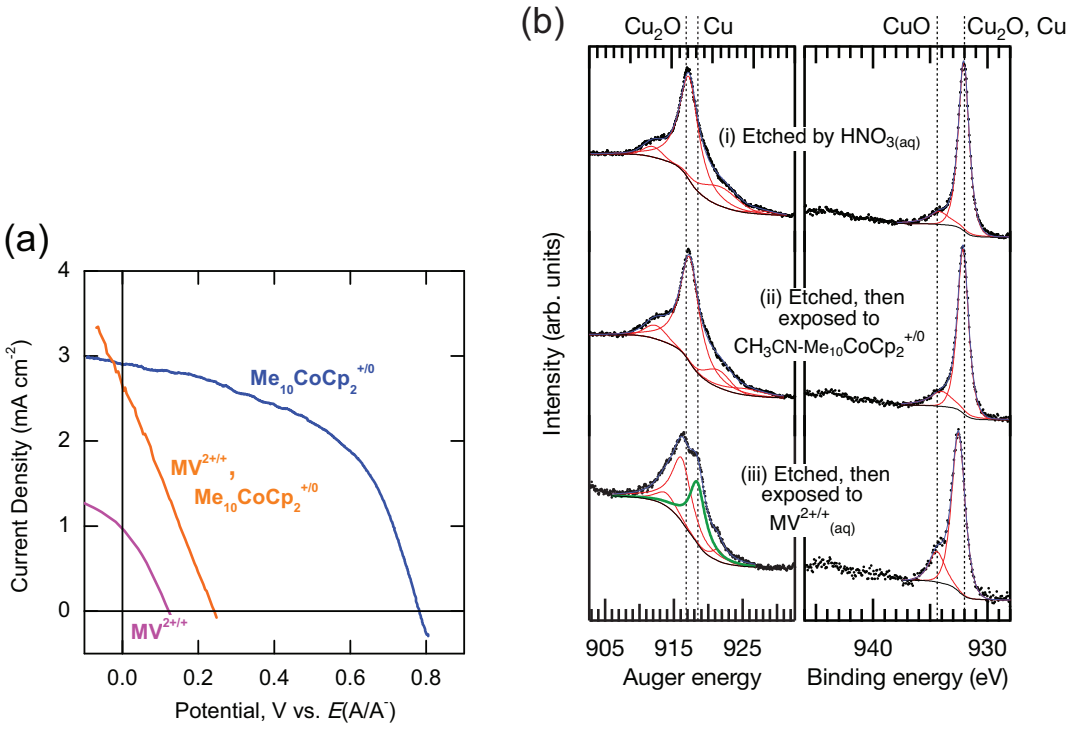

Figure 6.8. (a) Current density–potential characteristics under ELH-simulated 1 sun illumination of freshly etched Cu_2O photocathodes in contact with CH_3CN–1.0 M $LiClO_4$–0.020 M $Me_{10}CoCp_2^+$–0.002 M $Me_{10}CoCp_2$ (blue); etched, exposed to H_2O–0.5 K_2SO_4–0.050 M MV^{2+} (aq) and then in contact with CH_3CN–1.0 M $LiClO_4$–0.020 M $Me_{10}CoCp_2^+$–0.002 M $Me_{10}CoCp_2$ (orange); etched Cu_2O photocathodes in contact with H_2O–0.5 K_2SO_4–0.050 M MV^{2+} (aq) (purple). (b) Cu LMM Auger electron spectra (left) and Cu $2p_{3/2}$ XP spectra (right) for chemically treated Cu_2O: (i) etched by aqueous HNO_3; (ii) etched then exposed to CH_3CN–$Me_{10}CoCp_2^{+/0}$; (iii) etched then exposed to H_2O–0.5 K_2SO_4–0.050 M MV^{2+} (aq).

6.5 Conclusions

6.5.1 Open-Circuit Voltage of Cu_2O/CH_3CN Junctions

The behavior of the semiconductor/liquid contacts investigated here reflect the photogeneration, transport, and recombination processes in the Cu_2O, in which the redox system in the liquid only served to transport the charge across the interface and to determine the equilibrium barrier height of the solid/liquid contact. The resulting energy conversion properties of such systems are thus directly analogous to those displayed by Cu_2O heterojunctions or homojunctions. The 820 mV open-circuit voltage of Cu_2O/CH_3CN–$Me_{10}CoCp_2^{+/0}$ contacts is significantly higher than the reported V_{oc} values of 680 [88], 595 [84], and 300 mV for Cu_2O/ZnO [85, 86], 400 mV for Cu_2O/CdO [83, 87] and Cu_2O/Al-doped ZnO [107], 270 mV for Cu_2O/ITO [108], 240 mV for Cu_2O/Cu_xS [109], or <430 mV for *p*-*n* Cu_2O junctions [110, 111], and <400 mV for previous Cu_2O/liquid junctions [93, 112]. The 3.2 eV electron affinity of Cu_2O constrains the choices of redox couples appropriate for semiconductor/liquid junctions, because a very negative reduction potential is required to minimize the discontinuity between the Cu_2O conduction band edge and the solution reduction potential. For instance, the $CoCp_2^{+/0}$ standard reduction potential at –0.91 V versus SCE and the $Me_{10}CoCp_2^{+/0}$ standard reduction potential at –1.47 V versus SCE are close to the potential of the Cu_2O conduction band edge at –1.6 V versus SCE [97, 113]. The difference between the V_{oc} values in Cu_2O/CH_3CN–$Me_{10}CoCp_2^{+/0}$ contacts and Cu_2O/CH_3CN–$CoCp_2^{+/0}$ contacts is primarily due to the different standard reduction potentials of the two redox couples [100].

The observed open-circuit voltage is nonetheless lower than the V_{oc} expected from the bulk recombination limit for Cu_2O. The maximum theoretical V_{oc} of a semiconductor junction is determined by the bulk electronic properties of the semiconductor as described by equation (6.3): [40, 72, 114]

$$V_{oc} \approxeq \frac{kT}{q} \ln\left(\frac{J_{ph} L_n N_A}{q D_n n_i^2}\right) \quad , \tag{6.3}$$

Table 6.1. Analysis of photocurrent density for Cu_2O substrates, where J_{sc}^{MAX} corresponds to the theoretical maximum photocurrent density given the 2.0 eV band gap of Cu_2O and the spectrum of the incident light; J_{sc}^{IQY} corresponds to the expected photocurrent density given the reduced red response due to internal collection losses; J_{sc}^{PEC} corresponds to the expected photocurrent density given the estimated internal quantum yield, solution absorption and reflection losses; and J_{sc}^{exp} is the observed photocurrent density under ELH illumination

Light source	J_{sc}^{MAX} ($mA \cdot cm^{-2}$)	J_{sc}^{IQY} ($mA \cdot cm^{-2}$)	J_{sc}^{PEC} ($mA \cdot cm^{-2}$)	J_{sc}^{exp} ($mA \cdot cm^{-2}$)
AM 1.5	14.1	9.0	5.0	n/a
100 $mW \cdot cm^{-2}$	13.8	7.2	4.7	3.3
10 $mW \cdot cm^{-2}$	1.4	0.68	0.44	0.41

where L_n is the minority-carrier (electron) diffusion length, N_A is the concentration of acceptors, n_i is the intrinsic carrier density, D_n is the minority carrier diffusion coefficient (estimated by using $D_n = \left(\frac{m_h}{m_e}\mu_h\right)\frac{kT}{q}$, where μ_h is the hole mobility, and $\frac{m_h}{m_e} \approx 0.58$ is the effective mass ratio between the hole and the electron) [115, 116, 117]. Using $N_A = 3.7 \times 10^{13}$ cm^{-3}, $D_n = 2.2$ $cm^2 \cdot s^{-1}$, $n_i = 2 \times 10^2$ cm^{-3}, and estimating L_n to be 100 nm to 10 μm, yields a value of 1.20–1.32 V as the maximum theoretical V_{oc} for Cu_2O photocathodes. Achieving the maximum theoretical V_{oc} will require the use of the redox couple with a more negative potential and the passivation of Cu_2O surface states.

6.5.2 Short-Circuit Current Density of Cu_2O/CH_3CN Junctions

The low observed J_{sc} values for Cu_2O photocathodes in contact with CH_3CN–$Me_{10}CoCp_2^{+/0}$ solutions can be quantitatively attributed to incomplete collection

due to bulk recombination in the semiconductor and to incomplete absorption due to solution optical absorption and reflection losses. Table 6.1 shows the estimated J_{sc} values expected for Cu_2O photocathodes under AM 1.5 illumination, under ELH-simulated 1.0 sun of illumination, and under attenuated ELH-simulated 0.09 sun of illumination, given the various expected loss mechanisms. J_{sc}^{MAX} represents the theoretical maximum photocurrent density given the photon flux of the incident light that is above the 2.0 eV band gap of Cu_2O, using standard spectral data. J_{sc}^{IQY} refers to the expected photocurrent density, given the spectrum of the incident light and the energy dependence of the internal quantum yield. J_{sc}^{PEC} refers to the expected photocurrent density given the measured solution absorption and estimated reflection losses inherent in the photoelectrochemical cell in addition to internal collection losses. At ELH-simulated 1.0 sun illumination, the value J_{sc}^{exp} is expected to be even less than J_{sc}^{PEC}, due to additional solution absorption caused by $Me_{10}CoCp_2{}^0$ that is generated at the electrode surface under short-circuit conditions. However, at the attenuated ELH-simulated 0.09 sun illumination, the values of J_{sc}^{exp} and J_{sc}^{PEC} are in agreement, because the photogenerated $Me_{10}CoCp_2{}^0$ is produced at a lower rate and can be removed by stirring. Routes to improving the photocurrent of the Cu_2O photocathodes in contact with a nonaqueous $Me_{10}CoCp_2{}^{+/0}$ solution include producing material with longer diffusion lengths and better red response, as well as utilizing a thin-layer photoelectrochemical cell with minimized solution absorption [118].

Appendix A

Detailed Synthesis Procedures

This section contains detailed procedures for processing high purity Zn_3P_2 substrates with controlled p-type doping from elemental zinc and phosphorus starting materials [24].

A.1 Quartzware Preparation

For high temperature work and to reduce contamination, quartz glassware is required for the synthesis. Standard borosilicate glassware cannot withstand the high temperatures or pressures during the synthesis of Zn_3P_2. Even for lower temperature procedures such as substrate doping, quartz is still preferred for its high purity SiO_2 composition. The most easily obtained quartz is a natural mineral that is refined and sold as "fused quartz" or quartz grade GE 214. Quartz grade indentifies the impurity concentrations in the material, and table A.1 shows the impurity level in parts per million (ppm) for the most common grades available. The supplier that has given consistently quality material has been GM Associates in Oakland, CA (http://www.gmassoc.com).

Several particular sizes of quartz ampoules are used in the procedures to prepare high purity Zn_3P_2 substrates. The smallest ampoules use 14×16 mm outer tubes with 11×13 mm plugs. These are used for ≈4 g scale Zn_3P_2 synthesis, single ampoule crystal growth, and doping experiments. The medium size ampoules use 22×25 mm outer tubes with 18×21.6 mm plugs. These are used for ≈8 g scale Zn_3P_2 synthesis, ≈24 g purification, and housing the nested ampoule crystal growth. The largest ampoules use 46×50 mm (or 47×50 mm) outer tubes with 42×45 mm (or 42×46 mm)

Table A.1. Impurity concentrations for quartz of different material quality in ppm for the most common purities where fused quartz (GE 214) is appropriate for most applications, and synthetic quartz or silica (GE 095) is of extremely high purity but is expensive and difficult to obtain

Type	Al	Ca	Fe	K	Li	Na	Ti	Zr	OH
GE 214	14	0.4	0.2	0.6	0.6	0.7	1.1	0.8	<5
GE 095	11	<0.05	0.08	<0.05	<0.05	<0.05	<0.02	<0.02	<4
GE 124	14	0.4	0.2	0.6	0.6	0.7	1.1	0.8	<5
GE 144	8	0.6	0.2	<0.2	<0.2	<0.2	1.4	0.3	<5
GE 219	14	0.4	0.2	0.6	0.6	0.7	100	0.8	<5
GE 224	14	0.4	0.2	<0.2	<0.05	<0.1	1.1	0.8	10

plugs. These are used for ≈24 g Zn_3P_2 synthesis and up to ≈80 g purification.

To prepare the outer tubes, 24” lengths of quartz are flame-cut to yield two 12” tubes with closed ends. For the plug tubes, 6”–8” pieces of quartz are flame-cut to yield two 3”–4” tubes with closed ends. Flame polishing of the rounded ends is necessary to improve its mechanical strength. Hydrogen–oxygen flames are preferred for quartz-working, but methane–oxygen flames are sufficient for the smaller tube size. The 50 mm ampoules require a glassblowing lathe to flame cut and should be left for a professional glassblower. After the tubes are cut, they are etched 1–2 h in a KOH–isopropanol base bath, thoroughly rinsed, and dried in an oven.

Before use in Zn_3P_2 synthesis, the inside of the outer tube for the ampoule is carbon coated. Carbon coating greatly reduces the adhesion of Zn_3P_2 to the quartz ampoule and enables greatly improved growth quality. In practice the location of the carbon is not critical to fulfilling its role of reducing adhesion. Even a carbon powder placed in the opposite end of the tube from the growing Zn_3P_2 material is effective for reducing adhesion. For this reason it is likely that the main role of the carbon is to act as a getter for water and SiO rather than a physical barrier between the Zn_3P_2 and the SiO_2. The carbon-coating apparatus in figure A.1 uses HPLC purity n-hexanes

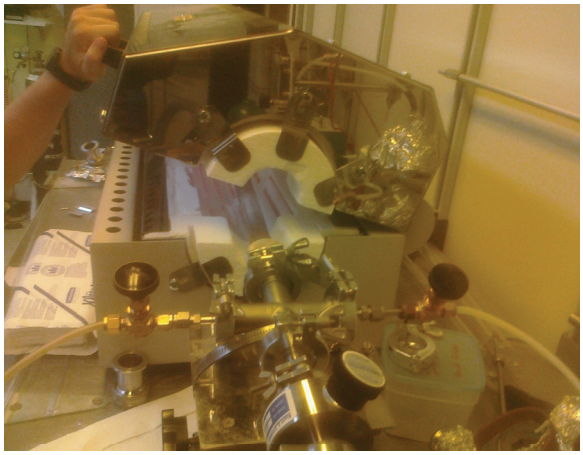

Figure A.1. Photograph of tube furnace for carbon coating ampoules. HPLC purity n-hexanes is delivered through the inlet valve (right) by Ar(g) to the ampoule at ∼750 °C in the furnace such that the n-hexanes decomposes to amorphous black carbon on the walls of the ampoule (center, back). The exhaust valve (left) allows the apparatus to purge, and the roughing valve (center, forward) enables vacuum annealing of the amorphous carbon coatings.

for the carbon source and Ar as the carrier gas. The outer tube is first pumped to <10 mTorr and then purged with Ar(g) while the furnace ramps to 750 °C. Once the furnace is at temperature, the Ar(g) is bubbled through n-hexanes and allowed to diffuse into the end of the outer tube in the furnace for 30–45 min or until an opaque black coating of amorphous carbon is formed. Then the gas flow is switched to Ar(g) to purge the apparatus and the furnace is raised to 1000 °C for 1 h. Once extracted from the furnace, the carbon coating should be shaped by burning the carbon in air with a torch so that only a few inches of black coating remain.

A.2 High Purity Zn_3P_2 Preparation

For preparing the sealed ampoule, the carbon-coated outer tube and the plug are loaded with the appropriate material. Using a KF flange to quick connect coupling adapter, the outer tube is evacuated to high vacuum and sealed under active pumping with a methane–oxygen torch. Great care must be taken for the initial evacuation to

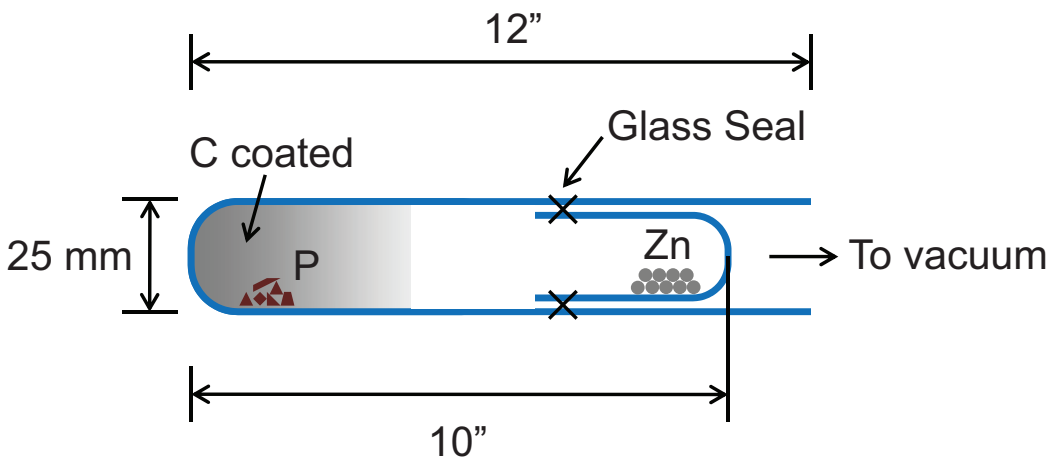

Figure A.2. Diagram of Zn_3P_2 synthesis ampoule showing the carbon-coated outer quartz tube loaded with red phosphorus chips and the plug loaded with zinc shot. The glass seal is a ring that melts the outer tube to the plug and is made with a hand-held methane-oxygen torch.

ensure that the components do not shift and for the ampoule sealing to ensure that the components do not escape during the reaction.

For synthesizing Zn_3P_2 from elemental zinc and phosphorus, the stoichiometric amount of phosphorus is loaded on the carbon-coated side and the corresponding zinc into the quartz plug. High purity >99.9999% zinc shot and red phosphorus lump can be purchased from Alfa Aesar, with the proper authorization for red phosphorus as it is restricted by the Drug Enforcement Administration (DEA). The sealed ampoule is loaded into a three zone furnace such that each end is centered on a separate zone. Figure A.2 shows a schematic of a Zn_3P_2 synthesis ampoule with dimensions. First the phosphorus end is heated to 550 °C for 1 h to convert the red phosphorus into white phosphorus. Then the zinc end is heated to 850 °C for about 16–24 h until complete reaction of the elements to Zn_3P_2. The resulting Zn_3P_2 material forms a large-grain polycrystalline pellet at the cold end of the reaction ampoule that is extracted by breaking open the (disposable) ampoule.

At least one purification step is performed with the raw Zn_3P_2 material. For the purification, Zn_3P_2 powder that has been ground in a mortar and pestle (mortar

and pestle are cleaned before and after with aqua regia) is added to the plug tube of a carbon coated ampoule. Then the sealed ampoule is loaded into a three-zone furnace, and the plug end is raised to 850 °C. During the next 50–100 h, the entire Zn_3P_2 source material sublimes to the cold end of the ampoule. Some residue of black carbon, black phosphorus, zinc oxides and glass is typically left in the plug end after the purification. Often the purification ampoule cracks upon cooling as the carbon coating does not completely prevent adhesion between the ampoule walls and the growing Zn_3P_2. Pulling the ampoule from the furnace and allowing it to cool quickly minimizes the loss of purified Zn_3P_2 for ampoules that crack upon cooling.

The Zn_3P_2 material formed during purification accumulates as a dense coating on the cold end of the tube. For long purification times, high purity Zn_3P_2 substrates have been cut from the dense coating and used for characterization experiments and device fabrication. The purified Zn_3P_2 has also been used as the source material for congruent sublimation of thin films.

A.3 Polycrystalline Boule Preparation

Two strategies for crystal growth are outlined here: the single ampoule technique and the nested ampoule technique.

The single ampoule technique uses a quartz rod joined to the outer quartz tube such that the tube reaches a point at the tube-rod junction. The quartz tube-rod junctions provide a nucleation zone for the growing Zn_3P_2 crystal and help increase the size of the grains. The outer tube is coated with carbon, loaded with Zn_3P_2, and sealed with a quartz plug under active vacuum. The single ampoule technique takes 1–2 months to grow a full boule, but yields 20–30 substrates when completed.

The nested ampoule technique is both more complicated to fabricate for the glass-blower and also more difficult to seal. When fabricated as per the schematic in figure A.3, the quartz piece can be loaded with the source Zn_3P_2 material and placed inside a carbon-coated outer tube followed by a standard plug tube for the outer tube. A glass seal is made around the loading opening of the inner ampoule to make the

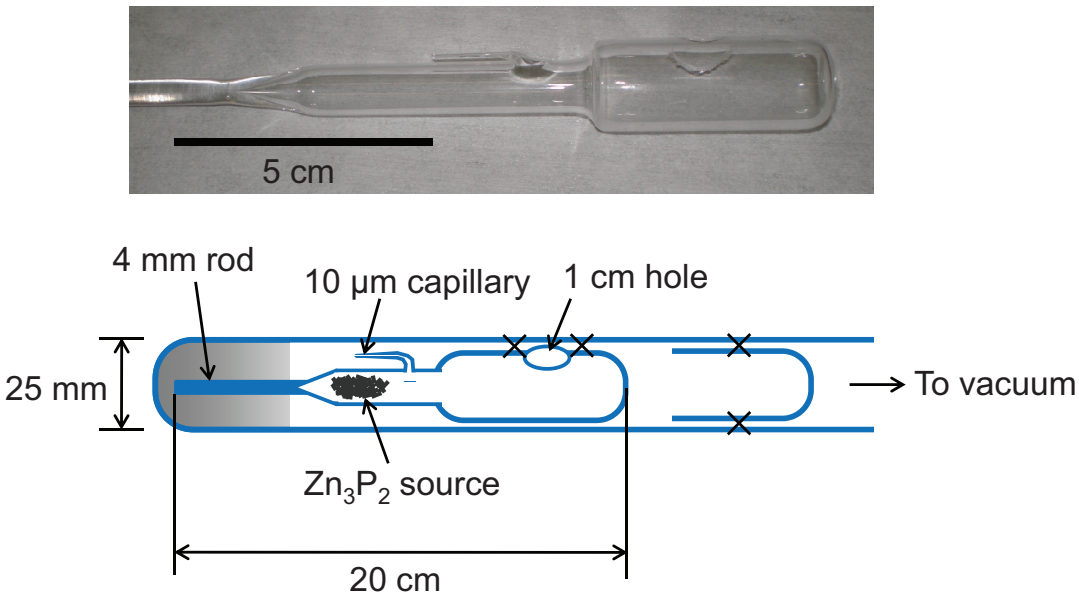

Figure A.3. Diagram of Zn_3P_2 crystal growth ampoule showing the carbon-coated outer quartz tube and the nested ampoule for crystal growth loaded with Zn_3P_2 source material. The quartz tube tapers to a point at the junction with the quartz rod to provide a nucleation zone. The first glass seal is a ring around the hole used to load Zn_3P_2 into the nested ampoule and the second glass seal is a ring that melts the outer tube to the plug. Be sure to slide the Zn_3P_2 source material away from the nucleation zone of the inner ampoule before growth.

capillary the only path for vapor transport between the outer and inner compartments of the nested ampoule. Finally the outer tube is sealed to bring the nested ampoule under passive vacuum. The advantage, however, of the nested ampoule technique is its ability to grow large-grain polycrystalline boules in 1–2 weeks or less. Some material is lost during growth through the capillary, resulting in yields of 15–20 substrates when completed.

The finished ampoule of either technique is loaded into the crystal growth furnace, and then the furnace is then ramped to 850 °C and aligned with a programmable stepper motor. The stepper motor uses a 9-pin serial connection that is adapted to a USB port and interfaced using the "IMS_term_NT.exe" program. Short segments of code are written and uploaded into the memory of the stepper motor. The program

is loaded into the stepper motor controller by opening a communication console in "IMS_term_NT.exe" and entering the code with a carriage return after each line. The following sample program moves the stepper motor about 1 $mm \cdot h^{-1}$:

```
P
+33
W 30000
G 0 250
G 0 250
P
```

The command "P" begins or ends a program; "+33" moves the stepper motor forward 33 steps, where 400 steps is 1 mm and a full revolution; "W 30000" waits 300 s; "G 0 250" is a loop command that goes to the first line (line 0) 250 times. The two loop commands create an infinite loop because the stepper motor controller has only one loop constant register. The wait command accepts a number between 0 and 32767 and the loop command accepts a repetition counter between 1 and 255. Loops commands with low repetition counters such as "G 0 2" may result in unstable wait times after several days. Constant growth rates of 0.5–1.0 $mm \cdot h^{-1}$ for the single ampoule technique and 3 $mm \cdot h^{-1}$ for the nested ampoule technique are appropriate for a 24" single zone furnace. When the growth is complete, the crystal is extracted by breaking open the intricate but disposable quartz pieces.

A.4 Substrate Preparation

The large-grain polycrystalline boule is diced using a low-speed diamond saw. Low concentration 4" diamond blades are effective for dicing Zn_3P_2 wafers of approximately 600–700 μm thickness, although wire saws could be used to cut thinner wafers. If too much force is applied to the crystal, the blade spins too fast, or if high concentration diamond is used, the boule is likely to fracture during dicing and not yield full 1 cm diameter wafers.

Zn_3P_2 substrates without intentional doping exhibit p-type intrinsic doping in a wide range from 10^{13} to 10^{16} holes $\cdot$ cm^{-3}. Annealing with P_4 vapor is effective for bringing intrinsic wafers to a p-type doping level of $\sim 5 \times 10^{16}$ holes $\cdot$ cm^{-3}. The rough wafers are etched in 2% Br_2 in methanol for 30 s, and then metallized with 10–60 nm of Ag metal if doping of $>10^{17}$ holes $\cdot$ cm^{-3} is desired. The rough wafers are loaded into a 14×16 mm quartz tube and 15–20 mg red phosphorus are loaded the 11×13 mm quartz plug. The ampoule is sealed under active vacuum and the plug end is heated to 550 °C to convert the red phosphorous to white phosphorus. When transparent droplets of white phosphorus condense on the cold end, the furnace is cooled to 400–450 °C and the ampoule is positioned in the center of the furnace for 20 h. Opening the doping ampoule requires caution because the remaining white phosphorus is highly reactive in air. The safest approach is to position the doping ampoule with only the end with the wafers in the furnace (at 100 °C) to transport the P_4 away from the wafers. Then the plug end is broken off and the phosphorus is allowed to oxidize in a fume hood away from the doped wafers.

Lapping and polishing is performed after the doping process because high temperature treatments damage the specular finish of the substrates. Although many methods have been attempted for preparing specular Zn_3P_2 substrates, the following method is the most consistent and straightforward. Both sides of the wafer are lapped with 20 μm alumina abrasive film to make the two sides parallel and planarized. The wafer is then lapped until its thickness is about 50 μm greater than the desired final thickness. Next, diamond abrasive filmes of 9, 6, 3, and 1 μm grit sizes are used to lap the wafer for about 60–180 s with each grit size to sequentially reduce the feature size of the polishing damage to the surface. The surface should be specular and almost featureless to the unaided eye, but streaks should still be visible by optical miscroscopy. Final polishing with 0.25 μm diamond paste further reduces the visible surface damage.

Immediately before using the substrate for characterization experiments or device fabrication, a final chemical etch in 2% Br_2 in methanol for 30 s (etch rate $\sim$30 nm $\cdot$ s^{-1}) is necessary to remove native oxidation and subsurface polishing damage. The solu-

tion changes over time due to Br_2 evaporation and reaction between Br_2 and methanol, so fresh 2% Br_2 in methanol solutions must always be used. The substrate is degreased in methanol, stirred in 2% Br_2 in methanol for 30 s with plastic or ceramic tweezers, quenched by immersion in clean methanol, and dried with a stream of inert gas.

Appendix B

Simulation of Time-Resolved Photoluminescence

This is the MATLAB code used to prepare simulated time-resolved photoluminescence decay traces [53, 54, 119].

```
function [tspan,xspan,n,ntintc] = PLsolverHL(tspan,mun,tn,Sn, PLOT)
close all; clear all; clc
%
% load raw TRPL data file
load PLdata3;
m=0;
PLOT=1;
%
% pulse characteristics
pw = 80e-12; % pulse width
pt = 4.2e-9; % pulse begins at t=pt
pulse = 1e-6; % energy per pulse (J)
lambda = 355e-7; % excitation wavelength (m)
E=h*c/lambda;
Np = pulse/E/0.01; % photons/cm2
%
% detector characteristics
dw = 250e-12; %binning width of detector
```

```
%
% Fundamental constants
k = 8.61734315e-5; % eV/K
T = 295; % K
q = 1; % C
c=29979245800; %m/s
h=6.6260689633e-34; % J s
eo = 8.85418e-14; % F/cm
epsilon = 11*eo; %for Zn3P2
%
% Absorption properties
ke=2.1; % k at excitation
alpha = 4*pi*ke/lambda;
ke2=0.01; % k at emission
lambda2 = 820e-7; % emission wavelength (m)
alpha2 = 4*pi*ke2/lambda2;
alpha2 = 0; % self-absorption neglected
%
% Electronic properties
mup=20; % hole mobility
mun =1000; % electron mobility
Dp = k*T/q*mup;
Dn = k*T/q*mun;
%
% ambipolar diffusion constant
Da = 2/(1/Dp + 1/Dn);
%
tn = 27e-9; % electron lifetime
krad = 0; % assuming negligible radiative recombination
%
```

```
% doping properties
ni=1e14; % intrinsic carrier density @ RT
ppo=1e15; % background p-type doping
npo=ni^2/ppo; % background n-type doping
%
% values of SRV and Tau used for the TRPL model
Snloop = [1.4e3 8.2e3 2.3e4];
tauloop = [28 28 28]*1e-9;
%
%%% Time and Distance mesh bounds
Tsteps = 5000; % time meshing points
Xsteps = 50; % distance meshing points
tspan = linspace(0,50e-9,Tsteps);
xspan = [0,logspace(-9,log10(10000*1e-7),Xsteps)];
[xxx,yyy] = meshgrid(exp(-xspan*alpha2),tspan);
opt = odeset('InitialStep',1e-15,'MaxStep',1e-9);
%
%%% Execute PDE solver
Nsave = zeros(length(tspan),length(xspan),length(Snloop));
It = zeros(length(tspan),length(Snloop));
for w=1:length(Snloop)
Sn = Snloop(w)
tn = tauloop(w)
sol = pdepe(0,@pdefun,@icfun,@bcfun,xspan,tspan,opt);
% solver returns n(x,t) and p(x,t)
n = sol(:,:,1);
p = sol(:,:,2);
np = n.*p;
% integrated np(t) product
npint = trapz(xspan,np.*xxx,2);
```

```
%
% convolution of np(t) with Gaussian for detector width
npintcon= zeros(size(npint));
tstep = 50e-9/Tsteps;
intwidth = int16(dw/tstep)*4;
for index1=intwidth+2:1:length(tspan)-intwidth-2
for index2=index1-intwidth:1:index1+intwidth
npintcon(index1)=npintcon(index1)+npint(index2)*exp(double(-(index2-
-index1)^2/2/(dw/tstep)^2));
end
end
%
% renormalize to max intensity = 1
zzz=find(npintcon==max(npintcon));
npcorr = 1/npintcon(zzz);
npintconc = npintcon*npcorr;
It(:,w) = npintconc;
w
end
%
%
%
%%% Plotting
if PLOT>0
load PLdata3;
% check ambipolar diffusivity approximation
figure
surf(log10(xspan*1e7),log10(tspan*1e9),((npo+n) +
(ppo+n))./((npo+n)./Dp + (ppo+n)./Dn))
%
```

```
% check no(x,t=0) on log and lin scales
figure
plot(xspan*1e7,alpha*Np*exp(-alpha.*xspan),'k-')
%
% check n(x,t) on log scale
figure
surf(log10(xspan),log10(tspan),n)
xlabel('Distance x')
ylabel('Time t')
%
% check n(x,t) on lin scale
figure
plot(xspan,n)
xlabel('Distance x')
ylabel('intensity')
xlim([0,100e-7])
%
% check np(x,t) on lin scale
figure
plot(xspan,np)
xlabel('Distance x')
ylabel('intensity')
xlim([0,100e-7])
%
% check integrated np(t) on log scale
figure
semilogy(tspan*1e9,npint)
xlabel('time s')
ylabel('intensity')
%
```

```
% check n(x,t), npo, ppo
figure
subplot(2,2,[1,3]); surf(xspan,tspan,n)
xlabel('Distance x')
ylabel('Time t')
xlim([0,100]*1e-7)
%
subplot(2,2,2);
semilogy(tspan*1e9,npo+nt,'r.-'); hold on
semilogy(tspan*1e9,ppo+nt,'b.-')
%
subplot(2,2,4);
semilogy(tspan*1e9,npo+nt,'r.-'); hold on
semilogy(tspan*1e9,ppo+nt,'b.-')
%
% plots of TRPL data and model prediction, LIN & LOG scale
% and plots of difference between TRPL data and model prediction
%
% PLOT of TRPL data and model prediction, LIN scale
figure
subplot(3,2,[1,3])
plot(PLdata3(:,1),PLdata3(:,2),'.','color',[0.7 0.7 0.7]); hold on
plot(PLdata3(:,1),PLdata3(:,3),'g.')
plot(PLdata3(:,1),PLdata3(:,4),'b.')
plot(tspan*1e9,It,'k--','LineWidth',1.5)
ylim([0,1])
xlim([0,30])
%
% plot difference between TRPL data and model
subplot(3,2,[5])
```

```
plot(PLdata3(:,1),PLdata3(:,2) - It(:,1),'.','color',[0.7 0.7 0.7]);
hold on
plot(PLdata3(:,1),PLdata3(:,3) - It(:,2),'g.')
plot(PLdata3(:,1),PLdata3(:,4) - It(:,3),'b.')
ylim([-1,1])
xlim([0,30])
%
% PLOT of TRPL data and model prediction, LOG scale
subplot(3,2,[2,4])
semilogy(PLdata3(:,1),PLdata3(:,2),'.','color',[0.7 0.7 0.7]); hold on
plot(PLdata3(:,1),PLdata3(:,3),'g.')
plot(PLdata3(:,1),PLdata3(:,4),'b.')
plot(tspan*1e9,It,'k--','LineWidth',1.5)
ylim([1e-4,1])
xlim([0,50])
%
% plot difference between TRPL data and model
subplot(3,2,[6])
semilogy(PLdata3(:,1),abs(PLdata3(:,2) - It(:,1)),'.','color',[0.7 0.7
0.7]); hold on
plot(PLdata3(:,1),abs(PLdata3(:,3) - It(:,2)),'g.')
plot(PLdata3(:,1),abs(PLdata3(:,4) - It(:,3)),'b.')
ylim([1e-4,1])
xlim([0,50])
%
%
% output of model for plotting
xlswrite(jpboutput,PLdata3,1);
xlswrite(jpboutput,It,2);
xlswrite(jpboutput,tspan,3);
```

```
end
%
%%% Necessary functions for PDE solver
% define PDE
function [c,f,s] = pdefun(x,t,u,dudx)
G=alpha*Np*exp(-alpha*x);
c = [1/Dn; 1/Dp; 0];
f = [dudx(1) - (u(1)+npo)*mun*dudx(3);
dudx(2) + (u(2)+ppo)*mup*dudx(3);
dudx(3)];
s = [(G - u(1)/tn + mun*(-dudx(3))*dudx(1))/Dn;
(G - u(2)/tn + mup*(-dudx(3))*dudx(2))/Dp;
-q*(u(1)-u(2))/epsilon];
end
%
% define initial function, n(x,t=0)
function [no_x] = icfun(x)
no_x = [0;0;0];
end
%
% define boundary conditions, Da*dn/dx(x=0) = n*Sn and dn/dx = 0 at
large x
function [pl,ql,pr,qr] = bcfun(xl,ul,xr,ur,t)
pl = [-Sn*ul(1);-Sn*ul(2);ul - 1e10];
ql = [Dn;Dp;0];
pr = ur;
qr = [0;0;0];
end
end
```

Appendix C

Photoelectrochemistry Procedures

Photoelectrochemical techniques are an invaluable tool for evaluating the material properties of semiconductors [100, 114, 118]. A series of fast, outer sphere redox couples spanning more than two volts in reduction potential have been studied for preparing semiconductor/liquid junctions. A semiconductor working electrode is prepared with an ohmic contact and immersed into an solution such that only the bare semiconductor surface is contacted by the solution. For studying material properties of semiconductors, the solution is often based on a nonaqueous solvent such as acetonitrile, tetrahydrofuran, or methanol with a dissolved electrolyte to reduce series resistance losses. Both halves of a redox couple are added to the solution to set the Fermi energy, or work function, such that the solution will make a rectifying contact to the semiconductor of interest. A high surface area Pt mesh is immersed into the solution to act as the counter electrode to complete the circuit. If desired, a reference electrode can be used to enable three-electrode electrical measurements. A bare Pt wire serves as the simplest option and poises the reference potential at the solution potential as determined by the redox couple. A Luggin capillary can be used instead to minimize the effects of solution resistance. Such a capillary consists of a glass tube that is pulled to a fine capillary of inner diameter $\sim$50 μm, filled with the solution and a Pt wire, and immersed into the photoelectrochemical cell.

C.1 Photoelectrochemical Cell Components

For typical nonaqueous photoelectrochemical experiments, CH_3CN (anhydrous, 99.8%) was distilled under N_2(g) (ultra high purity) from CaH_2 ($\geq$97%), $LiCl_4$ (bat-

tery grade, 99.99%) was dried by fusion at 350 °C under $<1 \times 10^{-3}$ Torr and was stored in a glove box that had <0.2 ppm of O_2(g). Bis(cyclopentadienyl) cobalt(II) (cobaltocene, $CoCp_2^0$) and bis(pentamethylcyclopentadienyl) cobalt(II) (decamethylcobaltocene, $Me_{10}CoCp_2^0$) were purchased from Sigma Aldrich and were purified by sublimation. Bis(cyclopentadienyl) cobalt(III) hexafluorophosphate (cobaltocenium, $CoCp2^+ \cdot PF_6^-$), bis(pentamethylcyclopentadienyl) cobalt(III) hexafluorophosphate (decamethylcobaltocenium, $Me_{10}CoCp_2^+ \cdot PF_6^-$), and tetrabutyl ammonium hexafluorophosphate ($NBt_4^+ \cdot PF_6^-$) were purchased from Sigma Aldrich and recrystallized before use.

Current density versus potential (J–E) data were collected at 50 $mV \cdot s^{-1}$ using a Princeton Applied Research (PAR 273) potentiostat. White light from a Sylvania ELH-type halogen bulb was passed through a quartz diffuser to provide the equivalent of air mass 1.5 illumination calibrated using a Si photodiode electrode inside the cell. Various illumination intensities were obtained by use of a combination of quartz neutral density filters. Conventional three-electrode photoelectrochemical cells were assembled in an inert atmosphere glove box, and included a Pt gauze counter electrode and a Pt wire reference electrode poised at the solution potential (depicted in figure C.1). An additional Pt disk working electrode was used to measure the uncompensated ohmic resistance of the cell, typically ≈50 Ω. The stir bar was placed directly next to the Cu_2O photoelectrode and was rotated at maximum possible speed (≈3000 rpm) to minimize mass transport effects. Stirring was accomplished by an external bar magnet attached to an electric motor (NWSL 12270-9) that was controlled by a DC power supply. The electrochemical data were analyzed and reported as-collected, without correction for any solution resistance or concentration overpotential losses [120].

Aqueous photoelectrochemical experiments were performed in ≈20 mL of aqueous 0.5 M K_2SO_4–0.050 M methyl viologen dichloride (MV^{2+}, 98%) that was buffered at pH = 3.6 by potassium hydrogen phthalate [89]. The Nernstian potential of the solution was driven to –0.6 V versus SCE using the large carbon cloth electrode as a working electrode and the frit-separated Pt mesh as a counter electrode. During

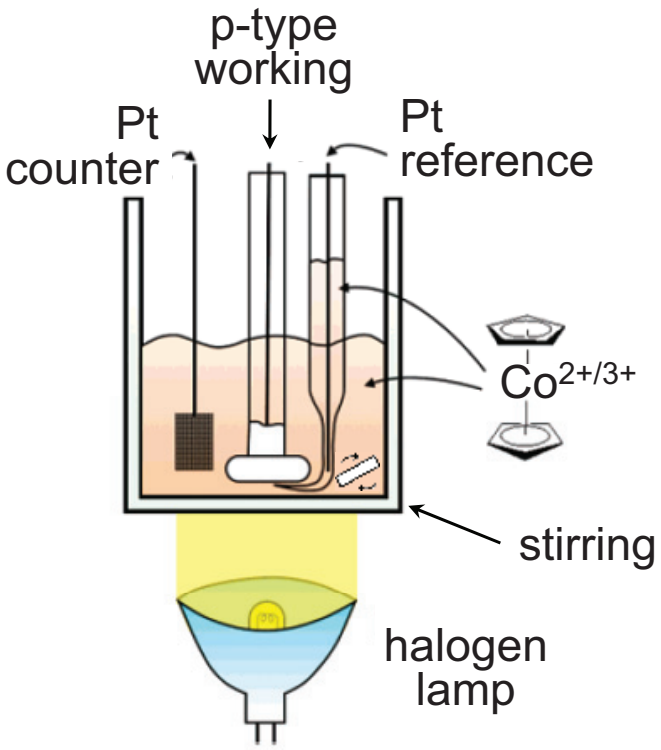

Figure C.1. Schematic of photoelectrochemical cell for conventional three-electrode measurements including a p-type semiconductor working electrode, a Pt gauze counter electrode, and a Pt wire reference electrode. The electrolyte used for investigating Zn_3P_2 substrates typically consisted of CH_3CN–1.0 M $NBt_4{\cdot}PF_6$–0.020 M $CoCp_2^+$–0.002 M $CoCp_2^0$ [90].

experiments with the Cu_2O working electrodes, the carbon cloth electrode served as the counter electrode, a Pt wire that was poised at the solution potential served as the reference electrode. The cell was purged with Ar(g) at all times, to minimize reaction between $MV^{+\cdot}$ and O_2(g).

Spectral response measurements were performed on a photoelectrochemical cell that contained CH_3CN–1.0 M $LiClO_4$–0.0020 M $Me_{10}CoCp_2^{+}$–0.0002 M $Me_{10}CoCp_2^{0}$. Relative to the solution used to collect *J–E* data, the solution used for spectral response measurements was diluted with CH_3CN to minimize solution absorption. A 50 W Xe arc lamp (Oriel) was chopped at 13 Hz and passed through a quarter-wave monochromator onto the working electrode in the photoelectrochemical cell. The light intensity was determined using using a calibrated Si photodiode that was placed at the same position as the working electrode. A Gamry Reference 600 potentiostat was used to measure the photocurrent at short circuit. Lock-in amplifiers (EGG Princeton Applied Research) collected signals from both the reference Si photodiode channel and from the potentiostat output channel. The signal from both lock-in amplifiers was fed into a computer that was controlled by a LabVIEW program.

C.2 Chemical Compatibility

Some adjustments to the above procedure were warranted due to issues with chemical compatibility. The first issue with Zn_3P_2 photoelectrochemical cells was the adsorption of Br_2 from the etching solution into the Hysol 1C epoxy used for electrode fabrication. As the Br_2 leeched from the electrode epoxy to the photoelectrochemical cell, the reduced form of the redox couple was rapidly oxidized, poisoning the electrochemical cell. To solve this problem a two-step etching system was required with alternating treatments of 0.05% Br_2 in methanol and 3 M NH_3 in methanol. The NH_3 was relatively inert in contact with the Zn_3P_2 substrate, but reacted with the residual Br_2 in the epoxy to form inert products of the form NH_xBr_{3-x}. The mixed etching system allowed measurements to be made without disrupting the redox balance of the electrochemical cell.

The second issue for working with Zn_3P_2 photoelectrochemical cells was the high reactivity of the Zn_3P_2 surface with the $LiClO_4$ electrolyte. The reaction did not appear to occur rapidly in the light or in the dark at open-circuit potentials, but with the onset of photocathodic current the Zn_3P_2 electrodes quickly became shorted. To investigate this behavior, a switch from epoxy-embedded electrodes to teflon-clamped electrodes was made. Figure C.2 shows a schematic of the two-electrode teflon photoelectrochemical cell used when recovering the substrate after the measurement is critical or if the substrate etchant is not compatible with epoxy. In the teflon electrochemical cells, Zn_3P_2 substrates that had been analyzed electrochemically were removed from the cell for surface composition analysis by XPS. Zn_3P_2 substrates that had been analyzed in the presence of $LiClO_4$ electrolyte displayed thick layers of $ZnCl_2$–evidence of a strong, irreversible electrochemical reaction that was degrading the performance of the cell. Substituting the $LiClO_4$ electrolyte for the more inert $NBt_4^+ \cdot PF_6^-$ enabled stable photoelectrochemical performance of Zn_3P_2 substrates.

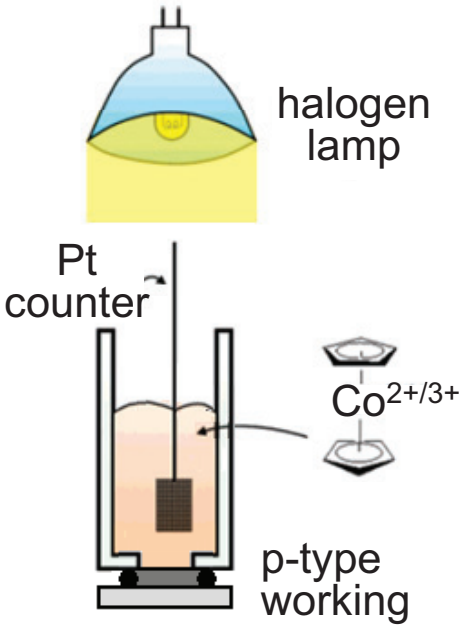

Figure C.2. Schematic of photoelectrochemical cell for two-electrode measurements including a p-type semiconductor working electrode and a Pt gauze counter electrode. The typical electrolyte used for investigating Zn_3P_2 substrates consisted of CH_3CN–1.0 M $NBt_4{\cdot}PF_6$–0.020 M $CoCp_2^+$–0.002 M $CoCp_2^0$. Two-electrode teflon cells are advantageous for semiconducting substrates that use etching chemistry incompatible with epoxy and for experiments that benefit from retrieving the substrate after operation in the photoelectrochemical cell [90].

Bibliography

[1] E. A. Fagen. Optical properties of Zn_3P_2. *Journal of Applied Physics*, 50(10): 6505–6515, 1979.

[2] M. Bhushan and A. Catalano. Polycrystalline Zn_3P_2 Schottky-barrier solar cells. *Applied Physics Letters*, 38(1):39–41, 1981.

[3] M. von Stackelberg and R. Paulus. Examinations on phosphides and arsenides of zinc and cadmium–the Zn_3P_2 lattice. *Zeitschrift Fur Physikalische Chemie-Abteilung B–Chemie Der Elementarprozesse Aufbau Der Materie*, 28(6):427–460, 1935.

[4] I. E. Zanin, K. B. Aleinikova, M. Y. Antipin, and M. M. Afanas'ev. Analysis of chemical bonding in Zn_3P_2 crystals from x-ray diffraction data. *Crystallography Reports*, 49(4):579–584, 2004.

[5] R.C. Schoonmaker, A.R. Venkitaraman, and P.K. Lee. Vaporization of zinc phosphide. *Journal of Physical Chemistry*, 71:2676, 1967.

[6] Z. Berak, J.; Pruchnik. Phase equilibria in zinc-cadmium-phosphorus system. 2. Zinc phosphorus system. *Roczniki Chemii*, 43(6):1141, 1969.

[7] I. J. Hegyi, E. W. Poor, E. E. Loebner, and J. G. White. Two crystal forms of ZnP_2, their preparation, structure, and optoelectronic properties. *Journal of Physics and Chemistry of Solids*, 24:333, 1963.

[8] D. H. M. W. Thewissen, A. H. A. Tinnemans, E. A. Vanderzouwenassink, A. Mackor, H. Vonkanel, R. Hauger, and P. Wachter. Photoelectrochemical

properties of α- and β-ZnP_2 electrodes and powders. *Journal of the Electrochemical Society*, 131:2048–2054, 1984.

[9] C. H. Henry. Limiting efficiencies of ideal single and multiple energy gap terrestrial solar cells. *Journal of Applied Physics*, 51(8):4494–4500, 1980.

[10] G. M. Kimball, A. M. Muller, N. S. Lewis, and H. A. Atwater. Photoluminescence-based measurements of the energy gap and diffusion length of Zn_3P_2. *Applied Physics Letters*, 95(11):3, 2009.

[11] P. J. Linchung. Energy band structures of Cd_3P_2 and Zn_3P_2. *Physica Status Solidi B–Basic Research*, 47(1):33–39, 1971.

[12] J. Andrzejewski and J. Misiewicz. Energy band structure of Zn_3P_2-type semiconductors: Analysis of the crystal structure simplifications and energy band calculations. *Physica Status Solidi B–Basic Research*, 227(2):515–540, 2001.

[13] F. C. Wang, A. L. Fahrenbruch, and R. H. Bube. Transport mechanisms for Mg/Zn_3P_2 junctions. *Journal of Applied Physics*, 53(12):8874–8879, 1982.

[14] M. Casey. Properties of zinc phosphide junctions and interfaces. *Journal of Applied Physics*, 61(8):2941–2946, 1987.

[15] M. Ginting and J. D. Leslie. Preparation and electrical properties of heterojunctions of ZnO on Zn_3P_2 and CdTe. *Canadian Journal of Physics*, 67(4): 448–455, 1989.

[16] M. Bhushan, J. A. Turner, and B. A. Parkinson. Photoelectrochemical investigation of Zn_3P_2. *Journal of the Electrochemical Society*, 133(3):536–539, 1986.

[17] J. Turner, B. A. Parkinson, and M. Bhushan. Photoelectrochemical characterization of p-Zn_3P_2. *Journal of the Electrochemical Society*, 130(8):C330–C330, 1983.

[18] S. R. Lunt, G. N. Ryba, P. G. Santangelo, and N. S. Lewis. Chemical studies of the passivation of GaAs surface recombination using sulfides and thiols. *Journal of Applied Physics*, 70(12):7449–7465, 1991.

[19] N. Prokopuk and N. S. Lewis. Energetics and kinetics of interfacial electron-transfer processes at chemically modified InP/liquid junctions. *Journal of Physical Chemistry B*, 108(14):4449–4456, 2004.

[20] F. C. Wang, R. H. Bube, R. S. Feigelson, and R. K. Route. Single-crystal growth of Zn_3P_2. *Journal of Crystal Growth*, 55(2):268–272, 1981.

[21] S. Fuke. Growth and characterization of zinc phosphide crystals. *Journal of Crystal Growth*, 87(4):567–570, 1988.

[22] D. E. C. Corbridge. *Phosphorus : an outline of its chemistry, biochemistry, and technology*. Elsevier, Amsterdam, 5th edition, 1990.

[23] J. Misiewicz, F. Krolicki, M. Lewicki, and J. F. Kasprzak. Growth of Zn_3P_2 crystals by gas-transport method. *Acta Physica Polonica A*, 69(6):1127–1130, 1986.

[24] A. Catalano. The growth of large Zn_3P_2 crystals by vapor transport. *Journal of Crystal Growth*, 49(4):681–686, 1980.

[25] C. G. Tuppen and B. H. Conen. Ultra-flat InP substrates produced using a chemomechanical polishing technique. *Journal of Crystal Growth*, 80:459–462, 1987.

[26] N. C. Wyeth and A. Catalano. Spectral response measurements of minority-carrier diffusion length in Zn_3P_2. *Journal of Applied Physics*, 50(3):1403–1407, 1979.

[27] A. Catalano and R. B. Hall. Defect dominated conductivity in Zn_3P_2. *Journal of Physics and Chemistry of Solids*, 41(6):635–640, 1980.

[28] J. Misiewicz. Inter-band transitions in Zn_3P_2. *Journal of Physics–Condensed Matter*, 2(8):2053–2072, 1990.

[29] A. Nayak, D. R. Rao, and H. D. Banerjee. Derivative spectra of polycrystalline Zn_3P_2 thin films. *Solid State Communications*, 78(2):149–151, 1991.

[30] J. M. Pawlikowski. Absorption edge of Zn_3P_2. *Physical Review B*, 26(8):4711–4713, 1982.

[31] V. Munoz. Optical properties of zinc phosphide. *Journal of Applied Physics*, 60(9):3282–3288, 1986.

[32] J. M. Pawlikowski, J. Misiewicz, and N. Mirowska. Direct and indirect optical transitions in Zn_3P_2. *Journal of Physics and Chemistry of Solids*, 40(12):1027–1033, 1979.

[33] L. Zdanowicz. Some optical properties of Zn_3P_2. *Acta Physica Polonica A*, 57 (2):159–165, 1980.

[34] J. Misiewicz and J. Andrzejewski. Pseudopotential calculation of the Zn_3P_2 energy band structure–antifluoride approximation. *Physica Status Solidi B–Basic Research*, 184(1):K7–K10, 1994.

[35] K. Sieranski. Semiempirical tight-binding band structure of II_3V_2 semiconductors–Cd_3P_2, Zn_3P_2, Cd_3As_2, and Zn_3As_2. *Physical review. B, Condensed Matter and Materials Physics*, 50(11):7331–7337, 1994.

[36] M. Bhushan. Mg-diffused zinc phosphide n/p junctions. *Journal of Applied Physics*, 53(1):514–519, 1982.

[37] F. Briones, F. C. Wang, and R. H. Bube. Pair transitions in Zn_3P_2. *Applied Physics Letters*, 39(10):805–807, 1981.

[38] S. Rumyantsev M. Levinshtein and M. Shur. *Handbook Series on Semiconductor Parameters*, volume 1. World Scientific, London, 1996.

[39] J. Haynes. New radiation resulting from recombination of holes and electrons in germanium. *Physical Review*, 98(6):1866–1868, 1955.

[40] S. M. Sze and K. K. Ng. *Physics of Semiconductor Devices*. John Wiley & Sons, Hoboken, New Jersey, 3rd edition, 2007.

[41] N. C. Wyeth and A. Catalano. Barrier heights of evaporated metal contacts on Zn_3P_2. *Journal of Applied Physics*, 51(4):2286–2288, 1980.

[42] T. Suda, M. Suzuki, and S. Kurita. Polycrystalline Zn_3P_2/indium-tin oxide solar cells. *Japanese Journal of Applied Physics Part 2–Letters*, 22(10):L656–L658, 1983.

[43] K. Kakishita, K. Aihara, and T. Suda. Zn_3P_2 photovoltaic film growth for Zn_3P_2/ZnSe solar cell. *Solar Energy Materials and Solar Cells*, 35(1-4):333–340, 1994.

[44] P. S. Nayar. Properties of zinc phosphide/zinc oxide heterojunctions. *Journal of Applied Physics*, 53(2):1069–1075, 1982.

[45] A. J. Nelson, L. L. Kazmerski, M. Engelhardt, and H. Hochst. Valence-band electronic structure of Zn_3P_2 as a function of annealing as studied by synchrotron radiation photoemission. *Journal of Applied Physics*, 67(3):1393–1396, 1990.

[46] U. Elrod, M. C. Luxsteiner, M. Obergfell, E. Bucher, and L. Schlapbach. Surface chemistry of Zn_3P_2 single-crystals studied by XPS. *Applied Physics B–Photophysics and Laser Chemistry*, 43(3):197–201, 1987.

[47] Y. Kato. Native oxides on etched Zn_3P_2 surfaces studied by x-ray photoelectron spectroscopy. *Applied Physics Letters*, 52(25):2133–2135, 1988.

[48] H. W. Nesbitt, G. M. Bancroft, R. Davidson, N. S. McIntyre, and A. R. Pratt. Minimum XPS core-level line widths of insulators, including silicate minerals. *American Mineralogist*, 89(5-6):878–882, 2004.

[49] M. P. Seah. *Practical Surface Analysis*. John Wiley & Sons, Chichester, 2nd edition, 1990.

[50] G. Hollinger, E. Bergignat, J. Joseph, and Y. Robach. On the nature of oxides on InP surfaces. *Journal of Vacuum Science & Technology A–Vacuum Surfaces and Films*, 3(6):2082–2088, 1985.

[51] R. R. Chang, R. Iyer, and D. L. Lile. Surface characterization of InP using photoluminescence. *Journal of Applied Physics*, 61(5):1995–2004, 1987.

[52] E. Yablonovitch, B. J. Skromme, R. Bhat, J. P. Harbison, and T. J. Gmitter. Band bending, Fermi-level pinning, and surface fixed charge on chemically prepared GaAs surfaces. *Applied Physics Letters*, 54(6):555–557, 1989.

[53] S. W. Feldberg, M. Evenor, D. Huppert, and S. Gottesfeld. Analysis of the decay of picosecond fluorescence in semiconductors–criteria for the presumption of electroneutrality during the decay of an exponential electron-hole profile. *Journal of Electroanalytical Chemistry*, 185(2):209–228, 1985.

[54] D. Huppert, M. Evenor, and Y. Shapira. Measurements of surface recombination velocity on CdS surfaces and Au interfaces. *Journal of Vacuum Science & Technology A–Vacuum Surfaces and Films*, 2(2):532–533, 1984.

[55] J. M. Moison, M. Vanrompay, and M. Bensoussan. Influence of the near band edge surface states on the luminescence efficiency of InP. *Applied Physics Letters*, 48(20):1362–1364, 1986.

[56] L. M. Terman. An investigation of surface states at a silicon silicon oxide interface employing metal oxide silicon diodes. *Solid-State Electronics*, 5(SEP-O):285–299, 1962.

[57] J. Misiewicz, J. M. Wrobel, and B. P. Clayman. Lattice modes of Zn_3P_2. *Solid State Communications*, 66(7):747–750, 1988.

[58] Y. Sun, Z. Liu, F. Machuca, P. Pianetta, and W. E. Spicer. Preparation of clean InP(100) surfaces studied by synchrotron radiation photoemission. *Journal of Vacuum Science & Technology A–Vacuum, surfaces, and films*, 21(1):219–225, 2003.

[59] Z. Liu, Y. Sun, F. Machuca, P. Pianetta, W. E. Spicer, and R. F. W. Pease. Preparation of clean GaAs(100) studied by synchrotron radiation photoemission. *Journal of Vacuum Science & Technology A–Vacuum, surfaces, and films*, 21(1):212–218, 2003.

[60] M. V. Lebedev, D. Ensling, R. Hunger, T. Mayer, and W. Jaegermann. Synchrotron photoemission spectroscopy study of ammonium hydroxide etching to prepare well-ordered GaAs(100) surfaces. *Applied Surface Science*, 229(1-4): 226–232, 2004.

[61] K. Strubbe and W. P. Gomes. Bromine-methanol as an etchant for semiconductors: A fundamental study on GaP. 1. Etching behavior of n-type and p-type GaP. *Journal of the Electrochemical Society*, 140(11):3294–3300, 1993.

[62] K. Strubbe and W. P. Gomes. Bromine-methanol as an etchant for semiconductors: A fundamental study on GaP. 2. Interaction between chemical and anodic etching of p-type GaP. *Journal of the Electrochemical Society*, 140(11): 3301–3305, 1993.

[63] Ihsan Barin. *Thermochemical Data of Pure Substances*. VCH, Wienheim, Germany, 1995.

[64] C. J. Spindt, R. S. Besser, R. Cao, K. Miyano, C. R. Helms, and W. E. Spicer. Photoemission study of the band bending and chemistry of sodium sulfide on GaAs(100). *Applied Physics Letters*, 54(12):1148–1150, 1989.

[65] B. J. Tufts, I. L. Abrahams, C. E. Caley, S. R. Lunt, G. M. Miskelly, M. J. Sailor, P. G. Santangelo, N. S. Lewis, A. L. Roe, and K. O. Hodgson. XPS

and EXAFS studies of the reactions of Co(III) ammine complexes with GaAs surfaces. *Journal of the American Chemical Society*, 112(13):5123–5136, 1990.

[66] C. A. Hogarth and M. A. Ghauri. Preparation of cadmium phosphate and cadmium zinc phosphate glasses and their electrical and optical properties. *Journal of Materials Science*, 14(7):1641–1646, 1979.

[67] K. S. Sree Harsha, K. J. Bachmann, P. H. Schmidt, E. G. Spencer, and F. A. Thiel. n-Indium tin oxide/p-indium phosphide solar cells. *Applied Physics Letters*, 30(12):645–646, 1977.

[68] K. Kamimura, T. Suzuki, and A. Kunioka. Metal-insulator-semiconductor Schottky-barrier solar cells fabricated on InP. *Applied Physics Letters*, 38(4): 259–261, 1981.

[69] Y. Robach, M. P. Besland, J. Joseph, G. Hollinger, P. Viktorovitch, P. Ferret, M. Pitaval, A. Falcou, and G. Post. Passivation of InP using $In(PO_3)_3$ condensed phosphates–from oxide growth properties to metal-insulator-semiconductor field-effect-transistor devices. *Journal of Applied Physics*, 71(6):2981–2992, 1992.

[70] A. Catalano and M. Bhushan. Evidence of *p-n* homojunction formation in Zn_3P_2. *Applied Physics Letters*, 37(6):567–569, 1980.

[71] L. L. Kazmerski and P. J. Ireland. Surface and interface properties of Zn_3P_2 solar cells. *Journal of Vacuum Science & Technology*, 18(2):368–371, 1981.

[72] H. J. Hovel. *Solar Cells*, volume 11 of *Semiconductors and Semimetals*. Academic Press, New York, 1975.

[73] V. B. Chernogorenko and K. A. Lynchak. Thermodynamic analysis of the combustion of metal powders and their oxides in phosphorus and of the combustion of the phosphides formed in oxygen. *Combustion Explosion and Shock Waves*, 34:298–304, 1998.

[74] J. C. Fuggle, L. M. Watson, D. J. Fabian, and S Affrossman. X-ray excited auger and photoelectron spectra of magnesium, some alloys of magnesium and its oxide. *Journal of Physics F–Metal Physics*, 5:375–383, 1975.

[75] L. C. Olsen, F. W. Addis, and W. Miller. Experimental and theoretical studies of Cu_2O solar-cells. *Solar Cells*, 7(3):247–279, 1982.

[76] B. P. Rai. Cu_2O solar cells–a review. *Solar Cells*, 25(3):265–272, 1988.

[77] J. A. Assimos and D. Trivich. Photovoltaic properties and barrier heights of single-crystal and polycrystalline Cu_2O/Cu contacts. *Journal of Applied Physics*, 44(4):1687–1693, 1973.

[78] A. A. Berezin and F. L. Weichman. Photovoltaic effect in cuprous oxide/copper junctions in relation to the optical absorption spectrum of cuprous oxide. *Solid State Communications*, 37(2):157–160, 1981.

[79] F. L. Weichman. Photoconductivity of cuprous oxide in relation to its other semiconducting properties. *Physical Review*, 117(4):998–1002, 1960.

[80] D. Trivich, E. Y. Wang, R. J. Komp, K. Weng, and A. Kakar. Cuprous oxide photovoltaic cells. *Journal of the Electrochemical Society*, 124(8):C318–C318, 1977.

[81] A. O. Musa, T. Akomolafe, and M. J. Carter. Production of cuprous oxide–a solar cell material–by thermal oxidation and a study of its physical and electrical properties. *Solar Energy Materials and Solar Cells*, 51(3-4):305–316, 1998.

[82] L. C. Olsen, R. C. Bohara, and M. W. Urie. Explanation for low efficiency Cu_2O Schottky-barrier solar cells. *Applied Physics Letters*, 34(1):47–49, 1979.

[83] L. Papadimitriou, N. A. Economou, and D. Trivich. Heterojunction solar cells on cuprous oxide. *Solar Cells*, 3(1):73–80, 1981.

[84] A. Mittiga, E. Salza, F. Sarto, M. Tucci, and R. Vasanthi. Heterojunction solar cell with 2% efficiency based on a Cu_2O substrate. *Applied Physics Letters*, 88 (16), 2006.

[85] K. Akimoto, S. Ishizuka, M. Yanagita, Y. Nawa, G. K. Paul, and T. Sakurai. Thin film deposition of Cu_2O and application for solar cells. *Solar Energy*, 80 (6):715–722, 2006.

[86] J. Herion, E. A. Niekisch, and G. Scharl. Investigation of metal oxide/cuprous oxide heterojunction solar cells. *Solar Energy Materials*, 4(1):101–112, 1980.

[87] Y. Hames and S. E. San. CdO/Cu_2O solar cells by chemical deposition. *Solar Energy*, 77(3):291–294, 2004.

[88] T. Minami, Y. Nishi, T. Miyata, and J. Nomoto. High efficiency oxide solar cells with ZnO/Cu_2O heterojunction fabricated on thermally oxidized Cu_2O sheets. *Applied Physics Express*, 4(6), 2011.

[89] S. W. Boettcher, J. M. Spurgeon, M. C. Putnam, E. L. Warren, D. B. Turner-Evans, M. D. Kelzenberg, J. R. Maiolo, H. A. Atwater, and N. S. Lewis. Energy-conversion properties of vapor-liquid-solid-grown silicon wire-array photocathodes. *Science*, 327(5962):185–187, 2010.

[90] J. R. Maiolo, H. A. Atwater, and N. S. Lewis. Macroporous silicon as a model for silicon wire array solar cells. *Journal of Physical Chemistry C*, 112(15): 6194–6201, 2008.

[91] J. R. Maiolo, B. M. Kayes, M. A. Filler, M. C. Putnam, M. D. Kelzenberg, H. A. Atwater, and N. S. Lewis. High aspect ratio silicon wire array photoelectrochemical cells. *Journal of the American Chemical Society*, 129(41):12346, 2007.

[92] M. J. N. Pourbaix. *Thermodynamics of Dilute Aqueous Solutions*. Arnold, London, 1949.

[93] G. Nagasubramanian, A. S. Gioda, and A. J. Bard. Semiconductor electrodes. 37. Photoelectrochemical behavior of p-type Cu_2O in acetonitrile solutions. *Journal of the Electrochemical Society*, 128(10):2158–2164, 1981.

[94] J. L. Sculfort, D. Guyomard, and M. Herlem. Photoelectrochemical characterization of the p-Cu_2O/non-aqueous electrolyte junction. *Electrochimica Acta*, 29(4):459–465, 1984.

[95] G. Vanamerongen, D. Guyomard, and M. Herlem. Photoelectrochemical behavior of the junction Cu_2O/liquid ammoniate of sodium iodide ($NaI_3 \cdot 3NH_3$). *Solar Energy Materials*, 4(4):435–441, 1981.

[96] Y. Tachibana, R. Muramoto, H. Matsumoto, and S. Kuwabata. Photoelectrochemistry of p-type Cu_2O semiconductor electrode in ionic liquid. *Research on Chemical Intermediates*, 32(5-6):575–583, 2006.

[97] J. A. Assimos and D. Trivich. Photoelectric threshold, work function, and surface barrier potential of single-crystal cuprous oxide. *Physica Status Solidi A–Applied Research*, 26(2):477–488, 1974.

[98] L. M. Wong, S. Y. Chiam, J. Q. Huang, S. J. Wang, J. S. Pan, and W. K. Chim. Growth of Cu_2O on Ga-doped ZnO and their interface energy alignment for thin film solar cells. *Journal of Applied Physics*, 108(3), 2010.

[99] M. Okeeffe and W. J. Moore. Thermodynamics of formation and migration of defects in cuprous oxide. *Journal of Chemical Physics*, 36(11):3009, 1962.

[100] M. X. Tan, P. E. Laibinis, S. T. Nguyen, J. M. Kesselman, C. E. Stanton, and N. S. Lewis. Principles and applications of semiconductor photoelectrochemistry. *Progress in Inorganic Chemistry*, 41:21–144, 1994.

[101] J. Spyridel, J. Stoimeno, and N. A. Economou. Oscillations in photoconductive response of Cu_2O. *Physica Status Solidi A–Applied Research*, 13(1):K87, 1972.

[102] J. Spyridel, J. Stoimeno, and N. A. Economou. Optical and photoconductive phenomena in cuprous oxide. *Physica Status Solidi*, 20(2):623, 1967.

[103] S. Poulston, P. M. Parlett, P. Stone, and M. Bowker. Surface oxidation and reduction of CuO and Cu_2O studied using XPS and XAES. *Surface and Interface Analysis*, 24(12):811–820, 1996.

[104] J. P. Tobin, W. Hirschwald, and J. Cunningham. XPS and XAES studies of transient enhancement of Cu^{I} at CuO surfaces during vacuum outgassing. *Applied Surface Science*, 16(3-4):441–452, 1983.

[105] T. H. Fleisch and G. J. Mains. Reduction of copper oxides by uv radiation and atomic hydrogen studied by XPS. *Applied Surface Science*, 10(1):51–62, 1982.

[106] G. Panzner, B. Egert, and H. P. Schmidt. The stability of CuO and Cu_2O surfaces during argon sputtering studied by XPS and AES. *Surface Science*, 151(2-3):400–408, 1985.

[107] T. Minami, H. Tanaka, T. Shimakawa, T. Miyata, and H. Sato. High efficiency oxide heterojunction solar cells using Cu_2O sheets. *Japanese Journal of Applied Physics Part 2–Letters & Express Letters*, 43(7A):L917–L919, 2004.

[108] W. M. Sears, E. Fortin, and J. B. Webb. Indium tin oxide/Cu_2O photovoltaic cells. *Thin Solid Films*, 103(3):303–309, 1983.

[109] R. P. Wijesundara, L. D. R. D. Perera, K. D. Jayasuriya, W. Siripala, K. T. L. De Silva, A. P. Samantilleke, and I. M. Dharmadasa. Sulphidation of electrodeposited cuprous oxide thin films for photovoltaic applications. *Solar Energy Materials and Solar Cells*, 61(3):277–286, 2000.

[110] C. M. McShane, W. P. Siripala, and K. S. Choi. Effect of junction morphology on the performance of polycrystalline Cu_2O homojunction solar cells. *Journal of Physical Chemistry Letters*, 1(18):2666–2670, 2010.

[111] K. H. Han and M. Tao. Electrochemically-deposited *p-n* homojunction cuprous oxide solar cells. *Solar Energy Materials and Solar Cells*, 93(1):153–157, 2009.

[112] T. Mahalingam, J. S. P. Chitra, J. P. Chu, H. Moon, H. J. Kwon, and Y. D. Kim. Photoelectrochemical solar cell studies on electroplated cuprous oxide thin films. *Journal of Materials Science–Materials in Electronics*, 17(7):519–523, 2006.

[113] J. L. Robbins, N. Edelstein, B. Spencer, and J. C. Smart. Syntheses and electronic structures of decamethylmetallocenes. *Journal of the American Chemical Society*, 104(7):1882–1893, 1982.

[114] N. S. Lewis. A quantitative investigation of the open-circuit photovoltage of the semiconductor liquid interface. *Journal of the Electrochemical Society*, 131 (11):2496–2503, 1984.

[115] J. W. Hodby, T. E. Jenkins, C. Schwab, H. Tamura, and D. Trivich. Cyclotron resonance of electrons and of holes in cuprous oxide, Cu_2O. *Journal of Physics C–Solid State Physics*, 9(8):1429–1439, 1976.

[116] A. Goltzene and C. Schwab. Impurity scattering effect on the cyclotron resonance of carriers in Cu_2O. *Physica Status Solidi B–Basic Research*, 92(2): 483–487, 1979.

[117] G. Dasbach, D. Frohlich, H. Stolz, R. Klieber, D. Suter, and M. Bayer. Anisotropic effective exciton mass in Cu_2O. *Fourth International Conference on Physics of Light-Matter Coupling in Nanostructures*, 2(2):886–889, 2005.

[118] J. F. Gibbons, G. W. Cogan, C. M. Gronet, and N. S. Lewis. A 14-percent efficient nonaqueous semiconductor liquid junction solar-cell. *Applied Physics Letters*, 45(10):1095–1097, 1984.

[119] M. Evenor, S. Gottesfeld, Z. Harzion, D. Huppert, and S. W. Feldberg. Time-resolved photoluminescence in the picosecond time domain from CdS crystals

immersed in electrolytes. *Journal of Physical Chemistry*, 88(25):6213–6218, 1984.

[120] A. J. Bard and L. R. Faulkner. *Electrochemical Methods, Fundamental and Applications*. Wiley, United States, 2nd edition, 2000.